

SPECTROSCOPY OF EXOTIC NUCLEI WITH THE S800 SPECTROGRAPH

By

Joseph Arthur Caggiano

A DISSERTATION

Submitted to
Michigan State University
in partial fulfillment of the requirements
for the degree of

DOCTOR OF PHILOSOPHY

Department of Physics and Astronomy

1999

ABSTRACT

SPECTROSCOPY OF EXOTIC NUCLEI WITH THE S800 SPECTROGRAPH

By

Joseph Arthur Caggiano

The high resolution, broad range S800 magnetic spectrograph was built at the National Superconducting Cyclotron Laboratory (NSCL) and commissioned in September 1996. The purpose for building the S800 was to allow the study of exotic nuclei. As part of this thesis, the magnetic fields of the spectrograph dipoles were measured and used to compute transfer maps to allow the high resolution of the spectrograph to be achieved and to confirm that the spectrograph met design criteria.

Binary multinucleon transfer reactions were used to spectroscopically study the exotic nuclei ^{10}Li , ^{23}Al , and ^{27}P . The $^9\text{Be}(^9\text{Be}, ^8\text{B})^{10}\text{Li}$ reaction populated a p-wave state at a neutron separation energy of $-500(60)$ keV in the ^{10}Li nucleus. Evidence for a lower lying state was insufficient to draw conclusions about the state.

The masses and first excited states of the astrophysically significant nuclei ^{23}Al and ^{27}P were measured. The $^{24}\text{Mg}(^7\text{Li}, ^8\text{He})^{23}\text{Al}$ reaction was used to measure the mass excess of the ^{23}Al ground state, $M.E.=-6773(28)$ keV, and its first excited state location, $E_x=550(20)$ keV, both in agreement with past measurements. The $^{28}\text{Si}(^7\text{Li}, ^8\text{He})^{27}\text{P}$ reaction was used to measure the mass excess of the ^{27}P ground state, $M.E.=-670(41)$ keV, and its first excited state location, $E_x=1.199(19)$ keV, which is the first experimental report

of this state. The significance of these measurements to the astrophysical rp process will be discussed.

To my family, both human and animal

Acknowledgements

First and foremost, I would like to thank my advisor, Brad Sherrill, for his support throughout my graduate career. His presence, stamina and abilities have been inspiring. Walt Benenson has also been an inspiration during my graduate career; he is a great teacher and was always there when I needed him. I would like to thank Martin Berz, Tim Beers, and Julius Kovacs for serving on my advising committee.

Al Zeller provided assistance innumerable times during the S800 construction phase.

I must thank the Operations and Support staff at the NSCL for providing the necessary technical assistance and beams that made this dissertation possible.

I would like to thank Renan Fontus, Phil Johnson, and Len Morris for their tremendous help with the mapper project.

Daniel Bazin has provided immeasurable assistance, from mapping to configuring detectors and data acquisition, and to providing transfer maps. Thanks, Daniel.

I would like to thank Jon Kruse, Chris Powell, and Barry Davids for their friendship. They have been true friends, always there to listen, discuss or help. I owe Jon a debt of gratitude for introducing me to the game of golf.

I want to thank Pat Lofy for his willingness to discuss and understanding of the game of baseball.

I would like to thank Mathias Steiner, Thomas Baumann and Renan Fontus for two very enjoyable DALMAC bicycle trips.

I thank my family for being supportive beyond belief. Thanks Mom, Dad, Scott, and Eric.

Finally, I would like to thank Njema Frazier, Ph.D. She always reminded me of the big picture and kept me sane when no one else could. She made the 6+ years I've spent in this God-forsaken state worthwhile.

Table of Contents

List of Figures	xi
List of Tables	xvii
1 Introduction	1
1.1 Mass measurement of exotic nuclei	1
1.2 Mass measurement using binary transfer reactions	4
1.3 Outline	5
2 The S800 Spectrograph	7
2.1 Magnetic spectrographs	7
2.2 Characteristics of the S800	8
2.2.1 Beamline and magnets	8
2.2.2 Detectors	13
2.3 Optics of the S800	13
2.3.1 Notation	13
2.3.2 Optical properties of the S800	15
2.3.2.1 Detector resolution considerations	17
2.3.2.2 Aberration Correction	17
3 Dipole Magnetic Field Measurements	19
3.1 Motivation for the measurements	19
3.2 Data Acquisition	21
3.2.1 General	21
3.2.2 Mapper hardware and electronics	23
3.2.2.1 Aluminum frame and cart	23
3.2.2.2 Induction coils	29
3.2.2.3 Analog-to-digital conversion	29

3.2.2.4	Electronic noise suppression	30
3.2.2.5	Position and time measurement	31
3.3	Post processing and data conversion	32
3.3.1	Raw data	32
3.3.2	Dead time correction	32
3.3.3	Accounting for missed field data	34
3.3.4	Voltage offset correction and sweep alignment	34
3.3.5	Field calibration	35
3.3.6	Position calibration	36
3.3.7	Smoothing	40
3.4	Results	42
3.4.1	Field curvature and gradients	51
3.4.2	Effective length	54
3.4.3	Edge angles	55
3.4.4	Alignment of both dipoles	56
3.5	Conclusions	56
4	Spectroscopy of ^{10}Li	59
4.1	Motivation	59
4.1.1	Halo nuclei	59
4.1.2	Lithium-11	60
4.1.3	Lithium-10	62
4.2	Experimental setup	69
4.2.1	Reaction and targets	69
4.2.2	S800	69
4.2.3	Detectors	70
4.2.4	Electronics	71
4.2.5	Calibrations	75
4.2.5.1	Tracking detector position calibrations	75
4.2.5.2	Elastic and inelastic scattering	79
4.2.5.3	Spectrograph bending radius calibration	79

4.2.5.4	Scattering angle calibration	80
4.2.5.5	Ray reconstruction	82
4.3	Results	83
4.3.1	^{10}Be and ^7He energy spectra	86
4.3.2	^{13}B energy spectrum	92
4.3.3	^{10}Li energy spectrum	95
4.3.3.1	Fitting procedure	98
4.4	Discussion	103
4.5	Conclusions	105
5	Spectroscopy of ^{27}P and ^{23}Al	107
5.1	Motivation	107
5.1.1	Explosive hydrogen burning and the rp process	107
5.1.2	Stellar Reaction Rates	109
5.1.3	Why study ^{27}P ?	113
5.1.4	Why study ^{23}Al ?	115
5.2	Experiment	116
5.3	Results	120
5.4	Discussion	129
5.4.1	The Isobaric Multiplet Mass Equation (IMME)	129
5.4.2	Astrophysical implications	132
5.5	Conclusions	135
6	Summary	137
A	Mapper Post-Processing Software	140
A.1	Introduction	140
A.2	How to use the software	140
A.3	Sample input file	146
A.4	Output files	147

B Inverse transfer maps	150
Bibliography	155

List of Figures

2.1	Schematic of the S800 spectrograph. The analysis line consists of those elements from the object position to the target chamber; the spectrograph itself is the portion downstream from the target chamber.	9
2.2	Schematic of optical coordinate system, before entering system of magnets M and after leaving it. The xz plane at $y=0$ is defined as the midplane.	10
3.1	The dipole mapper assembly, shown together with the magnet steel in both magnets. The cart with the coils rides up and down along the guiding track, which is mounted on an aluminum plate. Only one mapper assembly was used; the mapper was installed in D1, the magnet was mapped, then the mapper was removed and installed into D2.	24
3.2	Dipole mapper cart assembly, top (left) and side (right) views. The pinch rollers keep the cart on the guiding track, and the wheels keep the cart on the same plane as it rides along the aluminum plate.	25
3.3	Schematic of the mapper showing the coordinate system used. The thick black lines are the magnet steel, the thin lines are the mapper plate. The gray box represents the cart that moves up and down along the plate. The three cylindrical coordinates are shown originating from a typical coil position on the cart (z is out of the page).	26
3.4	Schematic of the mapper DAQ system. The PC supplies commands to the motors and power to the on board electronics and controls event timing. The optosensor on the cart reads holes in the position strip and sends a square waveform back to the PC for position and timing information.	27
3.5	Timing diagram for one pass through the magnet. The gate signal is generated when the cart passes a certain point and tells the PC to start or stop acquiring data. As the optosensor passes the teeth in the position strip, it generates a square wave. Field measurement is broken up into 3-tooth (0.090") samples. T_{hi} and T_{lo} are the times that the waveform is spent in the high or low state, respectively. $T(1)$ and $T(2)$ are the live times for the ADC's. $T_{start}(i)$ is the time it takes to start the ADC's following detection of the first tooth in the sample. All the times mentioned are measured by counting 1 μ s clock ticks using a stopwatch circuit.	28
3.6	Raw data from one pass through the D1 magnet at 1.6 Tesla. The top panel is the time it takes the cart to travel 0.762 mm at a radius of 2.7 m for each field sample. The bottom panel is the raw voltage output from the ADC. The cart oscillation causes the oscillations in the measured voltage, better seen in the right half of the figure.	33

3.7	Position of Hall probe and NMR probes for magnetic field measurements. The thick lines are the locations of the Hall probe measurements; the dots are the location of the NMR probe measurements. The origin of the coordinate system is at the center of the entrance to the D1 magnet.	37
3.8	Hall probe data for D2 at 1.6 Tesla. The line through the data is a 5th order polynomial fit. The fit residuals are all < 0.1 Gauss.	38
3.9	Left: Excitation functions for D1 and D2 determined from NMR measurements. Right: Field strength as a function of starting radius for D2 determined by Hall probe measurements. The fields range from 0.28 T (top) to 1.6 T (bottom). . . .	39
3.10	Field measurement of small permanent magnets placed on the D1 magnet steel. The magnets are 1cm x 1cm x 2cm long. The top left panel shows all the magnets. The lines through the centers of the circular contours are 5mm from the magnet steel edge.	40
3.11	Dipole magnetic field data for both spectrograph dipoles. The current through the coils was ~350 A for both, giving fields of 1.48 Tesla for both D1 and D2. . . .	44
3.12	A D2 field map at 0.28 Tesla, plotted above 99% of the field strength. The contours are separated by one Gauss, indicating a very flat central field.	45
3.13	Field measurements for D2 at 1.6 Tesla. All contours are separated by 5 Gauss. In sharp contrast to Figure 3.12, the field exhibits a bowing behavior characteristic of saturation effects.	46
3.14	D1 (left) and D2 (right) magnetic field strength along the reference trajectory for the field settings from Tables 3.1 and 3.2. The curvature in the flat field region grows with field strength. The negative field just outside the coil also grows with field strength.	48
3.15	Magnetic field profile and derivatives along the reference trajectory for a D2 map at B=0.28 Tesla. The field profile is very flat in the center.	49
3.16	Magnetic field profile and derivatives along the reference trajectory for a D2 map at B=1.6 Tesla. The field is much more curved in the center than are lower fields. The effect of the coil is much more prominent than in Figure 3.13; the outermost shoulders in the first derivative are a larger fraction of the peak. The outermost peaks in the second derivative also demonstrate this effect.	50
3.17	Azimuthal field curvature for some field settings used during the mapping campaign. Despite the high curvature at the largest field settings, the field gradients remain within design specifications (1 Gauss/cm).	52
3.18	Measured radial field gradients in D1 with (+) the trim coils off and (O) the trim	

	coils on at their optimized setting.	53
3.19	Average radial gradients measured for D1 and D2 during the mapping campaign. Despite the apparently erratic pattern, the general pattern is reproduced for both dipoles. The error bars are $\pm 15\%$. The design limit is 1 Gauss/cm.	53
3.20	Effective length for both dipoles from field data, calculated by dividing the integrated field along the reference trajectory by the appropriate NMR reading (from Tables 3.1 and 3.2).	54
3.21	Contour plot of the overlapping field region of two maps at the same current and field settings. The contours are separated by 20 Gauss, and the region contoured is that ≤ 0.0 Gauss. The overlap of the contours is on the few Gauss level, indicating correct position and field calibration for the two dipoles.	57
4.1	The first experimental observation of ^{10}Li [Wi75] using the $^9\text{Be}(^9\text{Be},^8\text{B})^{10}\text{Li}$ reaction at 121 MeV. The resolution and statistics are poor in the ^{10}Li energy spectrum (bottom panel).	64
4.2	The $^{11}\text{B}(\pi^-,p)^{10}\text{Li}$ reaction [Am90]. It is difficult to tell whether the peak is a single state or a composite.	65
4.3	Results from the Young, <i>et al.</i> experiment [Yo94]. A prominent peak is observed at $-S_n=540$ keV.	66
4.4	Two measurements by the Bohlen group [Bo97]. The measurements show evidence for states at $-S_n = 240$ and 530 keV.	67
4.5	Schematic of the CRDC operation. A particle track ionizes the gas as it passes through the detector. The electrons drift to the anode wire where they are collected. An induced image charge on the cathode pads provides horizontal position information, while drift time of the electrons to the anode wire provide vertical position information. (Note the cathode pad locations are really on the front and back of the detector; they are shown schematically on the bottom here for clarity.)	73
4.6	Schematic of S800 focal plane detector electronics. Only one CRDC is shown and only one cathode pad is shown from the overall electronics to simplify the diagram.	74
4.7	Data taken with the position mask placed in front of the S801 CRDC. The top panel is the raw data taken with a small cut in the dispersive angle, theta, and the bottom panel is a picture of the prominently illuminated holes.	76
4.8	Detector y-position (TAC) drifting over time during this experiment. The circles are the centers of the distribution and the (+) are the widths. Error bars are not	

	plotted and fluctuations are due to low statistics.	78
4.9	Spectrograph bending radius calibration using elastically scattered ^9Be for the ^{10}Li experiment.	80
4.10	Elastic scattering of ^9Be beam at 40 MeV/u from a carbon target consisting of carbon with H_2O contamination. The solid lines are known kinematics for scattering off carbon nuclei populating states, from right to left, g.s., 4.44, 7.65, and 9.64 MeV. The dashed lines are scattering from ^{16}O and populating g.s., 6.1, and 7.1 MeV. The dot-dashed line is elastic scattering off ^1H nuclei. Aligning the known kinematics with the spectrum provides a very accurate scattering angle calibration.	81
4.11	Measured energy loss vs. time-of-flight spectra. Contamination in the 8B gate arises mainly from scattered beam.	85
4.12	Spectrum of ^{11}C ejectiles from $^{12}\text{C}(^9\text{Be}, ^{11}\text{C})^{10}\text{Be}$ reaction populating the ground and excited states in ^{10}Be . The solid lines overlaid on the spectrum are the calculated kinematics for known states in ^{10}Be . The dashed lines are the ^{11}C 2.0 MeV excited state corresponding to the reactions (from right to left) $^{12}\text{C}(^9\text{Be}, ^{11}\text{C}(2.0))^{10}\text{Be}(\text{g.s.})$ and $^{12}\text{C}(^9\text{Be}, ^{11}\text{C}(2.0))^{10}\text{Be}(3.368)$	88
4.13	Top: Spectrum of ^{11}C ions in the S800 focal plane populating states in ^{10}Be . The top panel shows the entire focal plane extent. Bottom: Five Gaussians were fit to the lower portion of the spectrum to determine the location of the g.s. and 3.368 MeV states in ^{10}Be	89
4.14	Same as figure 4.12, but using the $^9\text{Be}(^9\text{Be}, ^{11}\text{C})$ reaction to make ^7He	90
4.15	Fits to the ^7He ground state using two different resolution functions. The top panel shows a purely Gaussian resolution function, whereas the bottom shows an improved fit (<0 MeV) by including some Lorentzian shape in the resolution function. The mixture doesn't affect the peak location (430 ± 30 keV) of the fit, but has a small affect on the extracted width (120 ± 30 versus 150 ± 30 keV).	91
4.16	Top: Energy spectrum of 8B ions in the focal plane populating states in the ^{13}B nucleus. Bottom: Multiple Gaussian fits used for energy calibration of the focal plane.	94
4.17	Resolution function used for the $(^9\text{Be}, ^8\text{B})$ reaction (solid line). All three peaks have the same FWHM.	95
4.18	Rigidity calibration for this experiment. The line through the data is a linear fit. The points surrounded by squares are calibration points from the $^{12}\text{C}(^9\text{Be}, ^{11}\text{C})^{10}\text{Be}$ reaction; all others are from the $^{12}\text{C}(^9\text{Be}, ^8\text{B})^{13}\text{B}$ reaction.	97

4.19	Energy spectrum of ${}^8\text{B}$ ions from both the reactions ${}^{12}\text{C}({}^9\text{Be}, {}^8\text{B}){}^{13}\text{B}$ (top) and ${}^9\text{Be}({}^9\text{Be}, {}^8\text{B}){}^{10}\text{Li}$ (bottom), shown for comparison.	99
4.20	The ${}^{10}\text{Li}$ energy spectrum gathered in this experiment. The three different fits are of similar quality, but the single p-wave fits the data best because it has the fewest degrees of freedom. The background values were held constant for all three fits.	102
4.21	Two different reactions measuring the ${}^{10}\text{Li}$ energy spectrum. The similarities between the two are striking.	105
5.1	The rp-process network for specific temperature and density conditions, reprinted from [Ch92].	109
5.2	Subset of the chart of the nuclides schematically showing the rp-process reactions affecting the abundance of ${}^{26}\text{Si}$. This is just a small subset of the total reaction network (see Figure 5.1).	114
5.3	Benenson's spectroscopic measurement of ${}^{27}\text{P}$ [Be77]. There appears to be a state at ~ 1.2 MeV, but wasn't reported.	115
5.4	Previous spectroscopic measurement of ${}^{23}\text{Al}$. The first excited state is not resolved from the ground state [Wi88].	116
5.5	Primary beam spot at the focal plane, used to check the dispersion matching of the spectrograph for the experiment. The line through the data points is a single Gaussian fit; the error bars are statistical. The beam was transmitted to the focal plane from the object position with the spectrograph in dispersion matched mode. The FWHM of the peak corresponds to an energy resolution of $E/\Delta E \sim 4000$	119
5.6	Particle identification spectrum for this experiment.	120
5.7	All kinematic spectra for this experiment. The fractional energy is relative to the central energy and defined as $(E-E_0)/E_0$. The resolution is better at lower angles because of the reduced kinematic broadening effects at lower scattering angles (see Chapter 4).	123
5.8	${}^8\text{He}$ energy spectra for the listed reactions at $E({}^7\text{Li})=50.1$ MeV/u and $\Theta_{\text{lab}}=0-12^\circ$	124
5.9	${}^8\text{He}$ energy calibration for this experiment. The line through the data is a linear fit. Errors on the points are statistical uncertainties (translated into energy) and mass errors of the calibration nuclei summed in quadrature. The mass errors are taken from the 1995 Mass Evaluation Update [Au95].	125

5.10	The energy spectrum of the $^{24}\text{Mg}(^7\text{Li}, ^8\text{He})^{23}\text{Al}$ reaction.	126
5.11	The energy spectrum of the $^{28}\text{Si}(^7\text{Li}, ^8\text{He})^{27}\text{P}$ reaction.	126
5.12	New level schemes for ^{23}Al and ^{27}P following this experiment. The thick lines are measurements reported here; the thin lines are previous measurements. The excited state locations are given relative to the ground state of the nucleus from their respective measurements. The proton separation energies are a weighted average of the present ground state mass measurements and those of Benenson <i>et al.</i> in the seventies [Be75, Be77].	128
5.13	Mass excesses for the $A=23, J^\pi=5/2^+, T=3/2$ isobaric quartet. The line through the data is a quadratic fit; the box lists the coefficients from the fit with errors in MeV.	130
5.14	Mass excesses of the $A=27, J^\pi=1/2^+, T=3/2$ isobaric quartet. The line through the data is a quadratic fit; the box shows the fit coefficients and their errors in MeV. The two solid squares are this measurement (lower) and Benenson's measurement.	131
5.15	Astrophysical reaction rates using data from past and present experiments. . .	134
5.16	Astrophysical reaction rates due to past and present experiments. Note that the calculations of Herndl <i>et al.</i> [He95] agree with the present experiment.	135

List of Tables

2.1	Features of the S800 spectrograph.....	11
2.2	Parameters of the D1 and D2 magnets.....	11
2.3	Parameters of the Q1/Q2 quadrupole doublet.....	12
3.1	Mapping parameters used during D1 production maps.....	43
3.2	Mapping parameters used during D2 production maps.....	43
3.3	Entrance and exit angles for the D1 magnet.....	55
3.4	Entrance and exit angles for the D2 magnet.....	56
4.1	Previous measurements of ^{10}Li states below $-S_n=1.0$ MeV	63
4.2	Reaction cross sections from the ^{10}Li experiment. The uncertainties on the cross sections are purely statistical. A 10-50% systematic error from the beam current measurement is not included.....	84
4.3	Fitted parameters for ^{10}Li energy spectrum.....	101
5.1	Experimental observations of states in ^{23}Al	127
5.2	Experimental observations of states in ^{27}P	127
5.3	IMME coefficients for the $A=23$ and $A=27$, $T=3/2$ isobaric multiplets.....	132
5.4	Resonance parameters the levels that dominate resonant proton capture in the $^{22}\text{Mg}(p,\gamma)^{23}\text{Al}$ reaction.....	133
5.5	Resonance parameters the levels that dominate resonant proton capture in the $^{26}\text{Si}(p,\gamma)^{27}\text{P}$ reaction.....	133
A.1	Smoothing parameters and their meanings.....	143
B.1	Inverse map coefficients for the ^{10}Li experiment.....	151
B.2	Inverse map coefficients for the rp-process nuclei experiment.....	153

Chapter 1

Introduction

1.1 Mass measurement of exotic nuclei

As the interest in nuclei farther from stability increases, new and better experimental techniques are being developed to study them. The mass of a nucleus and its energy levels are two of its most fundamental properties. Measurement of atomic masses and the lowest energy states provide invaluable nuclear structure information. As in any measurement, high precision is an important and challenging aspect of the measurement.

The importance of mass measurements can be illustrated through a few examples. The understanding of stellar processes, which are powered by nuclear reactions, requires knowledge of the network of nuclear reactions and their rates, and they in turn depend on each reaction Q-value and, hence, the nuclear masses. Nucleosynthesis and elemental abundance are largely governed by nuclear binding energies and are often very sensitive to small mass or excited state uncertainties. High precision mass and energy level measurements are therefore required to constrain the complex models used to understand many topics ranging from stellar evolution to nucleosynthesis and elemental abundances.

The nuclear shell model uses experimentally determined masses and energy levels

as two of its most important pieces of data, so precisely known masses and energy levels are extremely useful. For example, the relatively small masses of nuclei such as ^4He , ^{16}O and ^{40}Ca illustrate shell closure effects and suggest that a shell model description of the nucleus is appropriate.

There are many ways to measure a nuclear mass and low-lying energy states. Direct mass measurements, in which the nucleus of interest is detected following separation based on its mass-to-charge ratio, has been used in many cases to determine ground state masses. High precision is possible if other well-known masses are detected simultaneously. Often the separator is a magnetic system and the equation $\frac{B\rho}{v} = \gamma \frac{m}{q} = \frac{B}{\omega}$ relates the mass to the magnetic field, the ion's speed and its cyclotron frequency. In principle it is possible to measure all of these quantities absolutely and with high precision. Direct measurements are limited to nuclei that live long enough to be transmitted through the experimental apparatus, typically $T_{1/2} \geq 1 \mu\text{s}$. This is a distinct disadvantage when studying nuclei far from stability where half-lives can be 10^{-6} - 10^{-21} seconds.

There are many direct mass measurement techniques, some of which rely on measuring a resonant frequency for circulation in a field or a flight time. Atom traps are examples of mass measurement through frequency measurement. Atoms stored in an electromagnetic trap reside in a potential minimum characterized by the fields and the ion's mass to charge ratio. Measuring their characteristic circulation frequency provides a mass measurement. Penning trap mass measurements rely on this technique and have been used to measure masses at a precision of 10^{-7} [Mi97]. However, high resolution Penning trap mass measurements are limited to ions with half-lives tens of seconds or greater.

The ESR at GSI also uses frequency measurement to deduce mass [Mi97]. Frag-

mentation is used to produce secondary beams which are transported to a storage ring where they are cooled and circulate for a few to a few hundred turns. A small metal probe is used to detect the ions as they pass, and the time spectrum is Fourier transformed into the frequency domain. The frequency spectrum translates directly into charge to mass ratio. Circulating ions with known masses with the ions of unknown mass provides a good calibration. Typical mass precisions of $\delta m/m \sim 10^{-4}$ - 10^{-7} are possible depending on the number of turns and other factors. Because of the cooling time, this technique is limited to relatively long-lived isotopes.

Time of flight techniques have been extended to exotic nuclei through the ability to produce and separate isotopes simultaneously with isotopes of known mass. These techniques have been used at such facilities as TOFI at Los Alamos and SPEG at GANIL[Mi97]. The nuclei are produced in a nuclear reaction and continue forward into a beamline. The magnetic rigidity ($B\rho$) and flight time over a known distance (i.e., the velocity) are measured and the ratio provides a measure of the mass-to-charge ratio. Typical time measurement resolution of 200 ps and typical flight times of 600 ns translates into 3×10^{-4} mass resolution if the magnetic rigidity of the ion can be measured to $\sim 1 \times 10^{-4}$. Advantages to this technique are that other nuclei with known masses can be detected simultaneously with the unknown masses which provides a good calibration, and the half-lives of the isotopes only have to be of the order of microseconds or longer.

Nuclear mass and excited state measurements are also possible through Q-value measurements. The Q-value of a nuclear decay or reaction can be used to determine the mass of one of the participants provided the masses of the others are known. For example, in the case of alpha decay, the Q-value is $Q = M_P - M_D - M_\alpha$ where M_P , M_D , and M_α

are the masses of the parent and daughter atoms and the mass of the ^4He atom. If the mass of the daughter nucleus is known and the energy of the emitted alpha particle (Q-value) is measured, the parent mass can be inferred.

1.2 Mass measurement using binary transfer reactions

A method that has been in use for several decades now is the binary, single- or multinucleon transfer reaction. The method involves striking a target with a beam of nuclei and through nucleon transfer, populating states in the unknown nucleus. The Q-value of the reaction $A(X,Y)B$ is given by $Q=m(A)+m(X)-m(B)-m(Y)$, where $m(A)$ is the mass of atom A. Knowing the mass of any three and measuring the Q-value gives the mass of the fourth nucleus. The mass of either the residual (B) or the ejectile (Y) can be determined by measuring the momentum of the ejectile.

The advantage to this method is that nuclei with well known masses can be used as participants, thus reducing the measured error. Typical mass errors can be 1-50 keV leading to a mass precision of $\delta m/m \leq 1.0 \times 10^{-6}$. The method can be used to measure the masses of nuclei with lifetimes much less than a microsecond and is not limited to bound nuclei; unbound resonances can be measured with this technique because the mass of the residual nucleus can be measured by measuring the ejectile's energy (see Chapters 4 and 5). Examples of reactions that have been used successfully in the past for reaching proton rich nuclei are the (p,d), (p,t) [Mi97], (^7Li , ^8He) [Wi88], and (^3He , ^8Li) [Be77] reactions while the (t,p) [Da85], (t, ^3He) [St69], (^{13}C , ^{12}N) [Bo97], and (^7Li , ^8B) [Yo94] reactions have been used for reaching neutron rich nuclei.

In principle there is no limit to the number of transferred nucleons or the Q-value. However, the cross sections become prohibitively small much beyond 3-nucleon transfer

or Q-values much less than -40 MeV. For example, a recent ^{36}Ca mass measurement using the $^{40}\text{Ca}(^4\text{He}, ^8\text{He})^{36}\text{Ca}$ reaction (Q-value=-57.6 MeV) has a cross section of ~ 1 nb/sr [Ko99] and was only possible through the large solid angle and high energy resolution of the S800. Another disadvantage is that accessing nuclei farther from stability requires special targets of rare or radioactive isotopes which may be difficult or practically impossible to manufacture.

Attempting to measure the mass of a residual nucleus with a transfer reaction to a precision of $\leq 1 \times 10^{-6}$ crucially depends on precise measurement of the ejectile's momentum. The magnetic spectrograph is a particularly attractive option for doing mass measurements in the case of low cross section reactions because they provide high background suppression, large acceptance, and high energy resolution. Energy resolutions of 1-50 keV are possible leading to mass precision of $\sim 10^{-7}$. The S800 spectrograph is a new experimental device which meets all these criteria. Its combination of high resolution, large solid angle and momentum acceptance, and good background suppression makes the S800 an excellent device for transfer reaction mass measurements.

1.3 Outline

Magnetic spectrographs can be thought of as nuclear microscopes: they look in a very detailed way at the microscopic properties of a nucleus, such as masses, energy levels, and angular momentum. Chapter 2 describes the motivation and the key features of the new magnetic spectrograph, the S800, built at Michigan State University.

Chapter 3 describes a task necessary for obtaining the high resolution required in the spectrograph: magnetic field measurement. The spectrograph consists of large magnetic quadrupoles and dipoles, and the goal was to measure precisely and accurately the

magnetic field profiles of each element in the spectrograph. The general techniques, data acquisition and data analysis will be outlined. The spectrograph dipoles will be discussed in this thesis. Quadrupole mapping was described in Bo Zhang's dissertation [Zh97].

Chapter 4 is the first of two chapters on mass measurements made with the spectrograph to study nuclei far from stability. Chapter 4 is devoted to the unbound nucleus, ^{10}Li , which is important for applying three body models to the halo nucleus ^{11}Li . A detailed background is given on the status of ^{10}Li measurements. The desire to study this nucleus with a spectrograph is described, and then the measurement techniques and experimental methods necessary to perform a spectroscopic measurement of states in ^{10}Li will be outlined.

Chapter 5 describes spectroscopic measurements of two proton rich nuclei that play significant roles in the astrophysical rp process. Background information is presented explaining why the measurement is necessary, the experiment is described, and the results presented and discussed. Finally, chapter 6 summarizes the dissertation.

Chapter 2

The S800 Spectrograph

2.1 Magnetic spectrographs

Magnetic spectrographs have become an invaluable tool for precise measurements in nuclear physics. They are generally used as the equivalent of a nuclear microscope to study nuclear structure. For a thorough review of magnetic spectrographs, see [En79]. The primary advantages of spectrographs as compared to other types of particle detector systems are background suppression and very precise momentum determination. Background suppression is a virtue in modern heavy ion physics experiments because it facilitates low cross section measurements in the presence of background that would otherwise hide the interesting events. Spectrographs are good for coincidence experiments with charged particle, neutron, or gamma ray detectors placed at the target. These characteristics are particularly important as nuclear physicists strive to learn more about very proton- and neutron-rich nuclei.

A magnetic spectrograph is an optical system for charged particles. It has an object and a focal plane, and it contains elements which bend and focus ions like lenses and prisms do for light. Magnetic spectrographs can be used to measure the momentum of an

ion using the following principle. A particle with charge, q , and mass, m , traveling at speed, v , passing through a uniform magnetic field with strength, B , will travel in a circular path with radius ρ given by balancing the centripetal and magnetic forces, $mv^2/\rho = qvB$, and thus $B\rho = p/q$, with $p = mv$. Relativistically, the mass is γm , where m is the rest mass and γ is the Lorentz transformation factor. Thus, for a given magnetic field setting, particles with identical momentum to charge ratios are deflected the same amount by the magnet.

Spectrographs can also measure the angles of emission of the particles. First, the spectrograph can be set to cover a limited angular range, say $10 \pm 1^\circ$. However, it is possible to design the optics of the system the angles of each individual beam particle within the spectrograph acceptance is measured (see section 2.3.2). Measurement of angles in nuclear physics experiments can be used to determine angular distributions of reaction products, which may be used to deduce the spin and parity of the state they are populating.

2.2 Characteristics of the S800

2.2.1 Beamline and magnets

The S800 was designed to have high energy and momentum resolution ($E/\Delta E = 10,000$, $p/\Delta p = 20,000$), good angular resolution ($\Delta\Theta = 2$ mrad), and large momentum and solid angle acceptance ($\Omega = 20$ msr, $\Delta p = 6\%$).

Figure 2.1 shows a schematic figure of the S800. The S800 consists of an analysis beamline (from the object to the target chamber), and a large spectrograph. The analysis line is very similar to the A1200 fragment separator at MSU [Sh92], but with better resolution and larger solid angle acceptance. Table 2.1 summarizes the features of the S800 spectrograph.

The analysis line consists of four 22.5° dipoles, five quadrupole triplets, four sextupoles, and one quadrupole doublet. The location labeled “object” in Figure 2.1 is the object used in high resolution, primary beam experiments. The intermediate image has a focus in x and y and a dispersion of $1.5 \text{ cm}/\%$. There is also a focus in x and y at the target position, but the dispersion is very high, $\sim 12 \text{ cm}/\%$. When making or transferring radioactive beams in the analysis line, the production target is the object position.

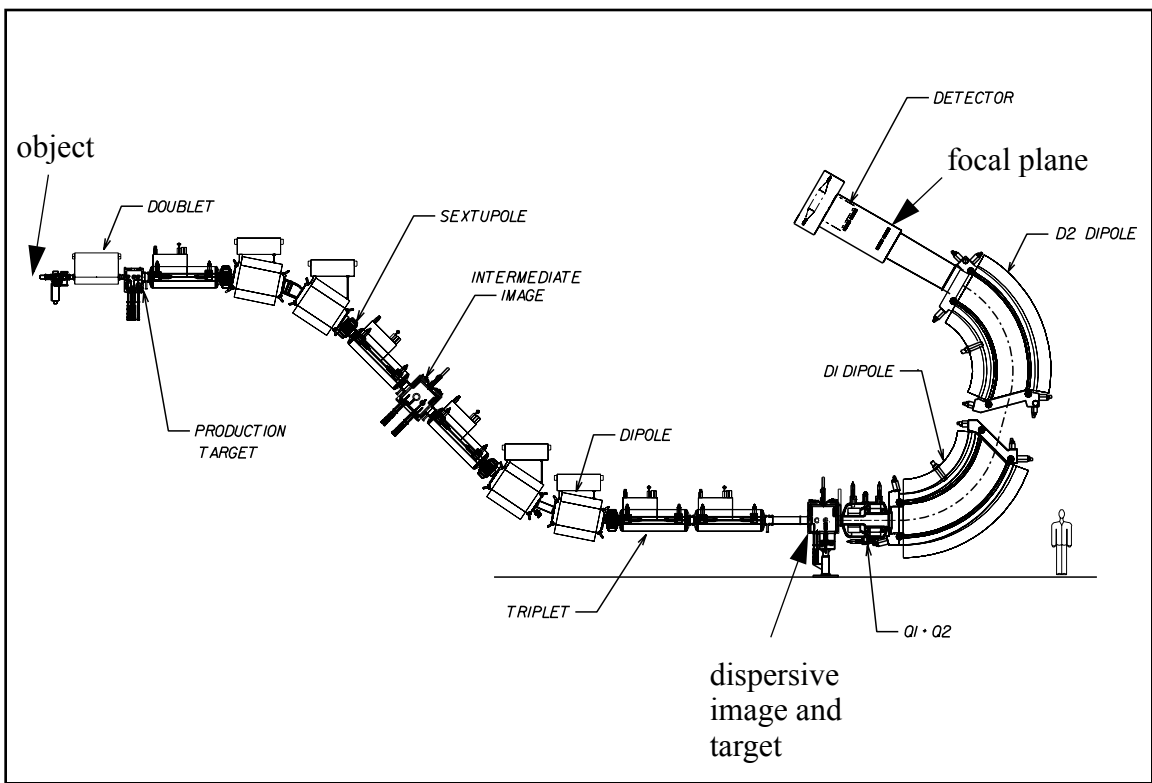


Figure 2.1: Schematic of the S800 spectrograph. The analysis line consists of those elements from the object position to the target chamber; the spectrograph itself is the portion downstream from the target chamber.

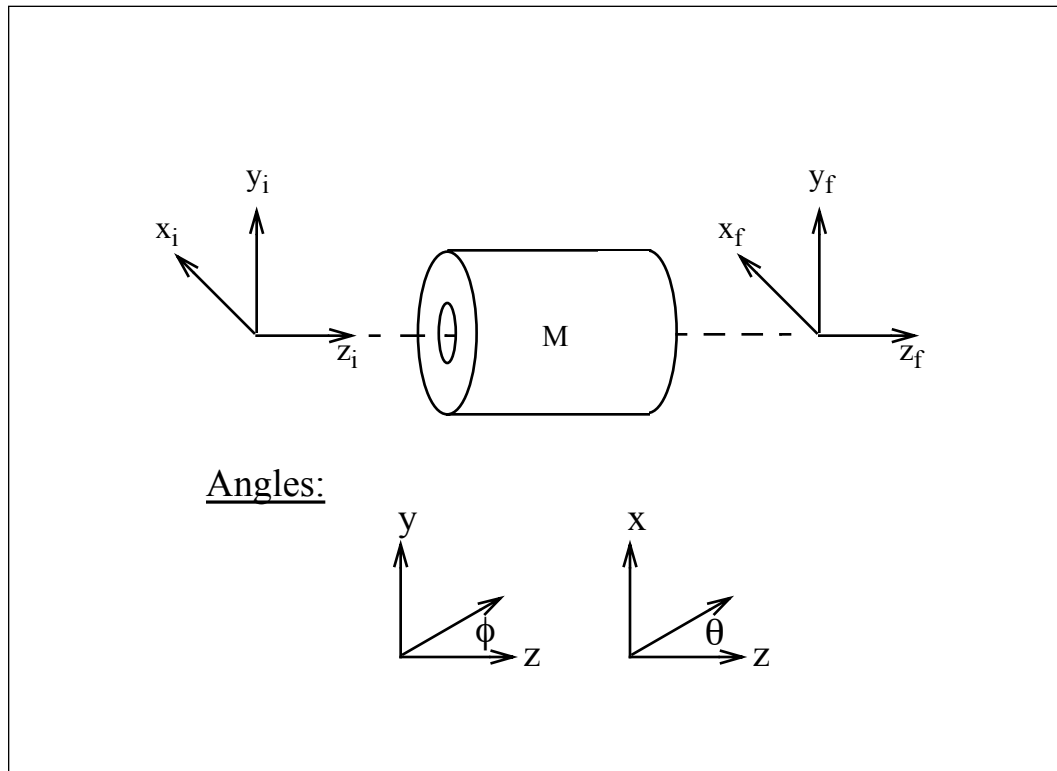


Figure 2.2: Schematic of optical coordinate system, before entering system of magnets M and after leaving it. The xz plane at $y=0$ is defined as the midplane.

Table 2.1: Features of the S800 spectrograph.

Energy, momentum resolution	$\Delta E/E=10^{-4}$, $\Delta p/p=5 \times 10^{-5}$
Energy, momentum range	11.6%, 5.8%
Solid angle	20 msr
Angular resolution	≤ 2 mrad
Horizontal dispersion ($x \delta$)	9.5 cm/%
Vertical dispersion ($y \phi$)	0.9 mm/mrad
Horizontal magnification ($x x$)	0.74
Focal plane size	55 cm (hor.) x 15 cm (ver.)
Detector separation	1 meter
Focal plane tilt	28.5°
Maximum rigidity	4.0 T-m
Maximum dipole field	1.6 Tesla
Dipole bend radius	2.8 m
Dipole bend angle	75°
Horizontal detector resolution	0.3 mm
Vertical detector resolution	0.3 mm

Table 2.2: Parameters of the D1 and D2 magnets.

Weight	70 Tons each
Dipole gap	15 cm
Maximum central field	1.6 Tesla
Dipole bend radius	2.8 m
Dipole bend angle	75°
Dipole entrance angle	D1=0°; D2 = 30°
Dipole exit angle	D1=-30°; D2=0°
Effective length (nominal)	3.7 m
Maximum current	450 A
Trim coil setting	43.75% of main current (1% of main coil A-Turns)
Maximum trim coil current	250 A

Table 2.3: Parameters of the Q1/Q2 quadrupole doublet.

Weight	5 Tons
Pole tip diameter	Q1=24 cm, Q2=42 cm
Maximum field gradient	Q1=19.7 T/m, Q2=7.5 T/m
Maximum current	Q1=85 A, Q2=100 A
Length of pole tips	Q1=30cm, Q2=30 cm
Effective length (nominal)	40 cm for both
Sextupole location	Q2
Maximum sextupole current	9 A

The beamline quadrupoles triplets are described in detail in Bo Zhang's dissertation [Zh97]. The triplets have a 6 inch bore for large acceptance. They are capable of maximum field gradients of 35 T/m and maximum currents of 100 Amps. The triplets weigh 5 tons each.

Table 2.2 summarizes the features of the superconducting spectrograph dipole magnets. The dipoles each weigh 70 Tons and have 6"x36" gaps. The dipoles have maximum central fields of 1.6 Tesla and NMR probes are placed in a flat field region to measure the absolute field setting of the dipoles during operation. The bend radii are 2.8 m, and bend angles are 75°. There are 30° edge angles on the dipole steel which defocus ions in the x direction while focussing them in the y direction, i.e., they act as quadrupoles. The dipole power supplies deliver up to 450 Amps to the coil and are stable to 1 part in 10⁵. Trim coils are present on the inner and outer radii of the dipoles to homogenize the field near the edges of the magnet. In the event of cryogenic failure, a coil protection switch takes the power supply out of the circuit and reroutes the current from the coils

through a dissipating resistor. At maximum current, 1.1 MJ of stored energy is dumped into this resistor with a decay constant of much less than a minute.

Table 2.3 summarizes the features of the spectrograph quadrupole doublet. Its design is described extensively in [Zh97]. It is a superconducting magnet with a cryogenic heat load of 2 Watts. There is no protection circuit on the quadrupoles as they can quench with no damage to the coils. The doublet focuses in the y direction first, then the x direction to maximize the acceptance of the spectrograph. Hall probes are fixed to the pole tips to measure the field gradient during operation.

There is a sextupole coil configuration around the bore tube of Q2. This is to correct the dominant $(x|\theta^2)$ spectrograph aberration in specific experiments such as studies of low-lying excited states via inelastic scattering. This will reduce the curvature of the lines to a known shape corresponding to the $(x|\phi^2)$ aberration, and a beam blocker can be placed in the focal plane to block the dominant elastic scattering.

2.2.2 Detectors

The standard S800 detector system consists of two position detectors, an ion chamber for energy loss measurement, and three scintillators for total energy measurement. This detector system and electronics will be described in detail in Chapter 4, and are presented in an annual report contribution by J. Yurkon and collaborators [Yu98]. The resolution requirements and their impact on spectrograph energy and angle resolution will be discussed later in this chapter.

2.3 Optics of the S800

2.3.1 Notation

The ions are guided through the beamline by the magnetic elements. The optical

coordinates of the ions are described in relation to a central, reference trajectory. This trajectory passes through the center of the magnets and has the reference momentum, defined by the $p_0=qB\rho_0$ for the dipole elements, where ρ_0 is the central bend radius for the dipoles, B is the dipole field, and q is the ionic charge.

Figure 2.2 illustrates the coordinate system used. The coordinate z is defined as the distance along the reference path at any point in the motion. The x coordinate is perpendicular to z at all points along the path, and defines the dispersive direction, i.e., the dipoles bend the ions in the xz -plane (labeled horizontal by convention). Two angles are defined in this coordinate system. Theta is the angle in the dispersive plane, and phi is the angle in the non-dispersive plane. The momentum coordinate is defined as $\delta = \frac{p}{p_0} - 1$. The coordinate l is the distance traveled along the central trajectory in relation to the reference particle, $l = \frac{l}{l_0} - 1$.

As the ions pass through the magnetic elements, their coordinates change due to the action of the magnetic fields on them. A simple transfer matrix can be used to relate the final coordinates to the initial coordinates. The transfer matrix contains information about how the ions travel through the fields in the system. If the fields are known, then the matrix can be determined by solving the Lorentz differential equation. To first order, the matrix equation is:

$$\begin{bmatrix} x_f \\ \theta_f \\ y_f \\ \phi_f \\ l_f \\ \delta_f \end{bmatrix} = \begin{bmatrix} (x|x) & (x|\theta) & (x|y) & (x|\phi) & (x|l) & (x|\delta) \\ (\theta|x) & (\theta|\theta) & (\theta|y) & (\theta|\phi) & (\theta|l) & (\theta|\delta) \\ (y|x) & (y|\theta) & (y|y) & (y|\phi) & (y|l) & (y|\delta) \\ (\phi|x) & (\phi|\theta) & (\phi|y) & (\phi|\phi) & (\phi|l) & (\phi|\delta) \\ (l|x) & (l|\theta) & (l|y) & (l|\phi) & (l|l) & (l|\delta) \\ (\delta|x) & (\delta|\theta) & (\delta|y) & (\delta|\phi) & (\delta|l) & (\delta|\delta) \end{bmatrix} \begin{bmatrix} x_i \\ \theta_i \\ y_i \\ \phi_i \\ l_i \\ \delta_i \end{bmatrix} \quad (2.1)$$

The transfer matrix equations take on a polynomial form when expressed as a Tay-

lor expansion about the central ray for only one final variable. The form is:

$$(x_f|x^i\theta^j y^k \phi^l l^m \delta^n) = \frac{1}{i!j!k!l!m!n!} \frac{\partial^{i+j+k+l+m+n} x_f}{\partial x^i \partial \theta^j \partial y^k \partial \phi^l \partial l^m \partial \delta^n} \quad (2. 2)$$

where x_f is the final coordinate and the derivatives are with respect to initial coordinates.

For example, the $(x|\theta^2)$ term has $i,k,l,m,n=0$ and $j=2$ and is given by $(x|\theta^2) = \frac{1}{2} \frac{\partial^2 x}{\partial \theta^2}$. The

equation for the transformation of the x coordinate:

$$x_f = (x|x)x_i + (x|\theta)\theta_i + (x|\delta)\delta_i + (x|\theta\phi)\theta_i\phi_i + (x|\theta\delta)\theta_i\delta_i + (x|\theta^2)\theta_i^2 + \dots \quad (2. 3)$$

where the i and f subscripts indicate the initial and final coordinates, respectively, and in principle the equation extends up to infinite order, with each successive order hopefully having a smaller affect. If a system has midplane symmetry, all terms with $(k+1)$ odd are zero. For example, terms like $(x|y)$, $(x|\phi)$, $(x|y^3)$, $(y|x)$, and $(\phi|\theta)$ are not allowed and are zero in Eq. 2.1.

2.3.2 Optical properties of the S800

The first order optics of the S800 are point to point in the x direction, i.e. $(x|\theta)=0$, and parallel-to-point in the y direction, i.e. $(y|y)=0$. In addition, the $(y|\phi)$ and $(x|\delta)$ (dispersion) terms dominate so the y position measurement is an accurate measurement of the scattering angle and the x position is an accurate measurement of the momentum. The dispersion has units of distance/(relative momentum in %). The dispersion of the spectrograph is 9.5 cm/%. Hence, two rays having the same initial positions and angles but differing in momentum by 1% will be separated by 9.5 cm at the focal plane.

The first order optics determine the momentum and angular resolution of the system as well as the measurement of certain other quantities. The momentum resolution of the system is defined as the reciprocal of the momentum deviation at which two peaks are

separated by their widths:

$$R = \frac{(x|\delta)}{(x|x)x_0 + \Delta x} \quad (2.4)$$

where $(x|x)$ is the magnification and x_0 is the object spot size. Aberrations present in the system add the Δx contribution to the denominator of Eq. 2.4. The goal of aberration correction is to make that contribution zero; this is the theoretical resolution limit.

One possible limitation to the resolution of the S800 is the intrinsic beam energy spread. Primary beams from the K1200 cyclotron at the NSCL have intrinsic energy spreads of 0.1% while secondary beams have 3% or more energy spread. The spectrograph is normally operated in dispersion-matched, energy-loss mode [No89] to compensate for this finite beam energy spread. The optical conditions for dispersion matching require that the final image have zero width, in the following manner. The spot size at the target position (dispersive image) between the beamline and the spectrograph is given, to first order, by $x_b = (x|x)_b x_0 + (x|\delta)_b \delta$ where x_0 is the object beam spot size and δ is the intrinsic dispersion in the beam, assuming a first order focus where $(x|\theta) = 0$. The spot size at the focal plane of the spectrograph is then given by $x_s = (x|x)_s x_b + (x|\delta)_s \delta$. The b and s subscripts denote the beamline and spectrograph, respectively. The term $(x|x)$ is the magnification M and $(x|\delta)$ is the dispersion D, and δ is the intrinsic beam momentum spread. The condition that the final spot size is negligibly small, i.e. $x_s = 0$ implies the condition $M_s x_b = -D_s \delta$. The initial spot size is assumed to be negligibly small so that $x_0 = 0$ and $x_b = D_b \delta$. Thus, the dispersion matching condition becomes:

$$D_b = \frac{-D_s}{M_s} \quad (2.5)$$

An excellent diagnostic for this condition in the S800 is a plot of the beam's time-of-flight

versus the x position at the focal plane (momentum). The TOF will vary according to the intrinsic momentum spread in the beam. The system is dispersion matched if the x position has no dependence on the TOF.

2.3.2.1 Detector resolution considerations

The resolution requirements of the spectrograph were considered in the detector design. In order to achieve the momentum resolution requirements given in Table 2.1, the horizontal resolution of the detectors should be better than $0.005\% * 95\text{mm}/\% = 0.475\text{mm}$. The measured angles are given by $\theta = \text{atan}\left(\frac{x_1 - x_2}{D}\right)$, where x_1 and x_2 are the two position measurements and D is the detector separation. The specified detector position resolutions listed in Table 2.1 correspond to a momentum precision of 0.003% and an angle error of 0.3 mrad.

Aberration correction requirements must be considered. Any angle error is magnified by a high order aberration in the system. For example, consider the dominant aberration $(x|\theta^2) = 0.006 \text{ mm/mrad}^2$. Given the 0.4 mrad angle measurement error as specified by the detector resolution, this translates into a worst case (i.e. if all events came with $\theta = 60\text{mrad}$) 0.4 mm error from the aberration, which is considered marginal. A more reasonable estimate would be if all events were evenly spread over the focal plane, giving an acceptable precision of 0.15 mm. Similar arguments can be made for the detector resolution considering the angular resolution requirements. A detailed study of these effects was made prior to construction of the S800 and is given in [No89].

2.3.2.2 Aberration Correction

In a magnetic spectrograph with large solid angle acceptance such as the S800, higher order aberrations significantly affect image quality, in both momentum and angle.

The dominant aberrations are the angular aberrations because they blur the image in the focal plane. These are the $(x|\theta^n\phi^m)$ terms where $n+m\geq 2$. The largest optical aberrations affecting the energy resolution are the $(x|\theta^2)$, $(x|\phi^2)$, and the $(x|\theta^3)$ terms. Chromatic aberrations such as $(x|\theta\delta)$ and $(x|\delta^2)$ are also substantial. Angular resolution is degraded by the dominant angular aberration $(y|y\phi)$.

Both hardware and software methods were evaluated for the correction of aberrations in the S800 [No89]. Because of the large solid angle in the S800, hardware corrections involve building large multipole magnets which can be costly. In addition, the multipoles would not be manufactured perfectly, and other aberrations could be introduced, and the need for software corrections still might be necessary. A detailed study determined that software correction for the S800 would be sufficient to achieve the desired angular and energy resolution [Be93]. Software correction is much more cost effective than building multipoles but comes at a price; the fields of the magnets need to be known accurately and with great precision. As specified in the article, aberrations must be accurately calculated up to 7th order to reach the design energy resolution which places certain constraints on the field knowledge. Chapter 3 will describe why and how field measurements were made.

Chapter 3

Dipole Magnetic Field Measurements

3.1 Motivation for the measurements

The S800 spectrograph makes use of magnetic elements to direct the ions that pass through it. If the magnetic fields of all the magnetic elements at all points in space are known, then an ion traveling through the fields can be tracked analytically, as they obey the Lorentz force law $d\mathbf{p}/dt=q(\mathbf{E} + \mathbf{v}\times\mathbf{B})$. Integrating the equations of motion provides the final momenta and positions for a given set of initial conditions. This relationship can be expressed as a matrix transformation of the initial coordinates to the final coordinates. Each element in the beamline has its own transfer matrix that describes how an ion's motion changes as it travels through the element. For a sequence of consecutive elements, the total transformation is just the product of transfer matrices.

Knowledge of these transfer matrices allows measurement of final coordinates to be translated into more meaningful nuclear physics quantities such as momentum, energy, and scattering angle. Specifically, in the S800, nuclear reactions occur in the target chamber and the emerging ions from the reaction are detected in the focal plane. Their positions and angles are measured in the two transverse directions. If the transfer matrix is known,

then it can be inverted to arrive at initial coordinates, such as the energy the ion had when it left the target and angle through which it was scattered. This process of reconstructing quantities in the target from the measured final coordinates in the focal plane is referred to as ray-reconstruction.

The spectrograph measures four quantities in the focal plane, and these are related to four different quantities in the target chamber by a matrix equation:

$$\begin{bmatrix} x_f \\ \theta_f \\ y_f \\ \phi_f \end{bmatrix} = S \begin{bmatrix} \theta_i \\ y_i \\ \phi_i \\ \delta_i \end{bmatrix} \quad (3.1)$$

where the subscripts f and i denote the measurements in the focal plane and the target chamber, respectively. The coordinates (x, θ , y, ϕ) are the two transverse positions, angles in the dispersive and non-dispersive directions, respectively. The coordinates (θ , y, ϕ , δ) describe the initial coordinates in the target chamber. The target spot size x_0 is assumed to be negligible, or equivalently that the incoherent width of the dispersion matched beam is negligible. Theta, phi and y carry the same meaning as in the focal plane; δ is the fractional kinetic energy difference from the central ray, $\delta=(E-E_0)/E_0$. The knowledge of the quantities in the target chamber now requires that this matrix equation be inverted. The inversion procedure is complicated and described in detail in [Be93]. The result is a matrix, R, which is not true inverse of S, but can be used to deduce energy and angles in the target chamber:

$$\begin{bmatrix} \theta_i \\ y_i \\ \phi_i \\ \delta_i \end{bmatrix} = \mathbf{R} \begin{bmatrix} x_f \\ \theta_f \\ y_f \\ \phi_f \end{bmatrix} \quad (3.2)$$

This inversion process includes the first order optics and all the optical aberrations as well.

Knowledge of this transfer matrix requires precise and accurate knowledge of the magnetic field data in the elements. The field data was intended to be used in the MF element in COSY [Be95]. If the system has midplane symmetry as the S800 does, then only specification of the midplane fields is necessary for complete description of the fields everywhere in the space of the magnet gap. COSY requires fields in a Cartesian coordinate system. This is easily understood: Maxwell's equations are far simpler in cartesian coordinates than in any other coordinate system. Thus, taking data in any other coordinate system requires interpolation onto a cartesian grid.

The precision and accuracy goal of the mapping process was 1 Gauss at all points along the beam path. However, it was shown that using the Gaussian image charge method of describing the data in COSY, 10 Gauss of random noise is allowable [De92]. There are tighter constraints on systematic errors as COSY may interpret them as field structures, and depend on the exact form of the error, but they are certainly ≤ 10 Gauss.

This chapter describes the techniques used for mapping.

3.2 Data Acquisition

3.2.1 General

The goal of the mapping project was to measure the fields in the dipole gaps to 1 Gauss accuracy, i.e., measure the fields as a function of position, $B(x,y,z)$. The field mea-

surement technique was to pass a coil of wire through the magnetic field and measure the induced voltage, $\epsilon = -d\Phi/dt$, where Φ is the magnetic flux through the coil. The field is determined along the path by time integral of the voltage. Field calibration measurements are made with NMR and Hall probes. The relative position measurement is done by reading teeth on a fixed strip along the coils' path and will be described in section 3.3.5. Absolute position calibration (relative to the magnet steel) is achieved by mapping small, strong, permanent magnets placed on the steel edges and is described in section 3.3.6.

The mapping coordinate system was chosen to be cylindrical, which is the natural coordinate system of the dipole magnets. The radial coordinate was perpendicular to the central beam's path, the angular coordinate parallel to the beams path, and the z coordinate perpendicular to both of those and parallel with the magnetic field lines in the center of the dipole.

The data acquisition system consisted of a 386-based personal computer, 5 ADC's (one for each induction coil), a scaler board (to count teeth and measure time), and a motor control board to control the stepper motors that moved the cart back and forth in the dipoles.

The general data acquisition algorithm was controlled by the PC. The coils make two passes through the field at a fixed radius. Once a lap is completed the coils are moved a fixed radial distance and another lap is started. It is through this rasterization procedure that the entire dipole gap is mapped.

The field measurements were taken at roughly one million individual points on a polar grid of 2.3 mm radial pitch by 0.05° angular pitch at 5 different vertical positions. Each sample contains position and time information for the coil package, and the 5 indi-

vidual coil voltages. A PC controlled the motion of the coils through the field and took data during the mapping cycle. Once a map was started, the system could be left to take data on its own until it had completed measurements over the whole gap of the dipole.

3.2.2 Mapper hardware and electronics

3.2.2.1 Aluminum frame and cart

The mapper was designed to fit in the gap of the two dipoles (see Figure 3.1). The frame is 0.5" thick aluminum plate, 27" across, with a central radius of 2.7 m, to match the central radius of the dipoles, and an angular extent of 110 degrees. The plate was firmly held in place against one side of the dipole gap with a combination of non-magnetic stainless steel brackets and suction. (A vacuum was applied to a large area between the plate and the dipole steel, creating approximately 6 tons of force on the plate to ensure it was flat against the magnet face.)

The coils ride on a G-10 cart, which is designed to ride on an aluminum guide that is mounted on the large aluminum frame that fits in the dipole gap. The cart was a 12"x25" rectangular piece of G-10, with aluminum hardware attached. The cart had four plastic pinch rollers, two on each side of the aluminum guide, to enable the cart to roll back and forth on an arc of fixed radius. The cart was held fixed in the y direction by eight wheels, one on each corner of the rectangular cart, top and bottom. The top four wheels were fixed in height and designed to press firmly against one surface at all times.

Only one mapper assembly was manufactured, so the dipoles were mapped sequentially. The mapper was first installed in D1, and the fields were measured. The mapper was then removed from D1 and installed in D2.

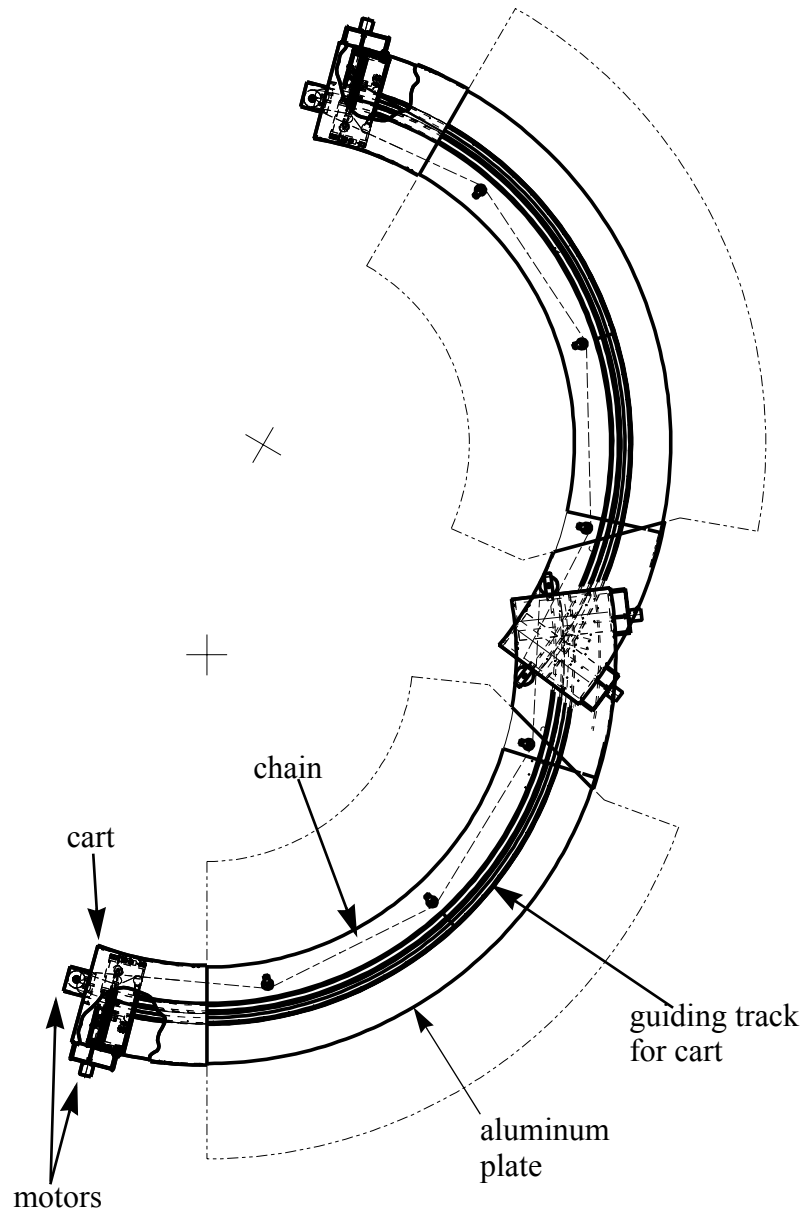


Figure 3.1: The dipole mapper assembly, shown together with the magnet steel in both magnets. The cart with the coils rides up and down along the guiding track, which is mounted on an aluminum plate. Only one mapper assembly was used; the mapper was installed in D1, the magnet was mapped, then the mapper was removed and installed into D2.

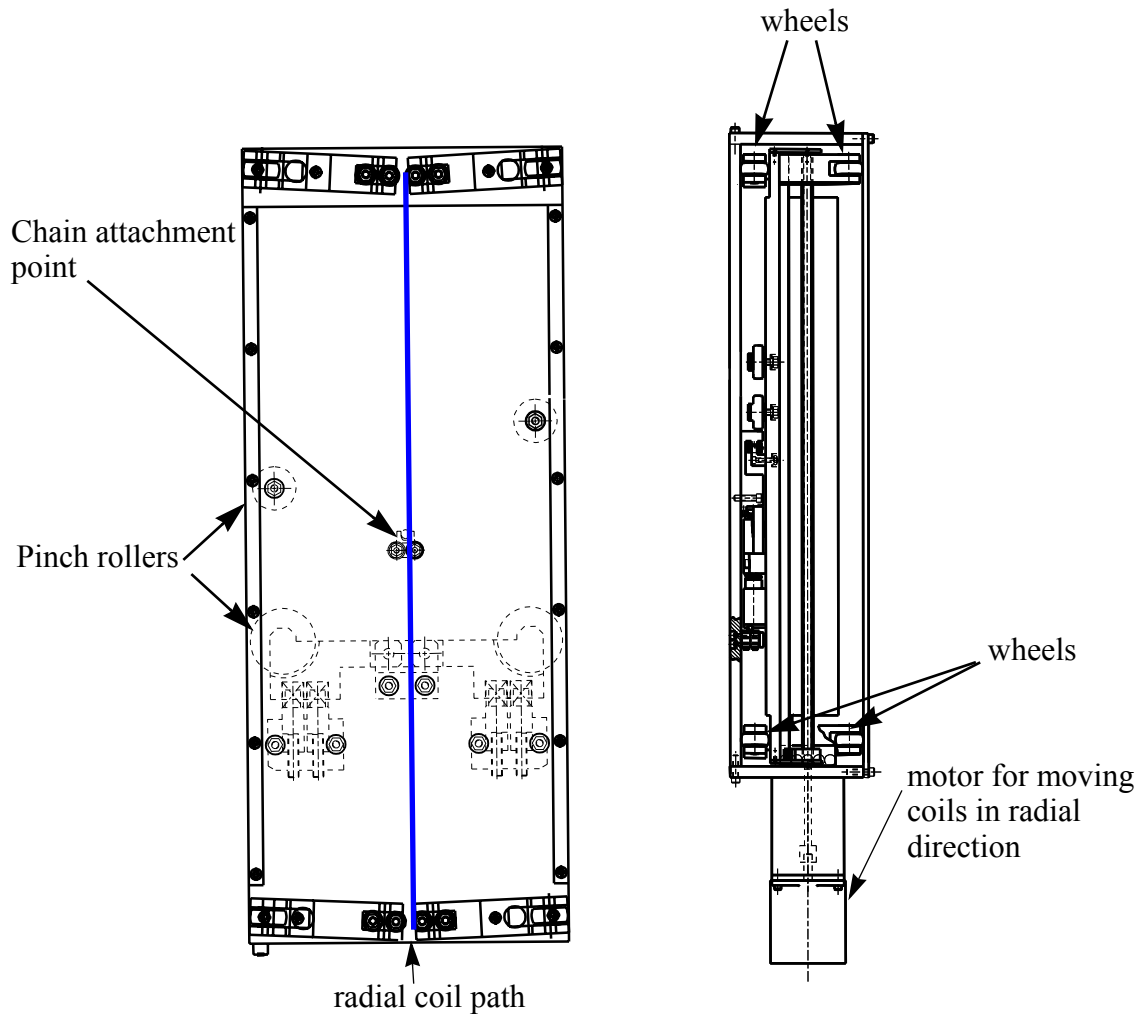


Figure 3.2: Dipole mapper cart assembly, top (left) and side (right) views. The pinch rollers keep the cart on the guiding track, and the wheels keep the cart on the same plane as it rides along the aluminum plate.

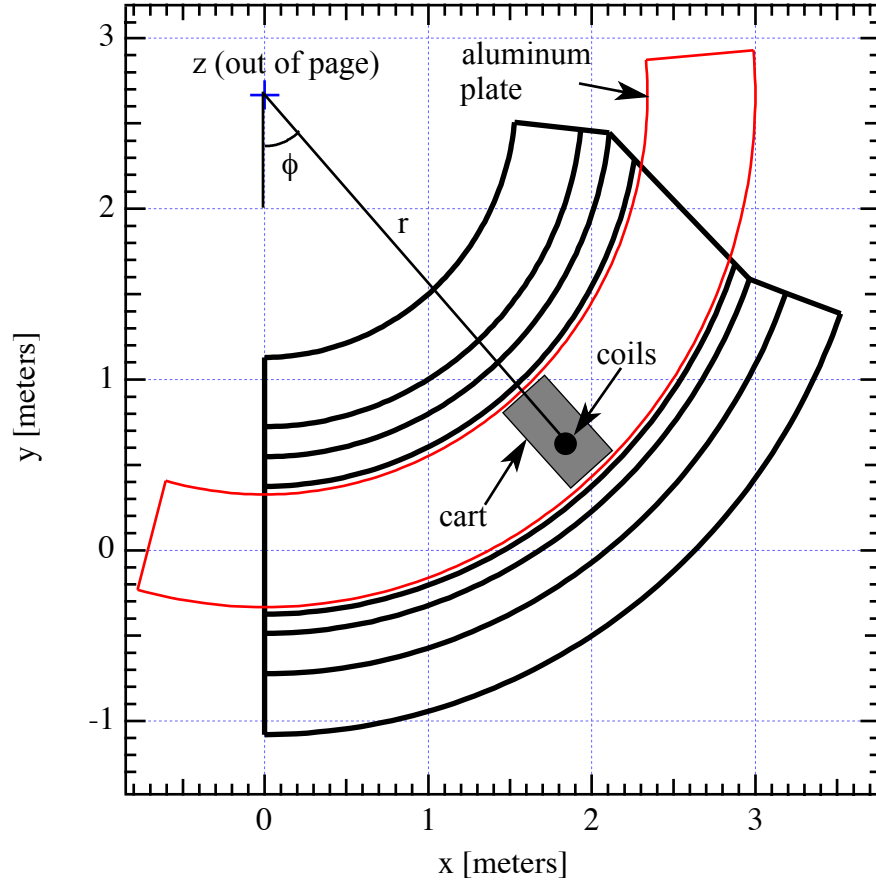


Figure 3.3: Schematic of the mapper showing the coordinate system used. The thick black lines are the magnet steel, the thin lines are the mapper plate. The gray box represents the cart that moves up and down along the plate. The three cylindrical coordinates are shown originating from a typical coil position on the cart (z is out of the page).

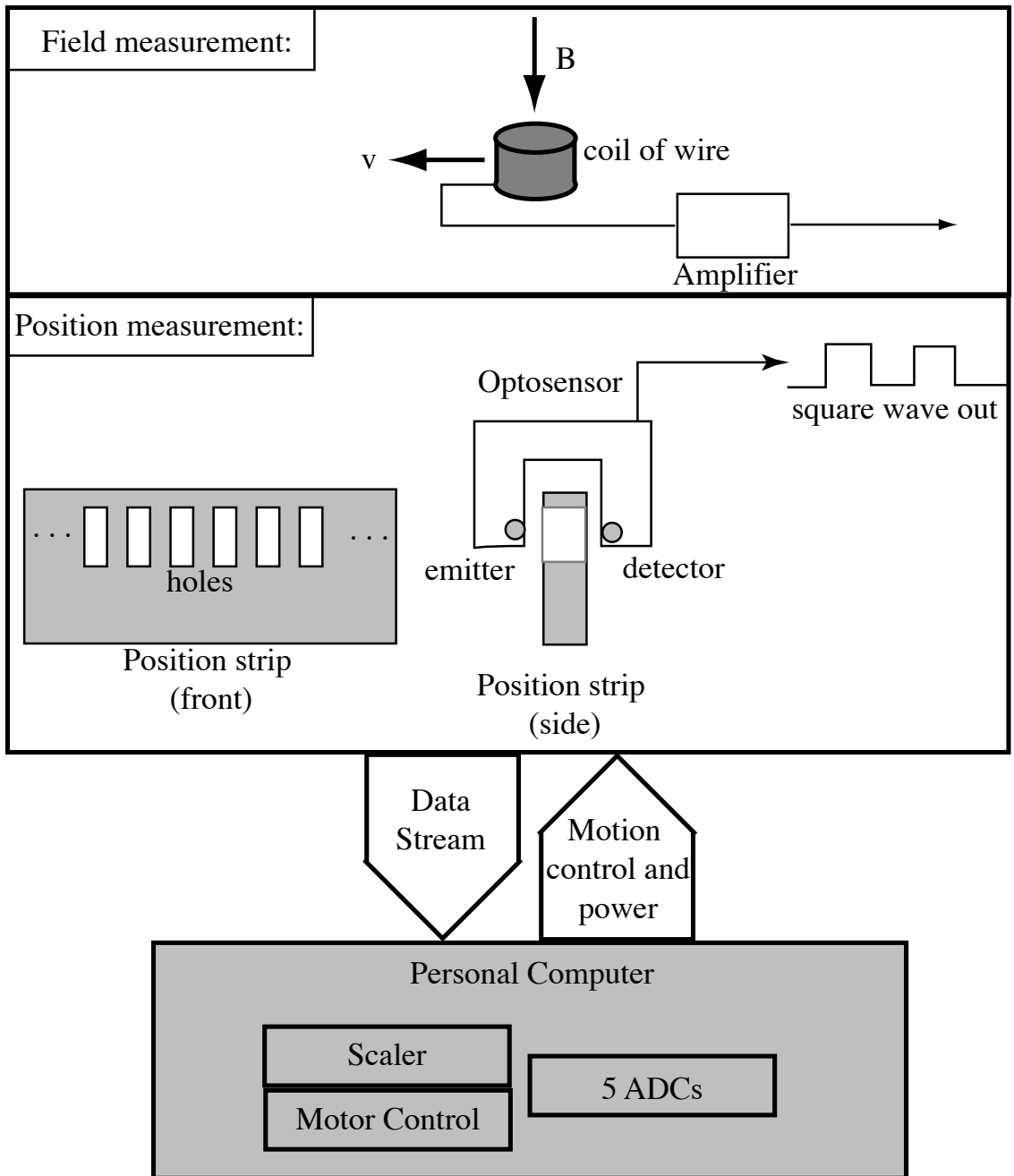


Figure 3.4: Schematic of the mapper DAQ system. The PC supplies commands to the motors and power to the on board electronics and controls event timing. The optosensor on the cart reads holes in the position strip and sends a square waveform back to the PC for position and timing information.

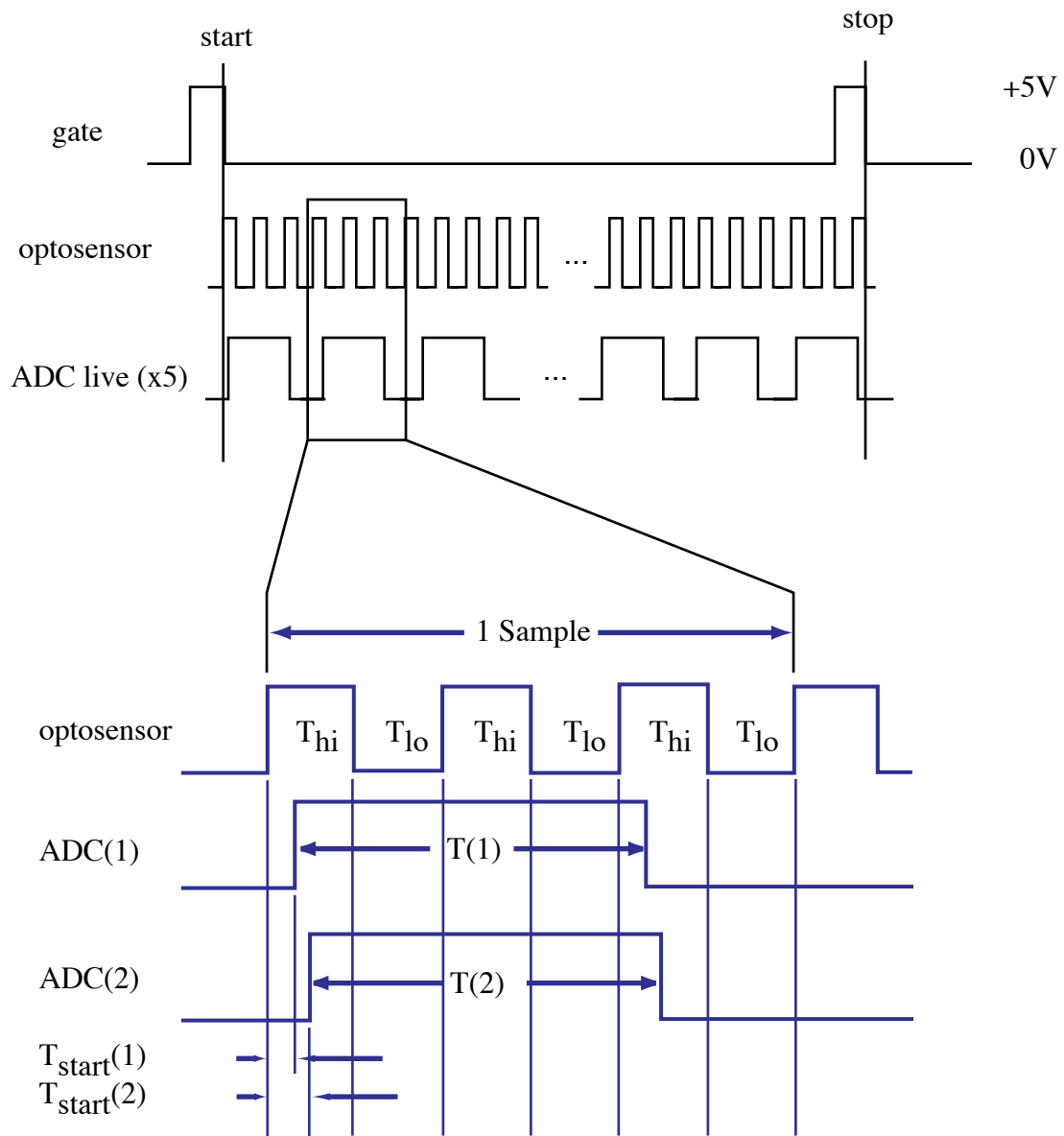


Figure 3.5: Timing diagram for one pass through the magnet. The gate signal is generated when the cart passes a certain point and tells the PC to start or stop acquiring data. As the optosensor passes the teeth in the position strip, it generates a square wave. Field measurement is broken up into 3-tooth (0.090") samples. T_{hi} and T_{lo} are the times that the waveform is spent in the high or low state, respectively. $T(1)$ and $T(2)$ are the live times for the ADC's. $T_{start}(i)$ is the time it takes to start the ADC's following detection of the first tooth in the sample. All the times mentioned are measured by counting 1 μ s clock ticks using a stopwatch circuit.

In the gap of the dipole, the springs on the bottom four wheels pressed the cart (side with rigid wheels) firmly against the pole-tip steel, which is very flat, ensuring that the coils stayed in the same vertical plane. In the fringe field region (outside the gap), the coils were constrained by an aluminum plate bolted to the aluminum frame. This plate was held 6.000 ± 0.005 " apart, and shimmed such that the coils remained coplanar with their paths in the gap. For example, the midplane coil remained on the midplane throughout its path inside and outside the magnet gap. The cart was propelled through the dipole gap by a plastic chain connected to a stepper motor. The plastic chain made a loop between a gear (attached to the driving motor) and a sprocket. The chain was fixed to the cart at roughly its center of mass.

3.2.2.2 Induction coils

The induction coils used for field measurement consist of very fine (42 gauge or 0.001" diameter) wire spooled around a bobbin. The height of the bobbin was 0.5", but the spool of wire was only 0.375" tall. The wire was wrapped very tightly with a final diameter of 0.375". The wires were copper, and given their diameter and resistance (5-10 kilohms), means they were miles in length, providing a large voltage signal (~0.7 Volt for a field gradient of 60 Gauss/mm). There were five of these coils, one on the magnetic midplane, one below and three above.

3.2.2.3 Analog-to-digital conversion

The ADC's were printed circuit modules designed for use in a personal computer. The ADC chip was an Analog Devices model number 1170. The exact workings of the chip are proprietary, but according to the manufacturer they operate roughly as voltage-to-frequency converters. The voltage is digitized into 24 bits, with the last four being

essentially unusable. The input range is -5V to 5V.

3.2.2.4 Electronic noise suppression

The voltage induced on the coils is 0-1 Volts for the typical field gradients present during the normal operation of the dipole magnets. Because the ADC's resided in the PC, they were subject to substantial electronic noise from various operations in the computer such as RAM and hard drive access. Typical peak to peak noise present at the inputs of the ADC from such sources was 300 mV. Because the ADC's were set to have a fairly long integration time, $T_{int}=16.67$ ms, most of the noise was suppressed.

Several steps were taken to reduce the noise level, and thus enhance the signal to noise ratio. They were shielding, cooling, elimination of noise sources, and amplification of the raw signal. Removing the switching power supply from the PC helped substantially. The supply was replaced with a different (non-"switching") supply whose highest frequency component was 60 Hz.

Cooling the ADC's also provided some noise relief. This was achieved by cooling the entire PC case to approximately 5° C. This reduced the fluctuations in the output ADC voltage by a factor of two. Replacing the AD1170 chip itself (if it was more than 1 year old) also had the effect of cutting the noise in half.

An simple amplification circuit with adjustable gain and offset was designed to bring the level of the input signal above that of the PC noise. Since the PC noise is constant (not amplified), simply amplifying the input signal will increase the signal to noise ratio. Consequently, the signal to noise ratio increased by a factor of 7-30 depending on the field setting.

3.2.2.5 Position and time measurement

The positions and times of the field measurements necessary for field integration were obtained by reading teeth from a small strip with a comb-like structure (see Figure 3.2). The strip had 0.010" x 0.25" rectangular holes regularly spaced at a distance of 0.030". The length of a three-foot section was measured and was reproduced to 0.002". A transmissive optical sensor was used to detect the teeth in the strip. The optosensor contained a small, collimated infrared photodiode on one side of the strip, and light from it was detected by a small (also collimated) photo-transistor placed on the other side of the strip. The output of the transistor (0 or 5 Volts) was supplied to the input of a fast schmitt trigger. The output of this chip is a square wave (rise time and fall times $< 2\mu\text{s}$). The rising and falling edges of the wavetrain then translate into position information.

Two strips provide the radial and azimuthal coordinates of the coils at all times. The azimuthal strip was mounted near the center of the aluminum plate and was read continuously as the cart passed through the magnet. The radial strip was mounted on the cart. These measured positions are relative to an arbitrary starting point on the aluminum frame. Absolute position measurement (reference to the magnet steel, for example) is necessary for final field analysis. This will be discussed later.

The time measurements for the field integration in the azimuthal direction were made by timing the cart between the teeth on the strip. A stopwatch circuit was established to measure the time spent in the high (+5V) and low (0 V) portions of the wavetrain from the optosensor. The stopwatch counted 1 μs clock ticks while the waveform was in a high or low state. In addition, the integration time from the ADC's was measured. The ADC's provide a gate signal to indicate when they are busy taking data, and the scaler board

counts clock ticks while this gate signal is active (Figure 3.3).

3.3 Post processing and data conversion

The objective of the post processing software was to interpret the raw data, make corrections where necessary, and provide the magnetic field values on a cartesian grid in the magnet's coordinate system. As mentioned before, the input requirements of the chosen optics code COSY demand that the field be in cartesian coordinates. The user is given several options including alignment, calibration, interpolation and smoothing. These are passed to the program through an input file which includes the location of the calibration data files. The output is a file written in binary format which is zero suppressed to conserve storage space. Appendix A gives the relevant details regarding input and output file format.

3.3.1 Raw data

Figure 3.6 is a plot of the raw voltage and time data for a typical sweep through the magnet. It is clear from the figure that the cart's speed was not uniform during its motion. This is caused by the propelling chain stretching like a spring. The cart then bounces as it passes through the magnet.

3.3.2 Dead time correction

The product of the voltage with the integration time gives the differential field element for that sample. If the ADC's could integrate continuously with no dead time, simply summing the products of these voltages and times would yield the field value at the end of each integration period. This is certainly the preferred method, as it is largely independent of the speed of the cart.

Correcting for dead time would be simple if the speed of the cart was constant or

slowly changing. Unfortunately, this was not the case, as is shown in the Figure 3.6. When comparing two identical sweeps through the magnet it was seen that the field differences were largest in places where the motion of the cart differed greatly from one pass to another. This large difference was attributed to insufficient position resolution during the testing phase. During the production mapping phase, the position strip was read at every tooth, in effect tripling the position resolution.

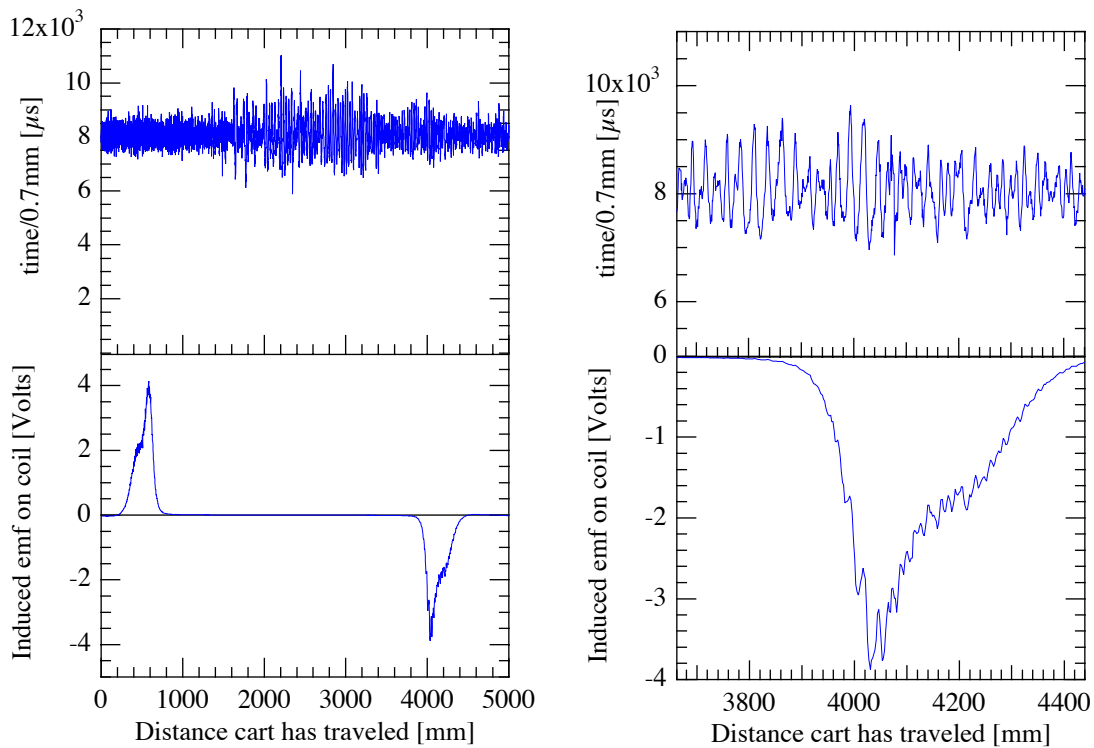


Figure 3.6: Raw data from one pass through the D1 magnet at 1.6 Tesla. The top panel is the time it takes the cart to travel 0.762 mm at a radius of 2.7 m for each field sample. The bottom panel is the raw voltage output from the ADC. The cart oscillation causes the oscillations in the measured voltage, better seen in the right half of the figure.

The variation in the speed of the cart also causes a change in the response, since the voltage induced is proportional to the speed. The first correction was to multiply the sample voltage by the ratio of the sample time to the integration time, essentially a speed normalization. The second correction was to compute precisely where the sample occurred, then the normalized voltage was interpolated to the center of the sample as if there was no dead time. This method was superior to computing the missed voltage and adding it to the sample.

3.3.3 Accounting for missed field data

To make post processing easier, the field measurement was taken on a regularly spaced polar coordinate grid. The goal was to have a field measurement every 2.3 mm (radial) and 0.05° (azimuthal). One unfortunate consequence of the vertical geometry of the dipoles was cart oscillations. Occasionally the speed of the cart was too fast for an integration (and subsequent conversion) to finish before the next regularly-scheduled sample was supposed to start. In this case, the sample was skipped and marked, then data taking resumed at the next regular grid point. (This is referred to as a bad sample.) The position and voltage information from surrounding samples was used to perform a 3rd order interpolation over the missed data.

3.3.4 Voltage offset correction and sweep alignment

The voltage offset from the electronics must be removed to determine the true induced voltage. This is necessary and important because it can affect the field calibration by more than 10 Gauss. By subtracting the forward and backward passes from each other, it was possible to determine this offset by fitting a line to the region of the map inside the steel (away from the fringing fields). This process also facilitated the alignment of forward

and backward passes at the same radius, because the difference of two raw sweeps is proportional to the first derivative if there is a position error. The passes were aligned by shifting one of the passes relative to the other until the difference held no peak like structures. The two sweeps then have the same coordinates.

3.3.5 Field calibration

Once the raw data was converted and corrected, the field strengths needed to be calibrated. The field measurements were calibrated using a combination of Hall probe and NMR probe data. Figure 3.7 shows the location of the probes during field measurement.

Because the fields are the integral of the voltage data, an integration constant needs to be added to the field at all points; this is the field strength at the starting position of the coil. The starting field strength was measured at the starting point of the coils at 1" intervals with a Hall probe, then the data was fit with a fifth order polynomial (Figure 3.8). The polynomial was used to determine the field strength for each starting position (2.3 mm pitch).

Figure 3.9 shows Hall probe and NMR probe data for D1 and D2 for all field settings used during the mapping campaign. The excitation functions for the two magnets differ slightly at high fields. This is due to the location of the power supplies and how the current is measured. The current through the cables coming from the power supply creates a significant and measurable magnetic field around the supply cables. The current is inferred by measuring the field it creates around the supply cable. Any other magnetic fields present, such as the ones from the magnets themselves, can affect this measurement. The power supply for D1 is very close to the magnet steel. At high field settings, stray fields from the magnets affect this current measurement.

NMR measurements were used to determine the absolute field strength at known locations in the magnet polar coordinates (r, θ, z) , placed to coincide with the location of the NMR probe during S800 experiments (midplane only). The measurements were made at five z locations, one for each coil, and were accurate to better than 0.1 Gauss. Once the dead time corrections were applied and the field integrated along the coils path, the uncalibrated field $F(r, \theta, z)$ is known at the calibration points.

The field was fit as a function of radius at the NMR angular location to eliminate the small fluctuation error in the field. The calibration value was then taken from the polynomial value at the NMR location rather than the raw data value. This provides a more reliable calibration and ensures that the measurements fluctuate around the correct central value. A scaling factor can then be determined based on the set of NMR and Hall probe measurements, as follows:

$$S = \frac{B_{\text{nmr}}(r_{\text{nmr}}, \theta_{\text{nmr}}) - B_{\text{hall}}(r_{\text{nmr}}, \theta_{\text{start}})}{F(r_{\text{nmr}}, \theta_{\text{nmr}}) - F(r_{\text{nmr}}, \theta_{\text{start}})} \quad (3.3)$$

and the calibrated fields are then given by

$$B(r, \theta) = B_{\text{hall}}(r, \theta_{\text{start}}) + S \cdot (F(r, \theta) - F(r, \theta_{\text{start}})) \quad (3.4)$$

3.3.6 Position calibration

Absolute position calibration was achieved by mapping small, strong, permanent magnets located on the steel edge. The magnets are 1 cm x 1 cm wide and 2 cm long and have a pole tip strength of ~ 0.5 Tesla. The magnets were placed in holes in the mapper plate and fixed firmly to the magnet steel edge by their magnetic attraction. The small permanent magnets are mapped individually, then the residual field from the magnetization of the spectrograph magnet steel is subtracted to reveal just the field due to the magnets. This procedure is also used to align the induction coils to each other as well

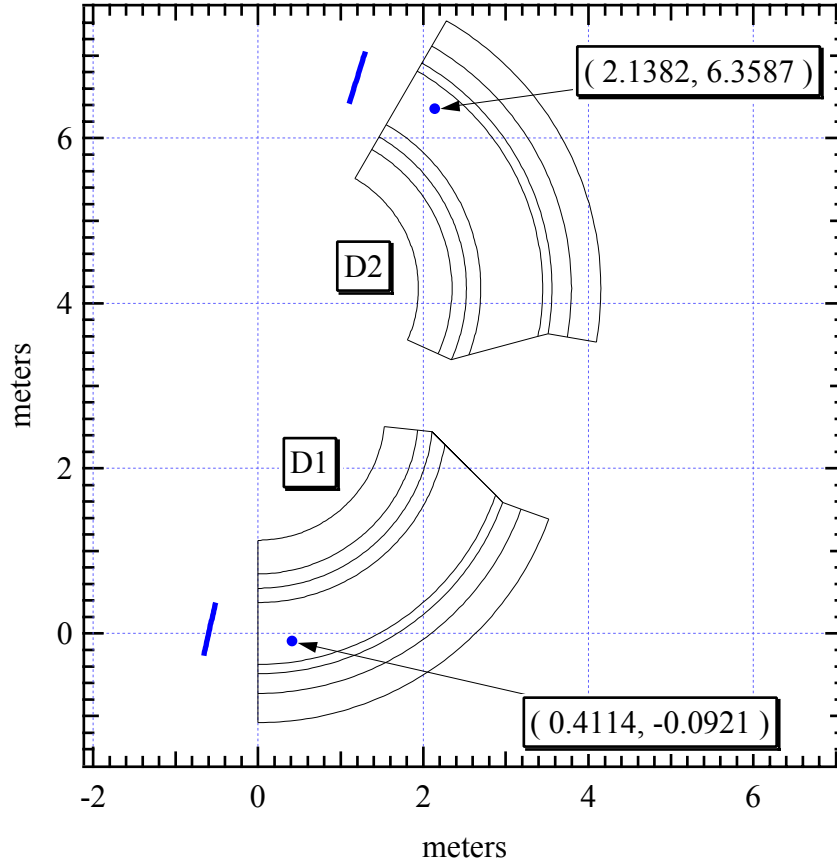


Figure 3.7: Position of Hall probe and NMR probes for magnetic field measurements. The thick lines are the locations of the Hall probe measurements; the dots are the location of the NMR probe measurements. The origin of the coordinate system is at the center of the entrance to the D1 magnet.

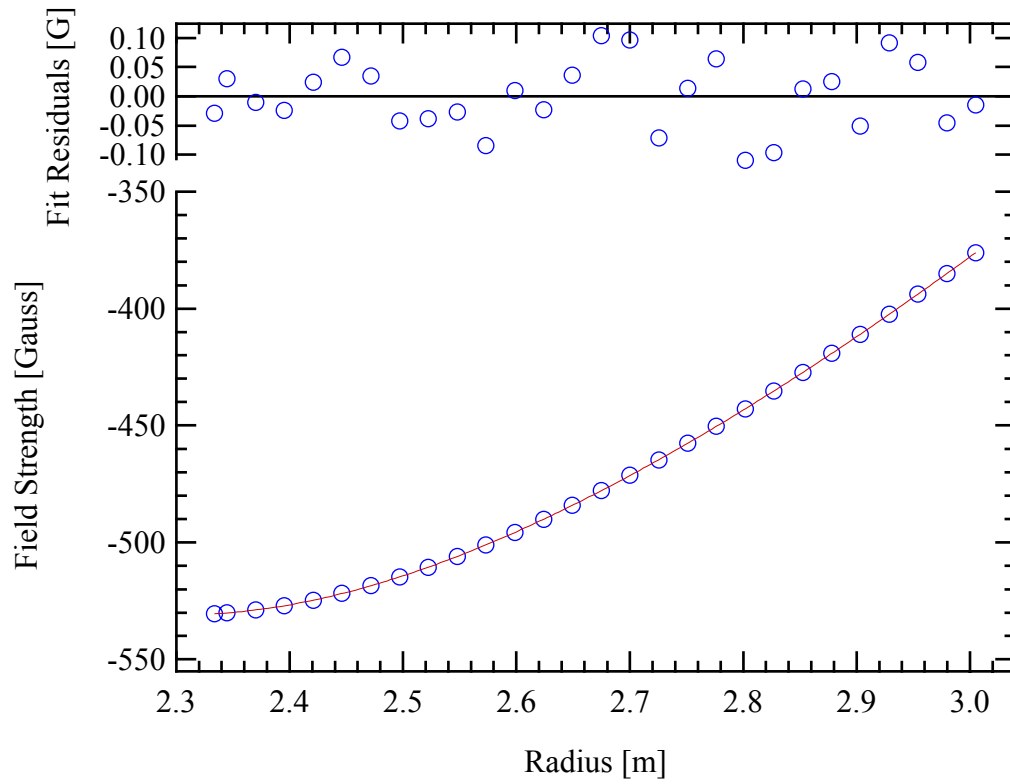


Figure 3.8: Hall probe data for D2 at 1.6 Tesla. The line through the data is a 5th order polynomial fit. The fit residuals are all < 0.1 Gauss.

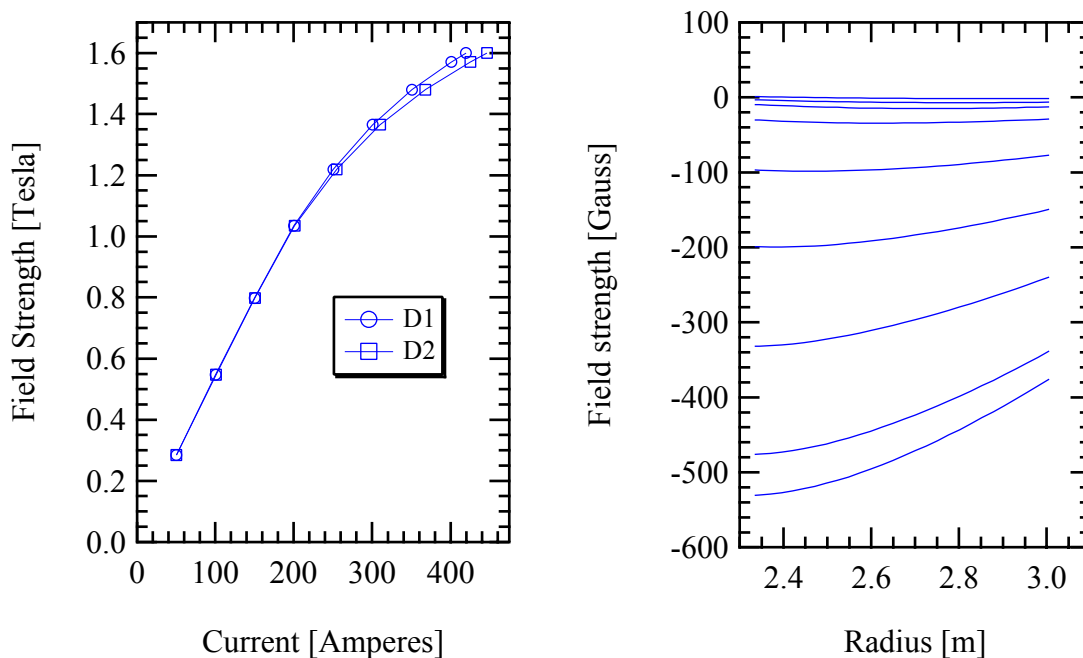


Figure 3.9: Left: Excitation functions for D1 and D2 determined from NMR measurements. Right: Field strength as a function of starting radius for D2 determined by Hall probe measurements. The fields range from 0.28 T (top) to 1.6 T (bottom).

as to the magnet steel. Figure 3.10 shows three such magnets placed on the edges of the D1 magnet steel and mapped. Following alignment of the maps with the steel, the magnets were in their expected locations of 5.0 ± 0.5 mm from the steel. This error alone will not degrade the energy resolution and is within specifications for maintaining 1 in 10,000 energy resolution [Zh97].

Position errors are always possible at some level. The frame was designed to have the same arc center as the magnet steel. However, small translational or rotational errors can occur when placing the mapper in the steel. Careful alignment ensured there was no rotational error for D1 or D2. There was a small translational error of 5.9 mm for D1.

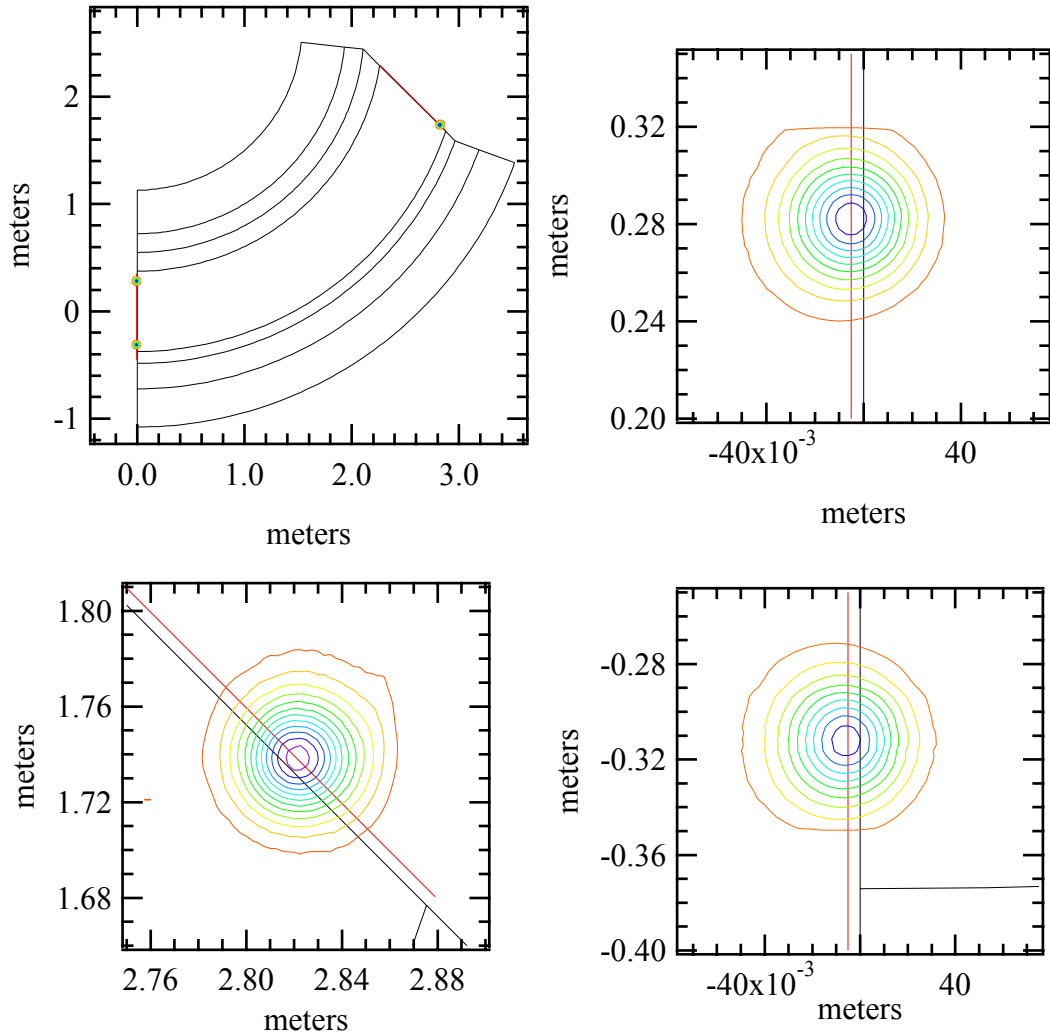


Figure 3.10: Field measurement of small permanent magnets placed on the D1 magnet steel. The magnets are 1cm x 1cm x 2cm long. The top left panel shows all the magnets. The lines through the centers of the circular contours are 5mm from the magnet steel edge.

3.3.7 Smoothing

Smoothing of the data was sometimes necessary for two reasons: (1) to provide the MF element in COSY with usable maps and (2) to provide accurate interpolation from the polar coordinate system to the cartesian coordinate system. COSY takes midplane field data and performs an off-midplane expansion to determine the fields everywhere in the

gap of the magnet. Even small (<1 Gauss) high-frequency fluctuations get magnified in the derivatives. Higher order terms in the transfer map then tend to diverge to meaningless numbers. Thus smooth data with smooth derivatives is desired.

The data provided to COSY is in a cartesian coordinate system, so the data is interpolated from polar coordinates to cartesian coordinates. Simulations prove that the field error following interpolation is greatly magnified when there is noise in the data and are of the order of the noise level. The smoothing process minimizes these errors.

The smoothing techniques use neighboring points to compute a weighted average at a specific data point, as follows:

$$S = \sum_{i=1}^N c_i \cdot B_i \quad (3.5)$$

where S is the smoothed result, c_i are the weighting coefficients used and B_i is the raw field values at the points. There is more smoothing with higher N. All these techniques essentially act as a filter to remove high frequency components of the field fluctuations.

Three types of coefficients were made available to the user in the post processing software: Savitzky-Golay, binomial, and Gaussian. The Savitzky-Golay weighting coefficients are a parabola with its extremum point at the center [Pr92]. The binomial weighting coefficients are just numbers taken from a binomial distribution [Ma83]. The Gaussian method uses a Gaussian distribution of coefficients and is exactly the process described on page 33 of the COSY manual [Be95], with a twist. The width of the Gaussian depends on local derivatives; higher derivatives mean a smaller width and vice versa. The Savitzky-Golay smoothing tends to preserve higher order derivatives more accurately and is very fast. The binomial and Gaussian methods smooth more effectively but may inaccurately

reproduce 2nd and higher order derivatives.

3.4 Results

The production maps were taken at several current and field settings ranging from 0.25 to 1.6 Tesla, from 50 to 450 Amps. Tables 3.1 and 3.2 summarize the settings used while acquiring production field maps. D1 was mapped separately from D2, but with D2 at the same central field value. The mapper was then removed from D1 and installed in D2. D2 was then mapped with D1 at the same central field value.

Raw sweep data show smooth, continuous behavior. However, RMS sweep-to-sweep differences exist at the level of ± 0.0006 Tesla at the highest fields of 1.6 Tesla. These could be interpreted as higher order aberrations by COSY, and their elimination is desired.

The data were interpolated onto the cartesian grid by means of a second order polynomial. This had a smoothing effect on the data and was determined to be as accurate as interpolation within the errors of the maps. In fact, this is more accurate for noisy data than interpolation. Choosing a larger number of points in the fit had a larger smoothing effect.

Figure 3.11 shows midplane data taken for the B=1.50 Tesla setting for each of the magnets in the magnet coordinate system. Figure 3.12 shows two separate field maps for D2 close to the maximum strength of the field. The field profile is very flat in the central magnet region for low field settings, but significantly curved at the highest field setting. All contours in the figure are separated by 1 Gauss. No rapid fluctuations from measurement errors remain in the maps, which is a result of the smoothing process.

Table 3.1: Mapping parameters used during D1 production maps.

D1		D2	
I [Amperes]	B [Tesla]	I [Amperes]	B [Tesla]
67	0.25463	50	0.25463
111	0.54328	100	0.54328
167	0.79567	149.9	0.79567
199.2	1.02964	199.9	1.02964
250.7	1.22031	255.0	1.22031
275.7	1.29650	282.3	1.29650
300.9	1.36513	310.3	1.36513
350.9	1.47982	368	1.47982
366.0	1.50819	385.1	1.50819
381.1	1.53601	402.7	1.53601

Table 3.2: Mapping parameters used during D2 production maps.

D1		D2	
I [Amperes]	B [Tesla]	I [Amperes]	B [Tesla]
50.0	0.28421	50.3	0.28421
100.2	0.54741	100.7	0.54741
150.3	0.79840	150.4	0.79840
200.5	1.03484	201.3	1.03484
250.6	1.21966	254.7	1.21966
300.8	1.36506	310.2	1.36506
350.9	1.47998	368.0	1.47998
401.1	1.56973	425.3	1.56973
419.7	1.60008	446.5	1.60009

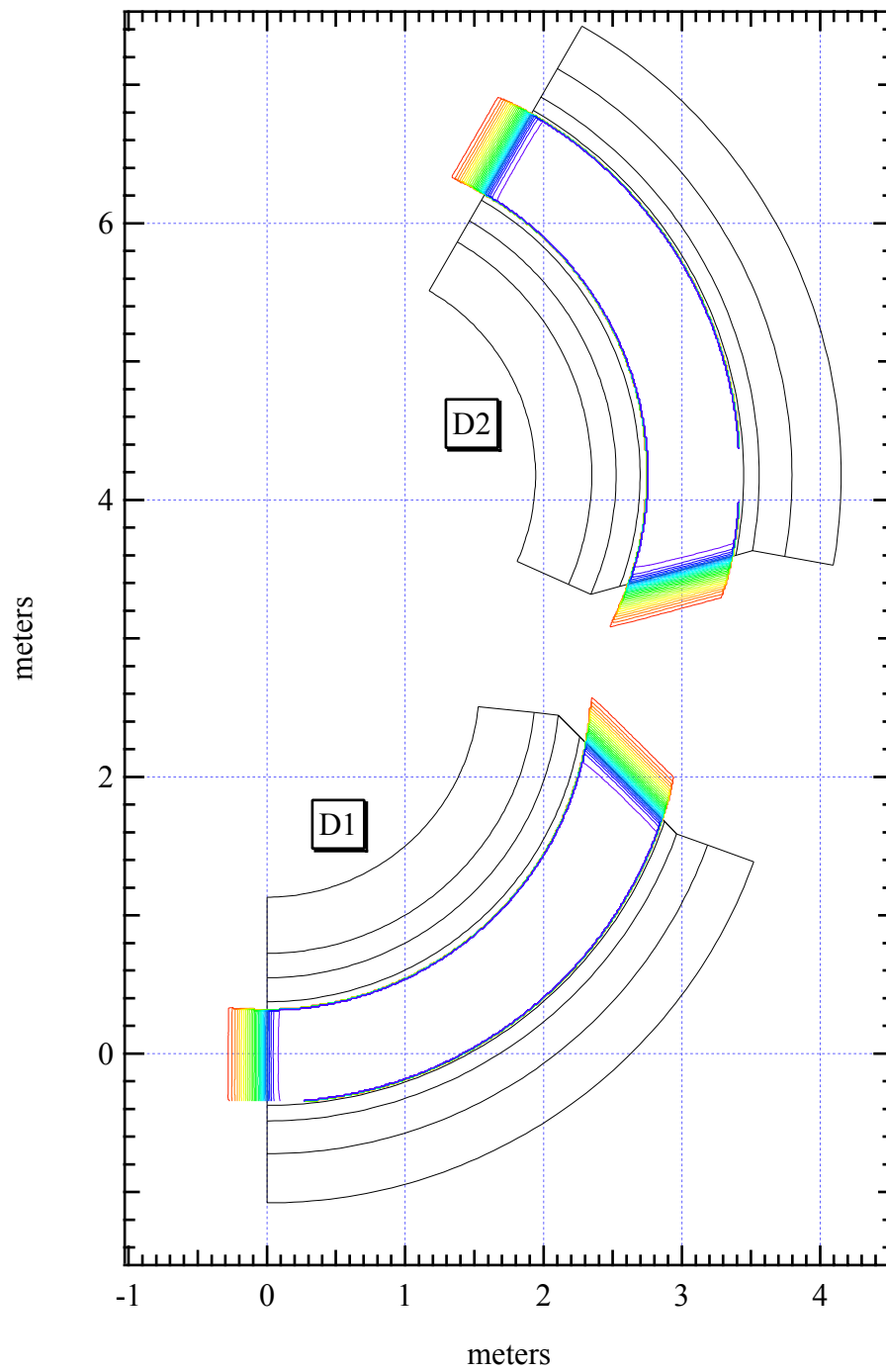


Figure 3.11: Dipole magnetic field data for both spectrograph dipoles. The current through the coils was ~ 350 A for both, giving fields of 1.48 Tesla for both D1 and D2.

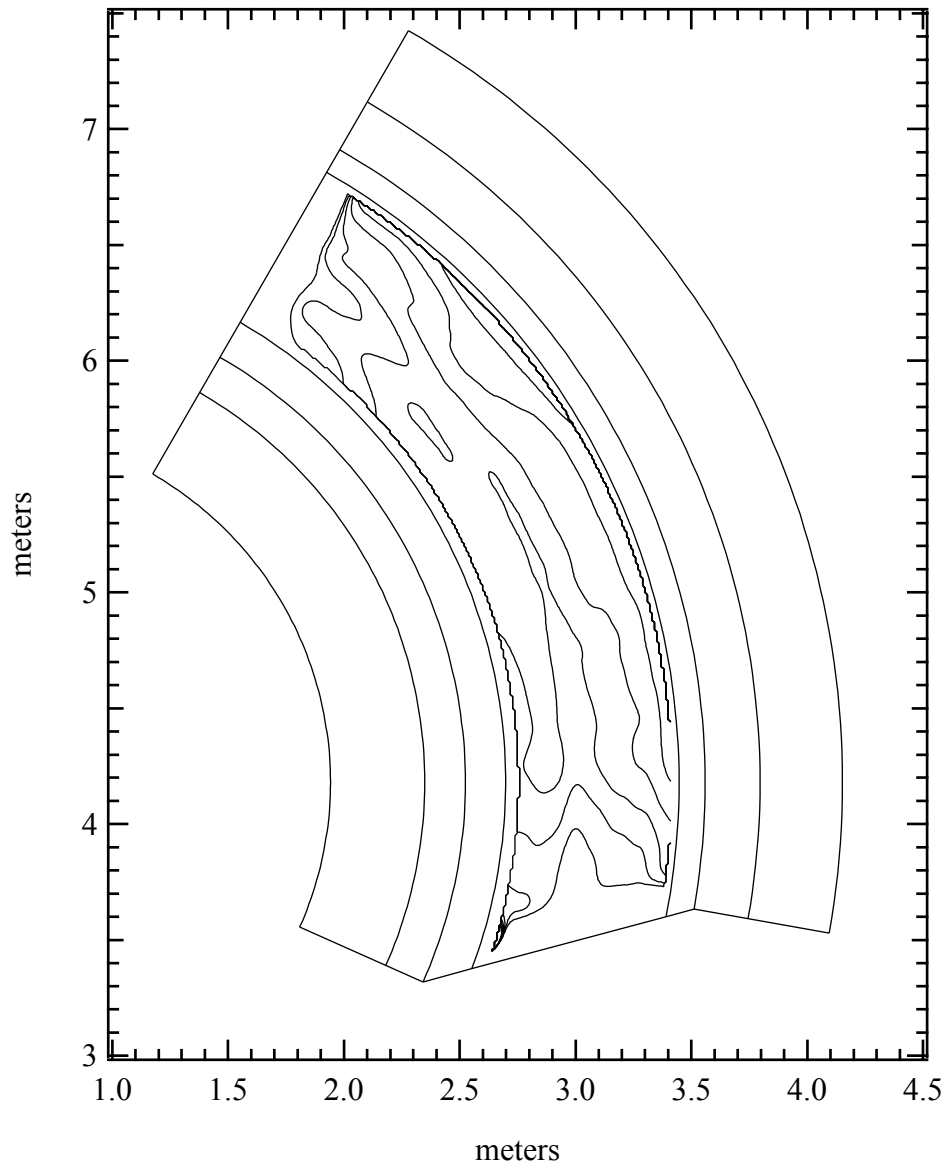


Figure 3.12: A D2 field map at 0.28 Tesla, plotted above 99% of the field strength. The contours are separated by one Gauss, indicating a very flat central field.

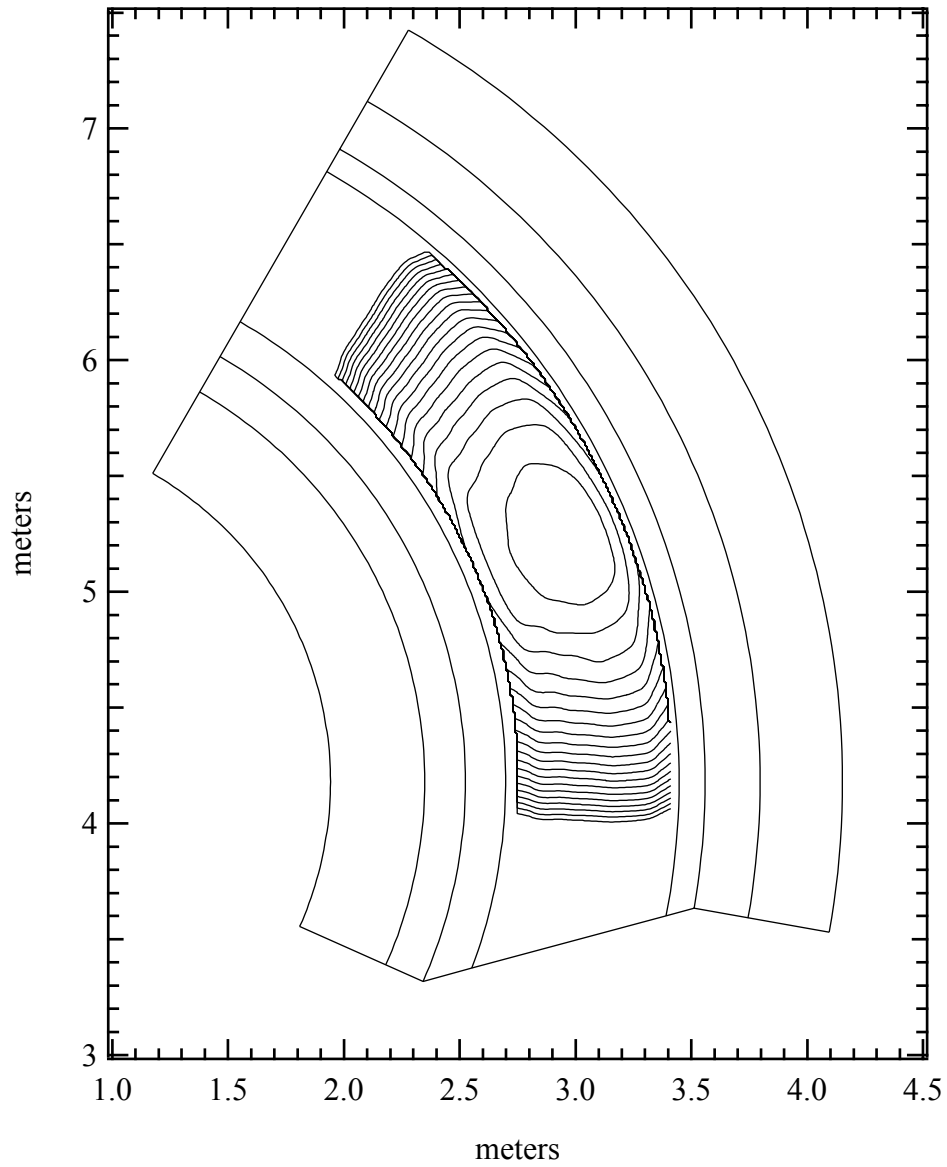


Figure 3.13: Field measurements for D2 at 1.6 Tesla. All contours are separated by 5 Gauss. In sharp contrast to Figure 3.12, the field exhibits a bowing behavior characteristic of saturation effects.

Figures 3.14, 3.15, and 3.16 show some interesting characteristics of the field data. Figure 3.14 shows that larger currents produce fields with opposite sign outside the magnets, making the particles bend first one way, then the other. The central field also becomes more bowed with higher field settings, a prominent saturation effect. Figures 3.15 and 3.16 show the D2 magnetic field profile and its derivatives through order along the reference trajectory for the lowest and highest field settings. The derivatives are somewhat smooth, but start to get noisy at 3rd order. The influence of the coil is greatly pronounced in Figure 3.15 compared to Figure 3.16. This is easily understood; the current in the coil is nine times greater, but the central field is only six times greater, due again to saturation of the magnet steel.

The mapping served to verify general characteristics about the magnets. It also provides a check on the magnet construction. The edge angles of the steel, the effective lengths, and field gradients can be measured with the maps.

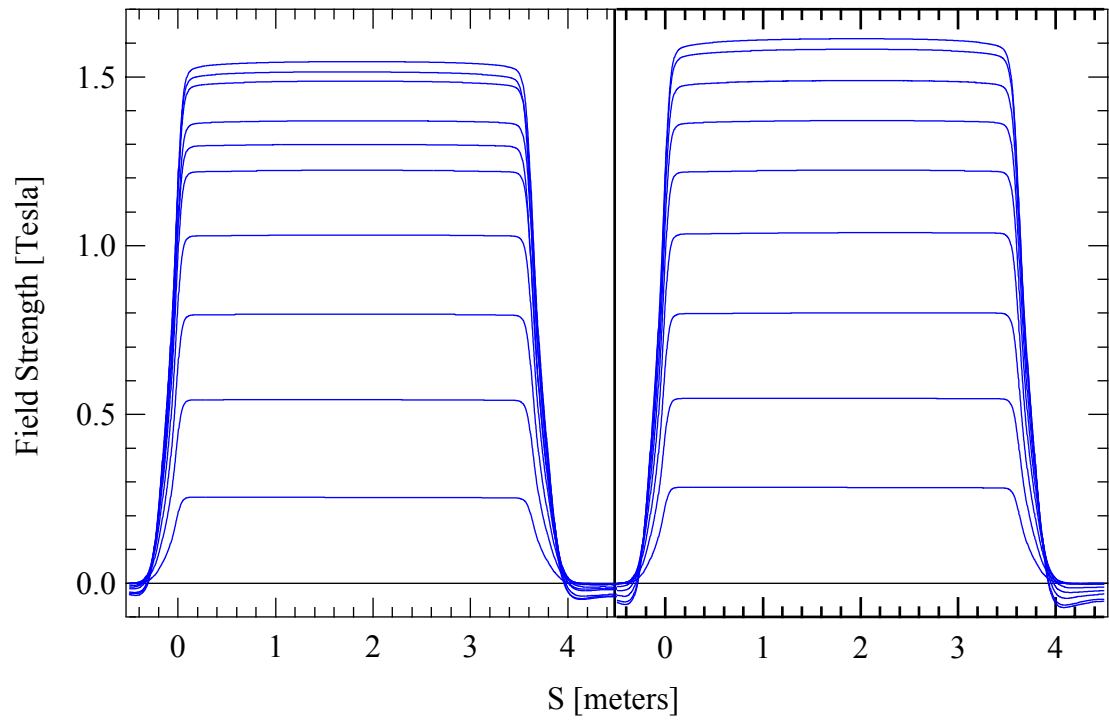


Figure 3.14: D1 (left) and D2 (right) magnetic field strength along the reference trajectory for the field settings from Tables 3.1 and 3.2. The curvature in the flat field region grows with field strength. The negative field just outside the coil also grows with field strength.

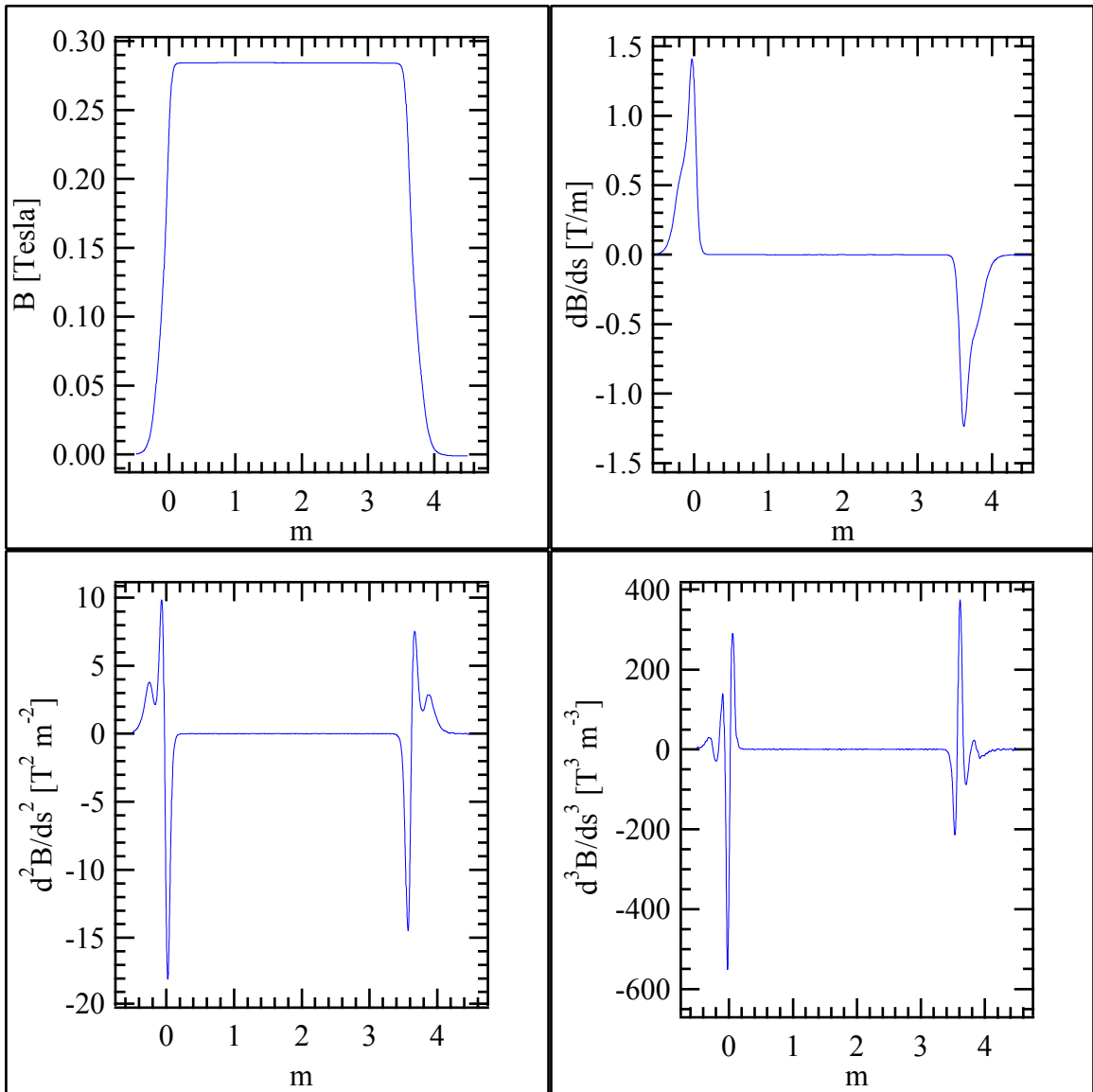


Figure 3.15: Magnetic field profile and derivatives along the reference trajectory for a D2 map at $B=0.28$ Tesla. The field profile is very flat in the center.

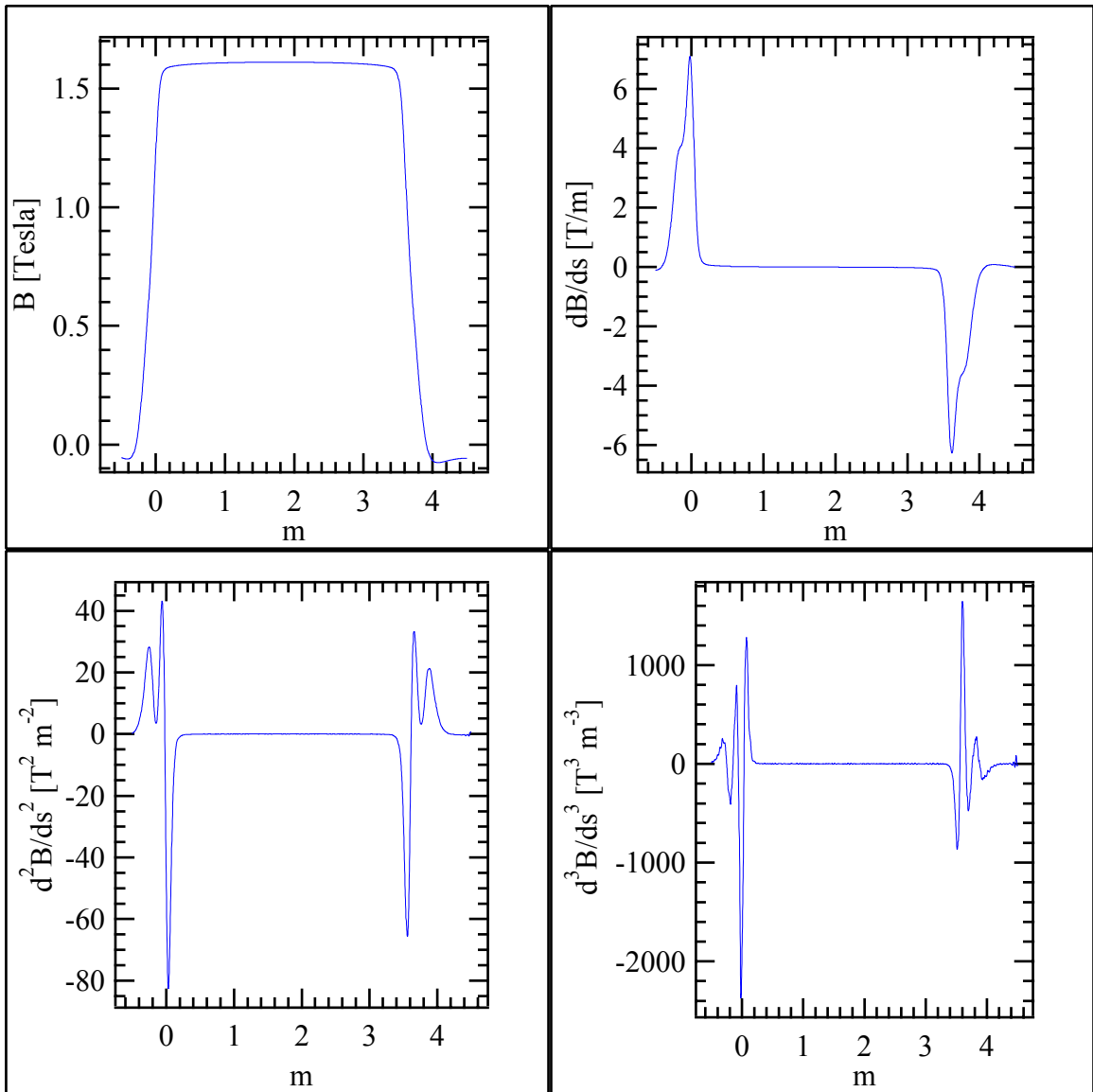


Figure 3.16: Magnetic field profile and derivatives along the reference trajectory for a D2 map at $B=1.6$ Tesla. The field is much more curved in the center than are lower fields. The effect of the coil is much more prominent than in Figure 3.13; the outermost shoulders in the first derivative are a larger fraction of the peak. The outermost peaks in the second derivative also demonstrate this effect.

3.4.1 Field curvature and gradients

The region inside the magnet steel is susceptible to field curvature due to the limited extent and susceptibility of the steel. Substantial field curvature was found to exist in the azimuthal (beam) direction. The curvatures are substantially higher at higher fields. Still, the field gradients in the flat field region of the dipoles are within design specifications. The curvature is normally defined in terms of an arc length, s , and its tangent angle, ϕ , as follows: $\kappa=|d\phi/ds|$. It usually has units of [length^{-1}]; the inverse of the curvature defines the radius of curvature at that point along the arc [Th84]. In this context, the curvature is defined as:

$$\kappa = \frac{\left| \frac{d^2B}{ds^2} \right|}{\left[1 + \left(\frac{dB}{ds} \right)^2 \right]^{\frac{3}{2}}} \quad (3.6)$$

where B is the field measured in Tesla and s is the arc length in meters.

Figure 3.17 shows the azimuthal field curvatures for all mapping settings. These were determined by making a second order polynomial fit to the central portion of the field. The first and second order coefficients were used as the first and second derivatives in equation 3.6. As the steel starts to saturate, the azimuthal curvature starts to grow exponentially. Figure 3.19 shows average radial field gradients for the mapping settings. These data exhibit strange behavior which is not understood. However, notice that the peak occurs close to the knee of the azimuthal curvature curve, perhaps suggesting a saturation effect.

The dipoles have normal (i.e., not superconducting) trim coils along their inner and outer radii to reduce the radial field gradients to tolerable, design (< 1 Gauss/cm) levels.

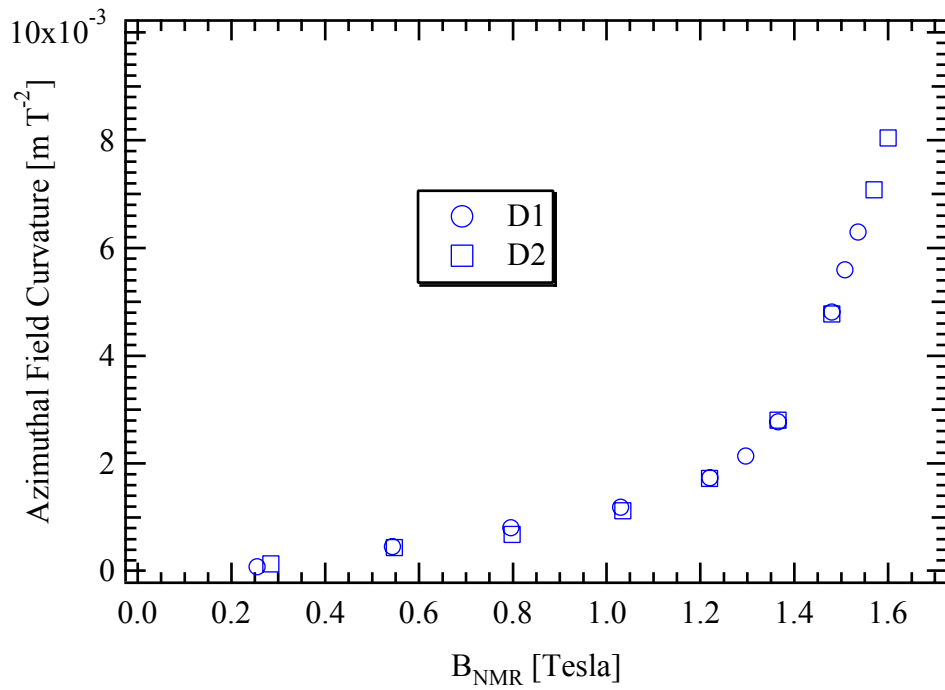


Figure 3.17: Azimuthal field curvature for some field settings used during the mapping campaign. Despite the high curvature at the largest field settings, the field gradients remain within design specifications (1 Gauss/cm).

During the test mapping phase, field maps were acquired with the trim coils on at their optimized settings ($I_{\text{trim coil}} = I_{\text{main coil}} * 0.4375$ [Ze93]) and with the trim coils at zero current. The trim coils have a pronounced effect on the radial field flatness in the region of usable field. Figure 3.18 shows a test map at 1.56 Tesla with the trim coils on and off. The radial field gradient is too high unless the trim coils are on and at their optimum setting.

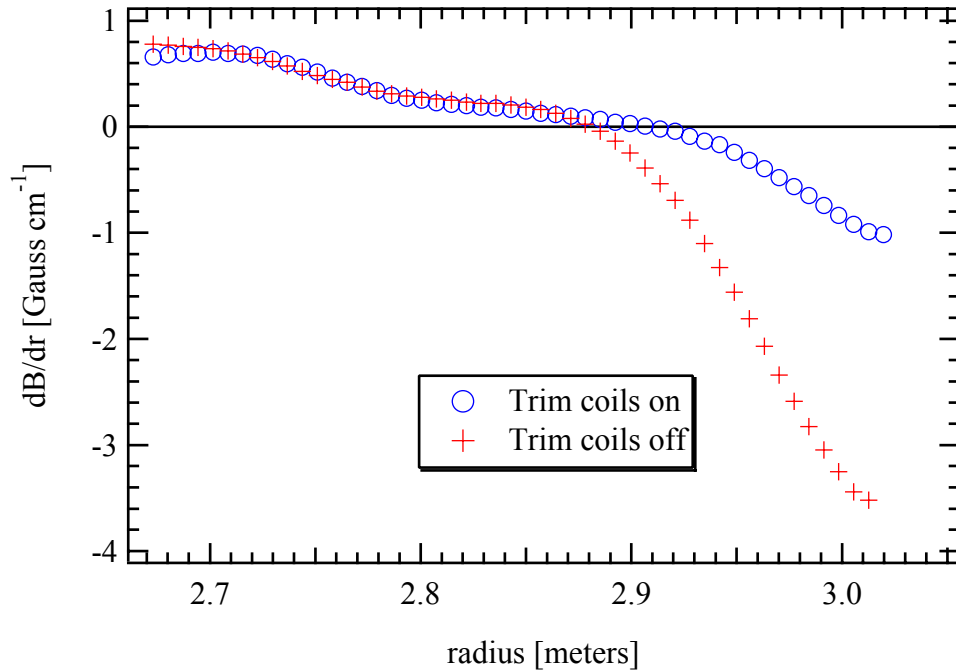


Figure 3.18: Measured radial field gradients in D1 with (+) the trim coils off and (O) the trim coils on at their optimized setting.

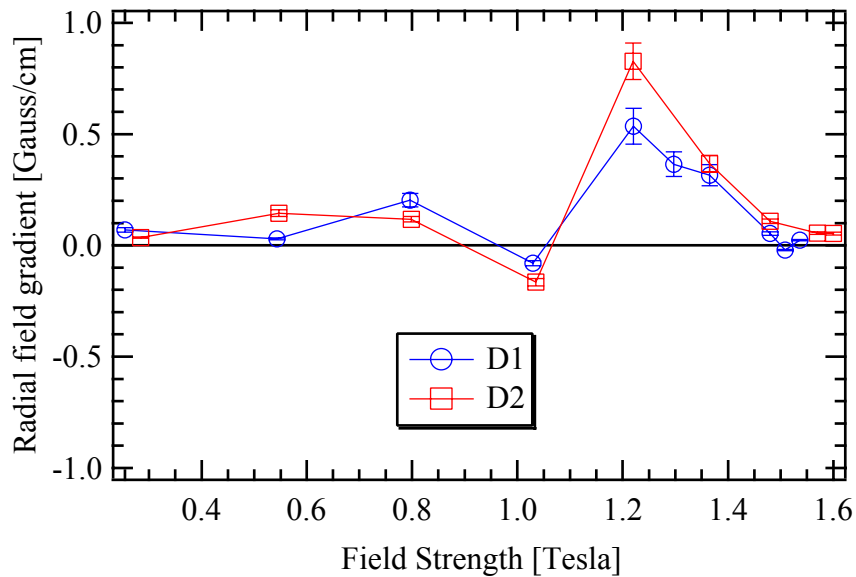


Figure 3.19: Average radial gradients measured for D1 and D2 during the mapping campaign. Despite the apparently erratic pattern, the general pattern is reproduced for both dipoles. The error bars are $\pm 15\%$. The design limit is 1 Gauss/cm.

3.4.2 Effective length

To determine the effective length of the dipoles, field data from the maps was interpolated onto the central, reference trajectory. The fringe fields of the dipoles effectively make them longer. The effective length was determined by performing a Simpson integration along this trajectory, then dividing the field integral by the NMR reading at that field setting. Figure 3.20 shows the measured lengths for D1 and D2 respectively.

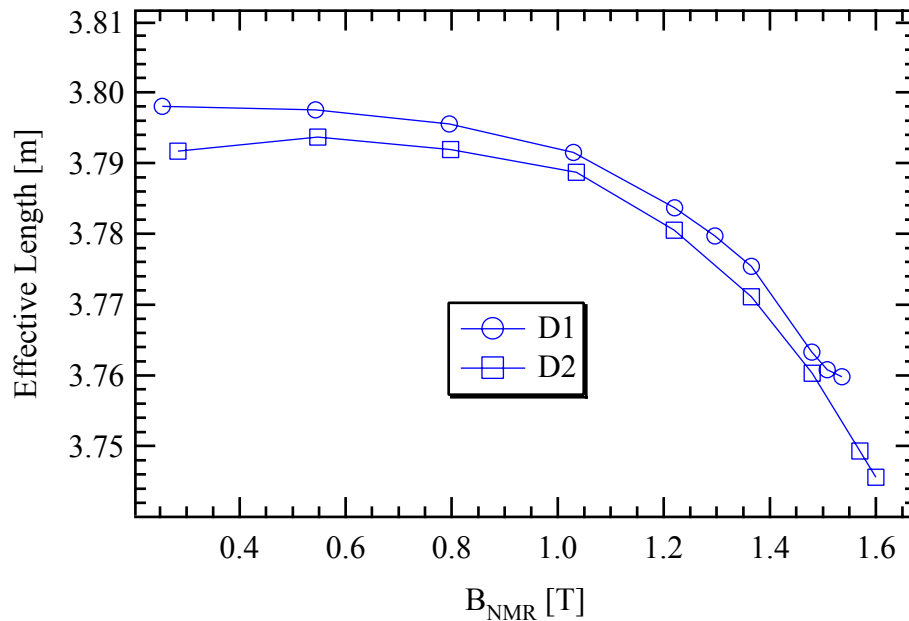


Figure 3.20: Effective length for both dipoles from field data, calculated by dividing the integrated field along the reference trajectory by the appropriate NMR reading (from Tables 3.1 and 3.2).

The strong field dependence of the effective length is typical of these types of magnets. Outside the magnet gap, the field contribution from the coil is opposite in direction. At higher fields, a higher current/central field ratio is necessary to account for saturation effects. This adds strongly to the negative field outside the magnet gap and is largely

responsible for this phenomenon.

3.4.3 Edge angles

The influence of saturation, finite susceptibility and other magnetic sources affect the edge angle measurements with field maps. Nevertheless, edge angles were computed for all of the midplane field maps. A straight line fit to a field contour ($B=0.4*B_{\max}$) at the entrance and exit edges determine the angles.

Table 3.3: Entrance and exit angles for the D1 magnet.

B_{NMR} [T]	Entrance[°]	Exit [°]	Difference [°]
0.25463	-0.005	29.73	29.735
0.54328	-0.07	29.70	29.87
0.79567	-0.04	29.79	29.83
1.02964	-0.07	29.86	29.93
1.22031	-0.09	29.75	29.84
1.29650	-0.08	29.76	29.84
1.36513	-0.05	29.72	29.77
1.47982	-0.07	29.71	29.78
1.50819	-0.05	29.69	29.74
1.53601	-0.14	29.64	29.78
Average =	-0.07±0.04	29.74±0.06	29.81±0.06

The entrance and exit angles as well as the angle between the two faces are listed in Tables 3.3 and 3.4. The averages and standard deviations are given in the last row of the table.

The slight lowering of the thirty-degree edge angle is possibly due to the increased influence of the other magnet and saturation effects or the limited extent of the steel on the faces. Using a different contour has a small effect on the measured angle unless very high or very low contours are used. This doesn't mean that the actual steel angle is different

from its designed 30° (in fact, this was measured to be 29.96° for each dipole). This can only be interpreted as a true magnetic effect due to the sum of magnetic sources.

Table 3.4: Entrance and exit angles for the D2 magnet.

B_{NMR} [T]	Entrance[°]	Exit [°]	Difference [°]
0.28421	-0.005	29.83	29.835
0.54741	0.005	29.83	29.825
0.79840	0.04	29.71	29.67
1.03484	-0.04	29.85	29.81
1.21966	-0.09	29.80	29.89
1.36506	0.01	29.74	29.73
1.47998	0.003	29.775	29.77
1.56973	0.007	29.77	29.78
1.60008	0.005	29.63	29.635
Average =	-0.01±0.04	29.77±0.06	29.77±0.08

3.4.4 Alignment of both dipoles

As a final check of the maps, Figure 3.21 shows two maps at the same field settings plotted in the overlap region between the two magnets. The contours are separated by 20 Gauss. The contours line up to better than 2 Gauss, indicating that the two sets of maps are aligned.

3.5 Conclusions

In the future, if one were to map these dipoles again, the best way to do it would be to use a zero dead time system, such as has been developed for the K500 cyclotron. The dead time correction used here, while accurate to ± 6 Gauss, is insufficient without substantial post processing effort. The most likely source of this error is the position measurement along the path. The optosensor is very sensitive to collimation of its light source

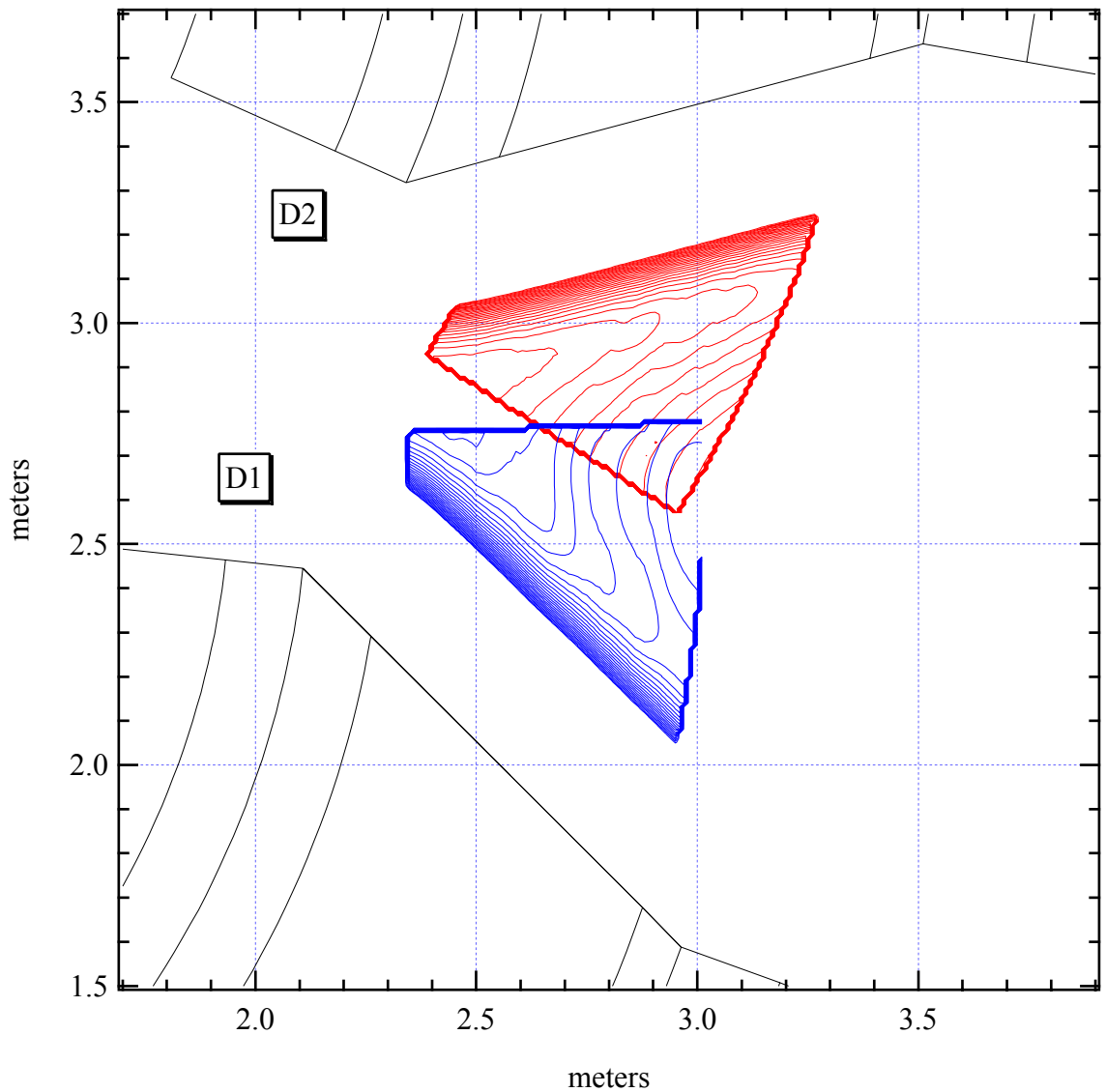


Figure 3.21: Contour plot of the overlapping field region of two maps at the same current and field settings. The contours are separated by 20 Gauss, and the region contoured is that ≤ 0.0 Gauss. The overlap of the contours is on the few Gauss level, indicating correct position and field calibration for the two dipoles.

and distance to the position strip from its light collector. Any variation in this distance (on the level of 0.01") can cause a change in triggering time, creating an error in position. Eliminating the dead time would reduce the dependence of the integrated field value on this position and may be enough to reduce the errors to the Gauss level as desired.

The data presented here were intended to be used in the MF element in COSY. Unfortunately, this method doesn't provide meaningful transfer maps beyond the 2nd order. Simulations show that the Gaussian interpolation (image charge fitting) used in COSY's MF element is adequate to describe the data at the 1 Gauss level at the 2.3 mm resolution used during mapping. However, this doesn't consider higher order derivatives, which may be unreliably described. Using larger image charge widths compensates for this somewhat, but then also fails to reproduce the fields in the regions with the largest gradients. Another possibility is that errors in the fields are just too large for reliable offplane expansion of the fields. This doesn't seem likely as the field fluctuation can be reduced to the ~1.0 Gauss level.

The good news is that the mapping illuminated various characteristics of the magnets that can be used in a field model representation of the magnets. The advantage to field models is that the higher order derivatives are continuous and, usually by definition, adhere to Maxwell's equations. The azimuthal curvatures, the radial field gradients, and the decrease in effective edge angles, as well as the fringe field data is very useful in determining a realistic model of the field. Thus, accurate transfer maps can be generated by simply using an accurate field model.

Chapter 4

Spectroscopy of ^{10}Li

4.1 Motivation

4.1.1 Halo nuclei

A nuclear halo is a simple quantum mechanical effect arising from low separation energy. This allows the valence nucleons to penetrate quantum-mechanically into the potential barrier, increasing the nuclear RMS radius appreciably. While stable nuclei have nearly identical neutron and proton radii, the distributions for halo nuclei can differ substantially. Neutron halo nuclei are those in which only the neutrons have a larger radius and similarly for proton halos. The differences in RMS radii can be as large as 6 fm or more. Nuclear halo states occur in nuclei having orbital angular momentum quantum numbers of $l=0,1$. For higher angular momentum, the states are more deeply bound due to the angular momentum term in the nuclear potential and hence the wavefunctions are more confined. Proton halos are also possible, but are less striking due to the added potential barrier provided by the Coulomb force. Several review articles describe the characteristics of nuclear halos [Ri92, Ha95, Or98].

Halos are of interest because of their inhomogenous structure and low nuclear den-

sity compared to stable nuclei. Most stable nuclei have a nuclear radius well described by $r=r_0A^{1/3}$, where A is their nucleon number and $r_0=1.2$ fm. Implicit in this scaling law is the fact that nuclear density is constant. Halo nuclei, by contrast, not only have substantially lower nuclear density but the nucleus is inhomogeneous. A core of normal nuclear density is surrounded by a halo of sparse nuclear matter. One can ask whether nuclear models that work well for stable nuclei, such as the shell model does, apply to such nuclei or whether the nuclear structure laws are different for these halo nuclei. By studying halo nuclei one hopes to answer these questions.

Neutron halos which have neutrons in s-wave states lead to even larger matter distributions than those in p-wave states owing to the lack of an angular momentum barrier. Consider an s-wave neutron bound by $S_n=100$ keV in a Wood-Saxon potential. Its asymptotic wave function is $\psi(r)\sim e^{-kr}$, with the characteristic length $k^{-1}=2\mu S_n/\hbar^2$, leading to an RMS neutron radius of ~ 11 fm, compared with 3.4 fm for $S_n=1$ MeV.

Another novel feature recently discovered in nuclei is the neutron skin [Ta92]. These are also extended nuclear matter distributions, like halos, but have distinctly different features. Unlike halos, they are characterized by proton and neutron RMS radii that differ by ≤ 1 fm and the matter in this skin is dense compared to halo matter. The skin is thought to arise from differences in proton and neutron Fermi energies; a larger difference meaning a thicker skin. Examples of skin nuclei are ${}^6\text{He}$ and ${}^8\text{He}$.

4.1.2 Lithium-11

Lithium-11 has been the subject of intense study in the last 15 years. It has been the most studied of the halo nuclei. The interest in halo nuclei and ${}^{11}\text{Li}$ was started by experimental results in the 1980's. Tanihata *et al.* used radioactive nuclear beams of 790

MeV per nucleon to measure total interaction cross sections [Ta85]. The interaction cross sections were surprisingly large for the neutron rich species ^6He , ^8He , and ^{11}Li . The deviation from the expected $r=r_0A^{1/3}$ value was much larger for ^{11}Li than either of the two helium isotopes. The nuclei were suspected of having extraordinarily large matter distributions and therefore low nuclear densities. This is in contrast to stable nuclei where nuclear densities are essentially constant.

Magnetic dipole and electric quadrupole measurements performed at ISOLDE at CERN in 1987 gave essentially the same results for ^9Li and ^{11}Li . This demonstrated that the proton distributions for ^9Li and ^{11}Li were very similar [Ar87]. This was interpreted as evidence that some or all of the neutrons, but not the protons, are responsible for ^{11}Li 's increased radius.

This was confirmed by Blank *et al.* [Bl92], who measured the interaction cross sections together with the charge changing cross sections. (A charge-changing reaction is any that changes the proton number of the projectile.) The $^{8,9,11}\text{Li}$ charge changing cross sections are shown to be constant while the total interaction cross section increased monotonically, again interpreted as evidence that the neutron distribution was responsible for the increased radii.

Kobayashi *et al.* found surprisingly narrow momentum distributions for ^9Li fragments following ^{11}Li breakup at 790 MeV/u [Ko88]. The sudden approximation is valid in high energy breakup and the fragment momentum distributions were interpreted as a direct measure of the intrinsic momentum distributions. In other words, the width of the fragment momentum distributions are inversely proportional to the extent of the valence wavefunctions; a narrow fragment momentum distribution corresponds to a large spatial

wavefunction.

In a case like ^{11}Li the neutrons in the halo have a much larger radius (~ 10 fm) than the ^9Li core (3 fm), and greater than 90% of the halo wave function is outside the core [Al97]. It is therefore appropriate but not necessary to use a three body model to describe ^{11}Li properties, where its properties are determined by the n-n and n- ^9Li interactions.

4.1.3 Lithium-10

Using a three body model to interpret the above experiments requires knowledge of its binary subsystems. The n-n interaction is well understood, but the n- ^9Li interaction is not. The ^{10}Li nucleus is an unbound system with a half-life of $\sim 10^{-21}$ seconds, making it difficult to study experimentally. A simple shell model suggests that the ground state character of the ^{10}Li system would be a neutron in the $0p_{1/2}$ orbit coupled to the $3/2^-$ ground state configuration of ^9Li leading to two states with 1^+ and 2^+ character. However, it was suggested as early as 1977 that the ground state character of the ^{10}Li system might mimic that of ^{11}Be [Ba77], in which an s-wave intruder state (the $1s_{1/2}$) drops below the $0p_{1/2}$ orbit giving rise to 1^- or 2^- states.

The ^{11}Li breakup data also suggest at least some component of s-wave in the ^{10}Li ground state. The unexpectedly narrow momentum distributions and large breakup cross sections can't be explained using a $(0p_{1/2})^2$ configuration for the ^{11}Li ground state [Th94]. Adding an s $_{1/2}$ component to the ^{11}Li ground state fixes these discrepancies. Consequently, this means that the ^{10}Li system should have both s-wave and p-wave resonances close to threshold.

The experimental difficulties in studying ^{10}Li are well documented. Currently, there are 10 published results regarding the low-lying structure of ^{10}Li , and they are sum-

marized in Table 4.1.

Table 4.1: Previous measurements of ^{10}Li states below $-S_n=1.0$ MeV

Year	Ref.	Reaction	$-S_n$ [MeV]	Width[MeV]	assignment
1975	Wi75	$^9\text{Be}(^9\text{Be}, ^8\text{B})^{10}\text{Li}$	0.80(25)	1.2(3)	g.s.
1990	Am90	$^{11}\text{B}(\pi^-, p)^{10}\text{Li}$	0.15(15)	<0.4	s1/2 g.s.
1994	Yo94	$^{11}\text{B}(^7\text{Li}, ^8\text{B})^{10}\text{Li}$	<0.10 0.54(6)	<0.23 0.36(2)	s1/2 g.s. p1/2
1993	Kr93	^{18}O fragmentation	<0.15 OR ~2.5		s1/2, gs s1/2, excited state
1995	Zi95	^{11}Li breakup	$a = 0 - (-50)$ fm		s1/2, g.s.
1997	Bo97	$^9\text{Be}(^{13}\text{C}, ^{12}\text{N})^{10}\text{Li}$ $^{10}\text{Be}(^{12}\text{C}, ^{12}\text{N})^{10}\text{Li}$	0.53(6) 0.24(6)	0.30(8)	p1/2 p1/2
1997	Zi97	^{11}Li breakup	0.21(5) 0.62(10)	0.12 0.6(1)	
1998	Be98	^{11}Li breakup	$a = -1.75(75)$ 0.30(5)		s1/2 g.s. p1/2
1999	Th99	^{18}O fragmentation (SNDS)	$a < -20$ fm OR ~2.5	<0.030	s1/2, g.s. s1/2, excited state

The first experimental observation was in 1975 by Wilcox *et al.* who used the $^9\text{Be}(^9\text{Be}, ^8\text{B})^{10}\text{Li}$ reaction at 120 MeV to produce ^{10}Li . They used two silicon telescopes at 14° and 30° in the lab to detect the ^8B and recoiling ^{10}Li , respectively. There is one prominent peak in their spectrum at $S_n = -0.80 \pm 0.25$ MeV, which they attribute to the ground state. The energy resolution of this spectrum is not very good, and the peak may be a composite of two or more peaks. In addition, there are only ~30 counts in the observed peak (Figure 4.1).

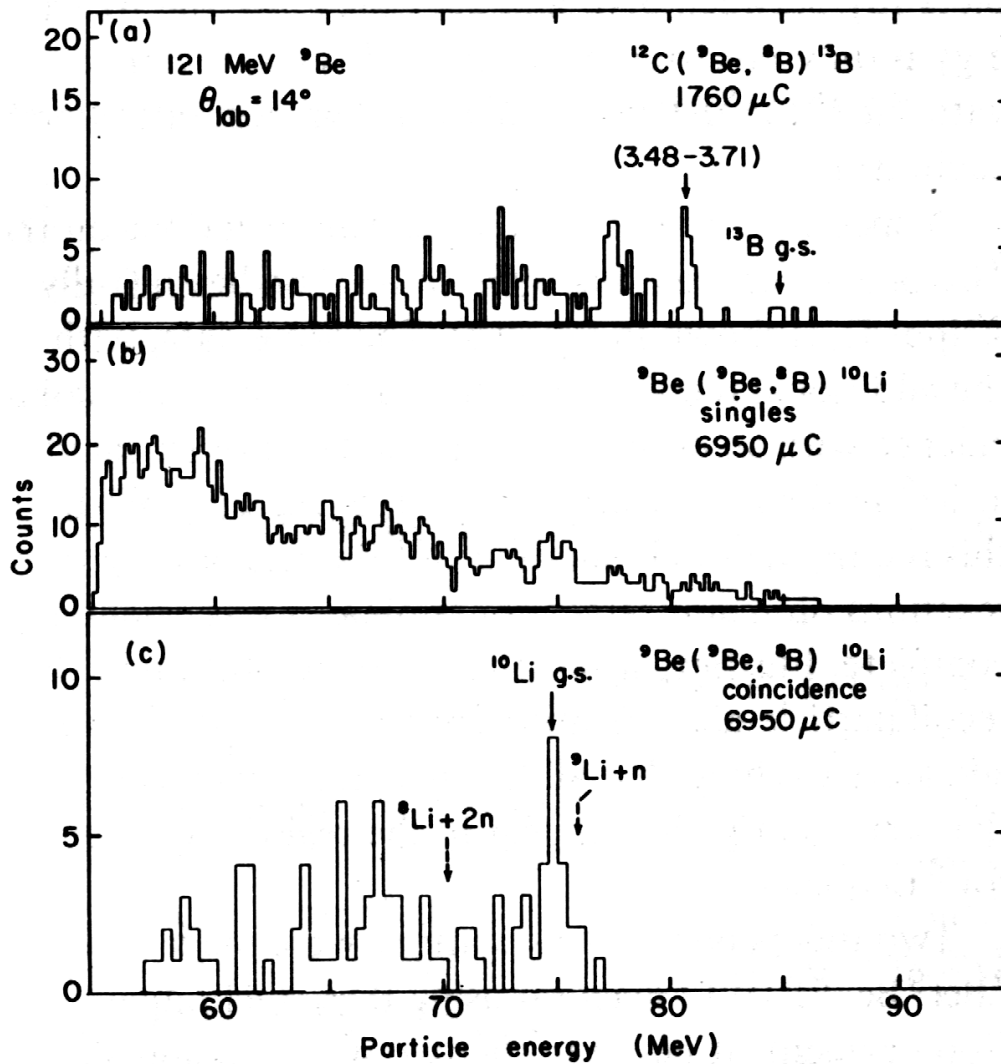


Figure 4.1: The first experimental observation of ^{10}Li [Wi75] using the $^9\text{Be}(^9\text{Be}, ^8\text{B})^{10}\text{Li}$ reaction at 121 MeV. The resolution and statistics are poor in the ^{10}Li energy spectrum (bottom panel).

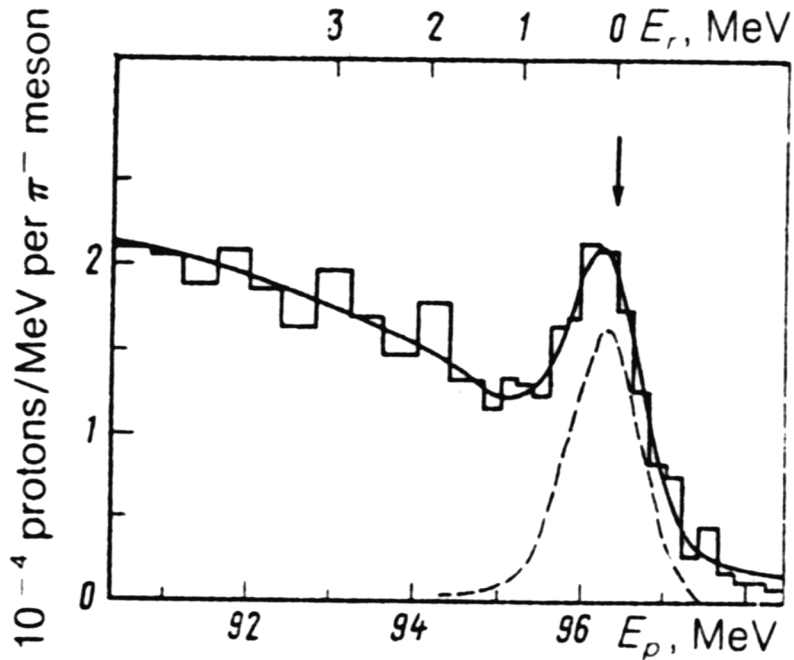


Figure 4.2: The $^{11}\text{B}(\pi^-,p)^{10}\text{Li}$ reaction [Am90]. It is difficult to tell whether the peak is a single state or a composite.

Amelin *et al.* published the next experimental observation of ^{10}Li in 1990. They used a (π^-,p) reaction on a ^{11}B target to produce ^{10}Li . Their spectrum shows a rise near zero separation energy, and has a peak at $-S_n = 150 \pm 150$ keV. They speculate this is an s-state and that it is the ground state. Again, the resolution is too poor to determine whether the peak is a composite structure or one peak (Figure 4.2). The observation of a 240 keV p-wave state that will be discussed shortly makes it possible this state contributes to the observed peak.

In 1993, Kryger *et al.* performed an experiment using Sequential Decay Neutron Spectroscopy (SNDS)[Kr93]. The nucleus of interest is generated in a fragmentation reaction and then decays in flight into a charged fragment and a neutron. The energy of both are measured, and thus the velocity of the neutron relative to the charged fragment is

deduced. The center of mass energy difference is then extracted. Kryger *et al.* used fragmentation of ^{18}O to produce ^{10}Li , and ^7He . The observed relative velocity of the ^6He -n system agrees well with the known ground state in ^7He at $E_r = 440 \pm 30$ keV. They see a peak at zero relative velocity in the ^9Li -n system which they attribute to an s-wave ground state OR a state coupled to the first excited state of ^9Li at 2.7 MeV (the absolute uncertainty is due to the relative nature of the measurement). There are shoulders on the spectrum which can be fit with a p-wave state near 500 keV.

Young *et al.* [Yo94] performed another binary reaction spectroscopic measurement of the ^{10}Li nucleus. The reaction they chose was $^{11}\text{B}(^7\text{Li}, ^8\text{B})^{10}\text{Li}$ at $E(^7\text{Li})=131$ MeV. They observe a sharp rise near zero separation energy in the ^{10}Li energy spectrum, and see one prominent peak at ~ 500 keV. Their fitting procedure can fit either one p-wave state at 500 keV or an s-wave state at <100 keV, and a p-wave state at 540 keV. The statistics for this experiment are low and they describe the evidence for the s-wave state as “weak”.

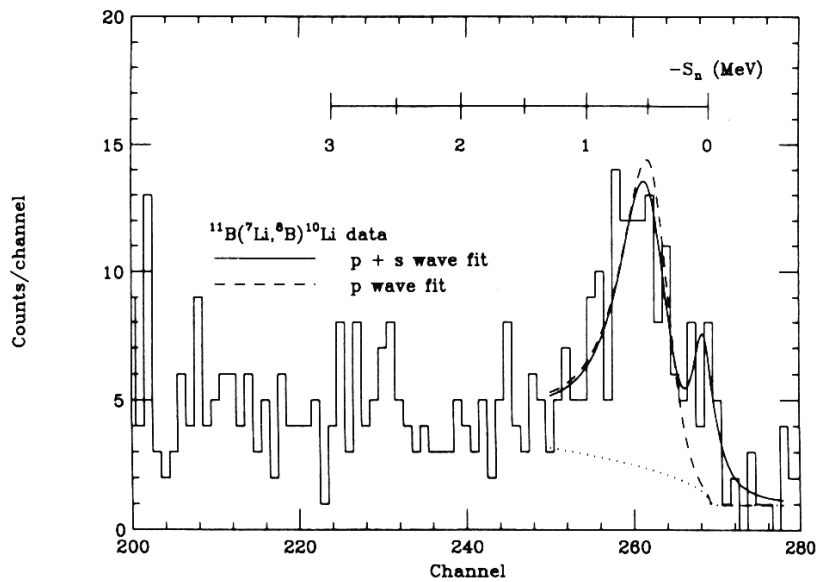


Figure 4.3: Results from the Young, *et al.* experiment [Yo94]. A prominent peak is observed at $-S_n=540$ keV.

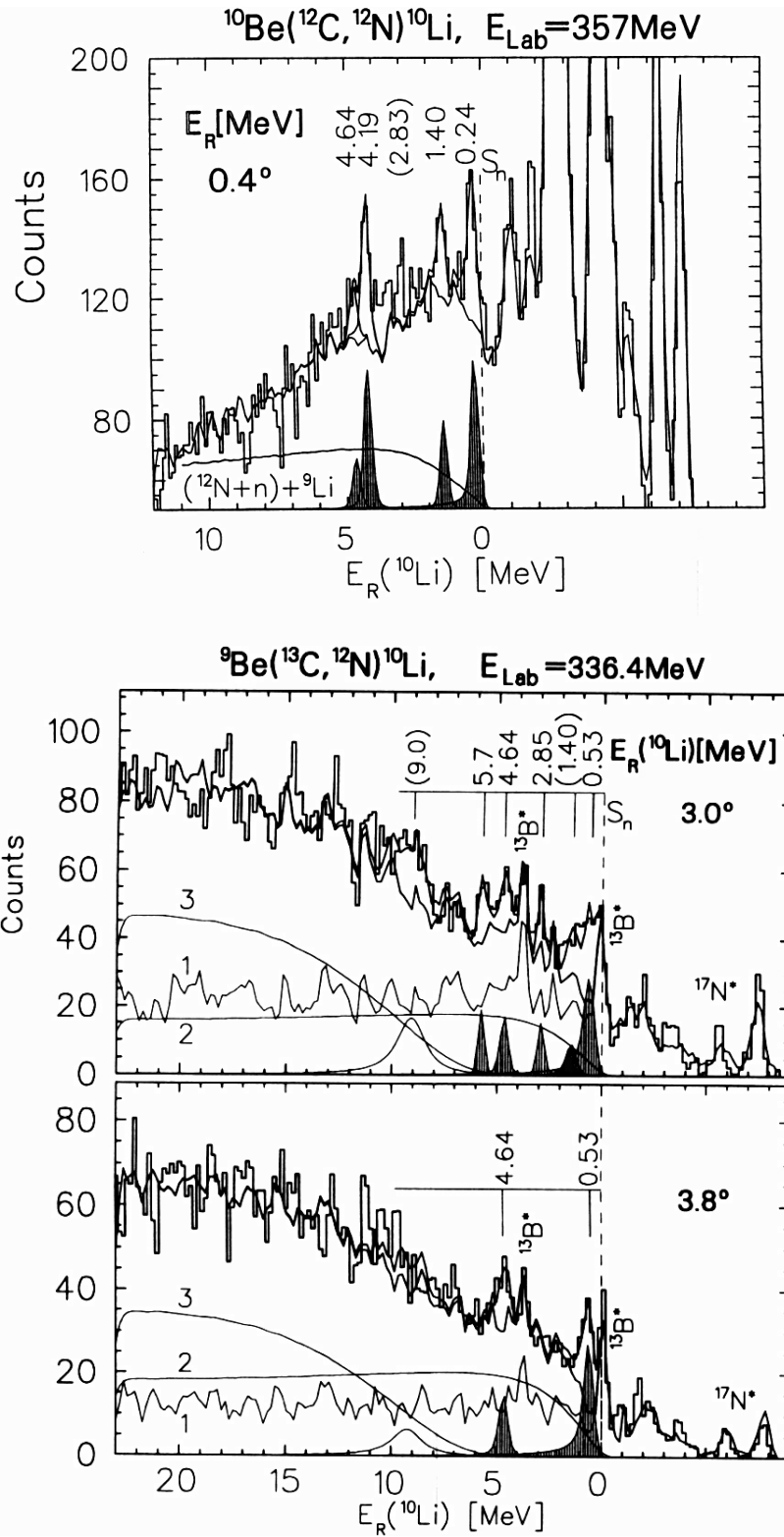


Figure 4.4: Two measurements by the Bohlen group [Bo97]. The measurements show evidence for states at $-S_n = 240$ and 530 keV.

A group at the Hahn-Meitner Institute in Berlin have made many spectroscopic measurements using binary transfer reactions. They have performed several measurements of the ^{10}Li nucleus, first published in 1993 [Bo93], then again in 1997 [Bo97]. In the 1997 paper they re-analyzed the data from the 1993 paper with an asymmetric, Breit-Wigner line shape. The $^9\text{Be}(^{13}\text{C}, ^{12}\text{N})^{10}\text{Li}$ and the $^{10}\text{Be}(^{12}\text{C}, ^{12}\text{N})^{10}\text{Li}$ reactions were used to populate states in ^{10}Li . Two prominent peaks at $-S_n = 240 \pm 60$ and $-S_n = 530 \pm 60$ keV are identified as two p-wave states, the 1^+ and 2^+ , but with no specific assignment. In all their experiments the spectra have significant background contamination, and the statistics are generally low. Extracting the location of the states then becomes very dependent on the background subtraction (Figure 4.4).

In 1995 a group from GSI in Germany published results from a ^{11}Li and ^{11}Be breakup experiments [Zi95]. They measured momentum distributions of the neutrons following breakup to ascertain the population of states in ^{10}Li . They see evidence for a s-wave ground state close to threshold with a scattering length in the range of -5 to -50 fm.

In 1997 Zinser *et al.* measured energy distributions of the neutrons and ^9Li fragments following breakup of ^{11}Li [Zi97]. The spectrum was fit with an s-wave shape at 200 keV and a p-wave shape at 600 keV, not accounting for experimental resolution effects. Bertsch *et al.* re-analyzed this experiment with a three-body approach to the ^{11}Li system and included experimental resolution in the fitting procedure [Be98]. They see an s-wave state with a relatively high scattering length ($a \sim -2$ fm) peaking at 80 keV, and a p-wave at 300 ± 50 keV.

Recently, Thoennessen *et al.* [Th99] published a new SNDS experiment which is essentially a repeated Kryger *et al.* experiment but with better resolution. Their findings

are consistent with a s-wave state at <50 keV (again either the ground state or coupled to the first excited state of ${}^9\text{Li}$) and a shoulder which may be attributed to a p-wave state at 540 keV. A p-wave state at ~ 250 keV can not be ruled out from their fit [Th99].

These experimental results taken together start to paint a picture of ${}^{10}\text{Li}$ which has a very low lying s-wave ground state (1^- or 2^-) and two p-wave states separated by 300 keV at ~ 250 and ~ 550 keV. However, it is very desirable to finally perform one clean, high-statistics, absolute mass measurement of the states involved. This is the goal of the experimental work described in this chapter.

4.2 Experimental setup

4.2.1 Reaction and targets

The ${}^9\text{Be}({}^9\text{Be}, {}^8\text{B}){}^{10}\text{Li}$ reaction was chosen because it has been reported [Wi75] to have an relatively large cross-section ($\sigma_{\text{cm}}=30$ nb/sr) for this type of process. In addition, the ${}^8\text{B}$ ejectile has a much different rigidity than other competing reactions which provides a relatively contaminant-free focal plane. A 40 MeV/u ${}^9\text{Be}$ beam was used to bombard three targets: 0.94 mg/cm² beryllium, 1.1 mg/cm² carbon, and a 0.45 mg/cm² beryllium foil on a formvar backing.

The binary reaction ${}^9\text{Be}({}^9\text{Be}, {}^8\text{B}){}^{10}\text{Li}$ was used to populate states in ${}^{10}\text{Li}$. The exact mechanism for particle transfer (sequential single particle transfers or as groups) is uncertain. Because it is a binary reaction (only two products), the kinematics are completely determined, meaning a ${}^8\text{B}$ with a certain energy and scattering angle defines exactly the parameters of the residual ${}^{10}\text{Li}$ nucleus.

4.2.2 S800

The S800 was operated in the dispersion-matched, energy-loss mode (see chapter

2). The primary beam was focussed at the object position of the spectrograph, then transported to the target position of the spectrograph. There it reacted with the targets and the reaction products were swept to the focal plane. The spectrograph was set with the center of the aperture at 5° corresponding to an angular coverage of 3.5-8 degrees in the laboratory.

4.2.3 Detectors

The focal plane detectors consisted of two position detectors and a plastic scintillator. The position detectors measured the two transverse positions and angles of the particles as well as their energy loss. A 5cm thick plastic scintillator was located behind these detectors for total energy measurement.

All ions from reactions in the target stopped in the scintillator. The scintillator is a 5 cm thick piece of plastic designed to scintillate when particles strike it. Light guides are mounted on each end to enhance the collection of the light in the photomultiplier tubes. The light travels through the plastic and light guides and is collected in the photomultiplier tubes on either end of the scintillator. The light collection time is of the order of nanoseconds from the scintillator. The amount of light collected in the scintillator is a function of the ion's atomic number, mass, and total energy. It can be parameterized as given in a Nuclear Instruments and Methods article published by Bechetti [Be76].

The position detectors are cathode readout drift chambers (CRDCs). The CRDCs were filled to a pressure of 140 Torr with 80% CF_4 and 20% C_4H_{10} . Figure 4.5 shows a schematic of their operation. Ions traveling through the gas create an ionization. A constant vertical electric field in the detector move the electrons toward an anode wire, where charge amplification takes place in the high electric field close to the wire. The anode wire

is placed below a grounded Frisch grid and held at a constant voltage, typically 1400 Volts. The electrons are collected on the anode wire. Cathode pads are located in front of and behind the anode wire. The charge collected on the anode wire induces a positive charge on the cathode pads, and each individual pad is read. A Gaussian fit to the charge distribution is performed, and the centroid is used as the x (dispersive) position in the detector. The signals from the cathode pads are amplified by small circuit boards placed directly on the detectors.

The vertical (y) position is determined by measuring the drift time of the electrons to the anode wire. The typical drift time of the electrons to the anode wire are 0-20 μ s, depending on their vertical position. The fast response of the scintillator is advantageous for timing the electron drift to the anode wire in the CRDCs. Measuring the time between the scintillator signal and the anode wire signal provides a direct vertical position measurement of the particle track with a 0.3 mm resolution.

The total charge collected on the cathode pads depends on the nuclear species and its energy loss in the detector gas, and can be used as a $\Delta E \sim z^2$ measurement for particle identification. Charge resolution was barely sufficient to separate particle groups and would have benefited from energy loss measurements in an ion chamber.

The particle's flight time is also measured relative to the cyclotron radiofrequency pulses. Reactions in the target make fragments with different speeds, and hence different flight times to the focal plane. This flight time measurement can be used in conjunction with the total energy measurement (given by the scintillators) and energy loss (given by the CRDCs) to identify nuclear species that arrive at the focal plane.

4.2.4 Electronics

Figure 4.6 is a schematic of the electronics used in this experiment. The plastic scintillator behind the focal plane generates the master gate for the electronics. The signal from each PMT on the scintillator is amplified and send to a constant fraction discriminator module (CFD) to provide a logic pulse. A master gate is generated by requiring coincidence of the two PMT logic pulses on the scintillator. The master gate is used to open a 20 μ s gate to wait for an anode signal (the wait gate). The master gate is logically AND-ed with the (NOT Busy) signal from the data acquisition front end CPU to provide the “master gate live” signal. This is also the start for the drift time in the CRDCs and the stop for the flight time information, taken relative to the RF pulses for the cyclotron. The anode wire signal is used as the stop for the drift time in the CRDCs. The TAC output (0-10V for 0-20 microseconds) was input to a 12-bit ADC. Each pad (there are 224 in each CRDC) is read by its own fast encoding and reading ADC (FERA) (charge integrators), following amplification by the front end electronics (FEE) cards. A 500 μ s gate for the FERA read is opened by the AND of the wait gate and the anode pulse. The pedestals on the FERAs were set so that a channel with no data has a digital output of zero. When the FERA module is operated in zero suppression mode, all channels that equal zero are ignored, ensuring that only those channels with significant signal heights are read. This reduces the deadtime substantially. Reading each FERA channel every event takes $5\mu\text{s}/\text{channel} * 224\text{channel}/\text{detector} * 2\text{detectors} = 2240$ microseconds, limiting the data rate to ≤ 450 events/second; this limit is increased to $\sim 20,000$ events/second in zero suppressed mode.

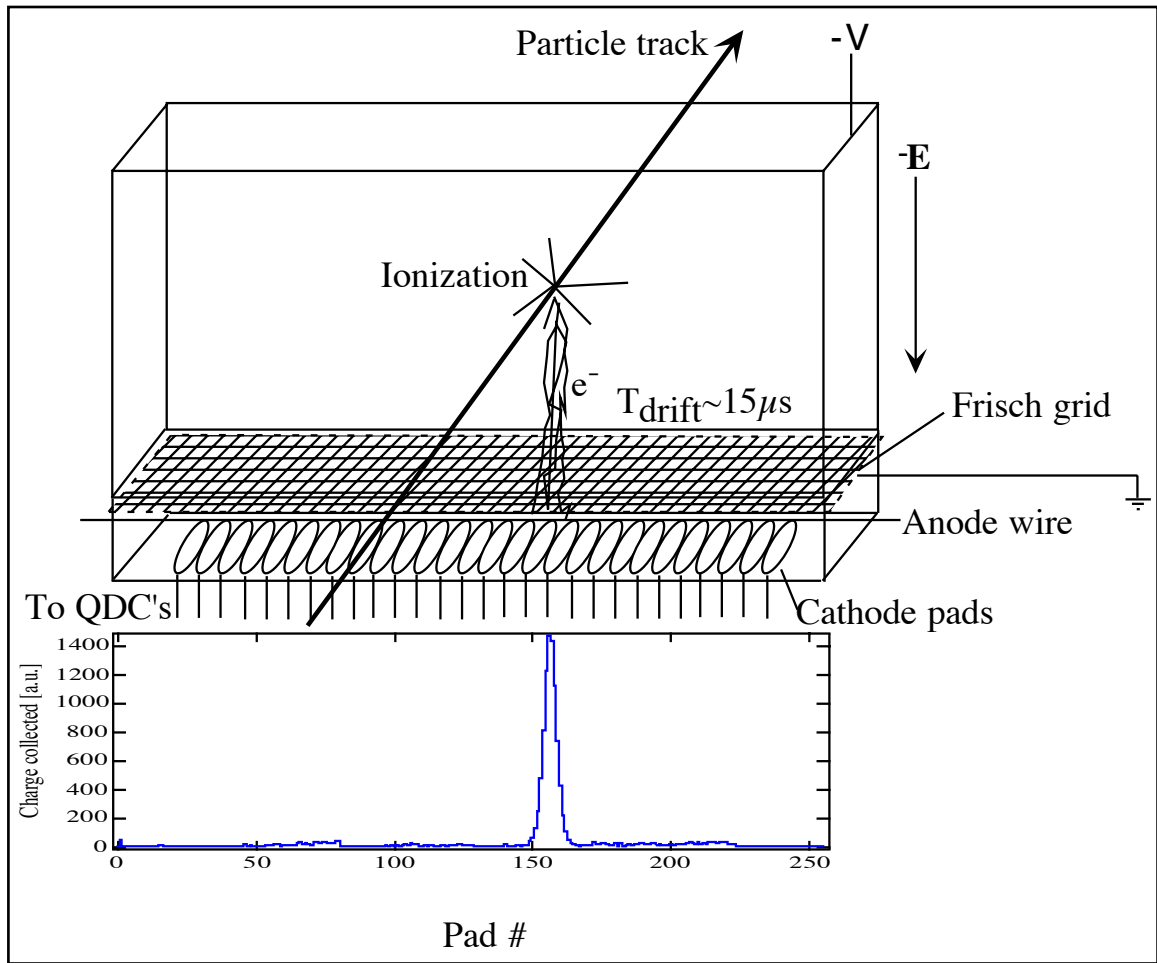


Figure 4.5: Schematic of the CRDC operation. A particle track ionizes the gas as it passes through the detector. The electrons drift to the anode wire where they are collected. An induced image charge on the cathode pads provides horizontal position information, while drift time of the electrons to the anode wire provide vertical position information. (Note the cathode pad locations are really on the front and back of the detector; they are shown schematically on the bottom here for clarity.)

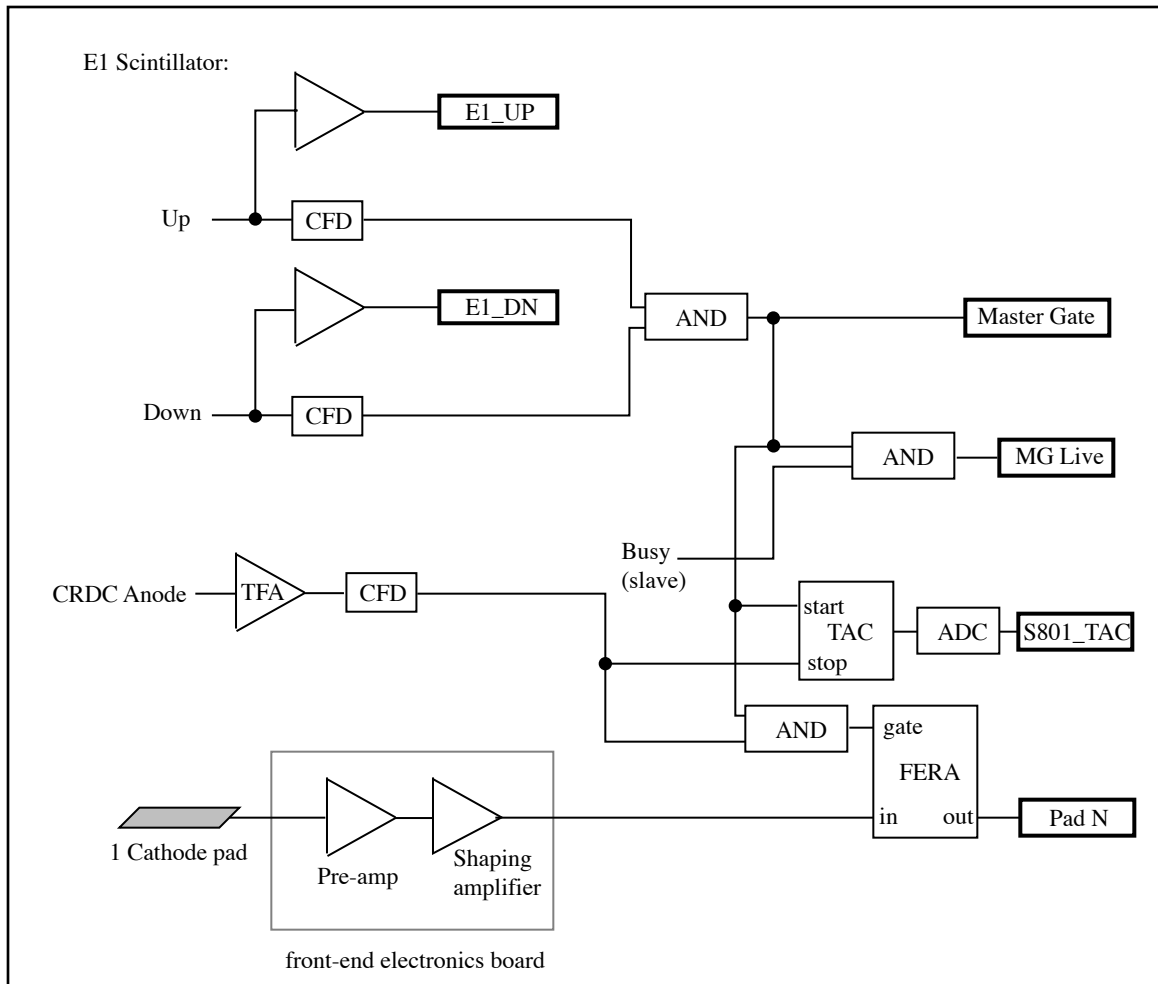


Figure 4.6: Schematic of S800 focal plane detector electronics. Only one CRDC is shown and only one cathode pad is shown from the overall electronics to simplify the diagram.

4.2.5 Calibrations

4.2.5.1 Tracking detector position calibrations

The ray reconstruction depends on the measured positions and angles of the fragments in the focal plane. Masks with well-defined hole and slit patterns were placed in front of (upstream) the CRDCs and illuminated with beam particles to calibrate the detector positions. The dispersive direction is already calibrated in the sense that the cathode pads are known to be separated by 2.54mm and fixed in position. A beam-axis hole (previously optically aligned with the beam axis) provides the optical center of the detectors. Other holes at several known locations from the beam axis hole provide the vertical position calibration points. Figure 4.7 is a picture of the calibrated position spectra of the S801 mask.

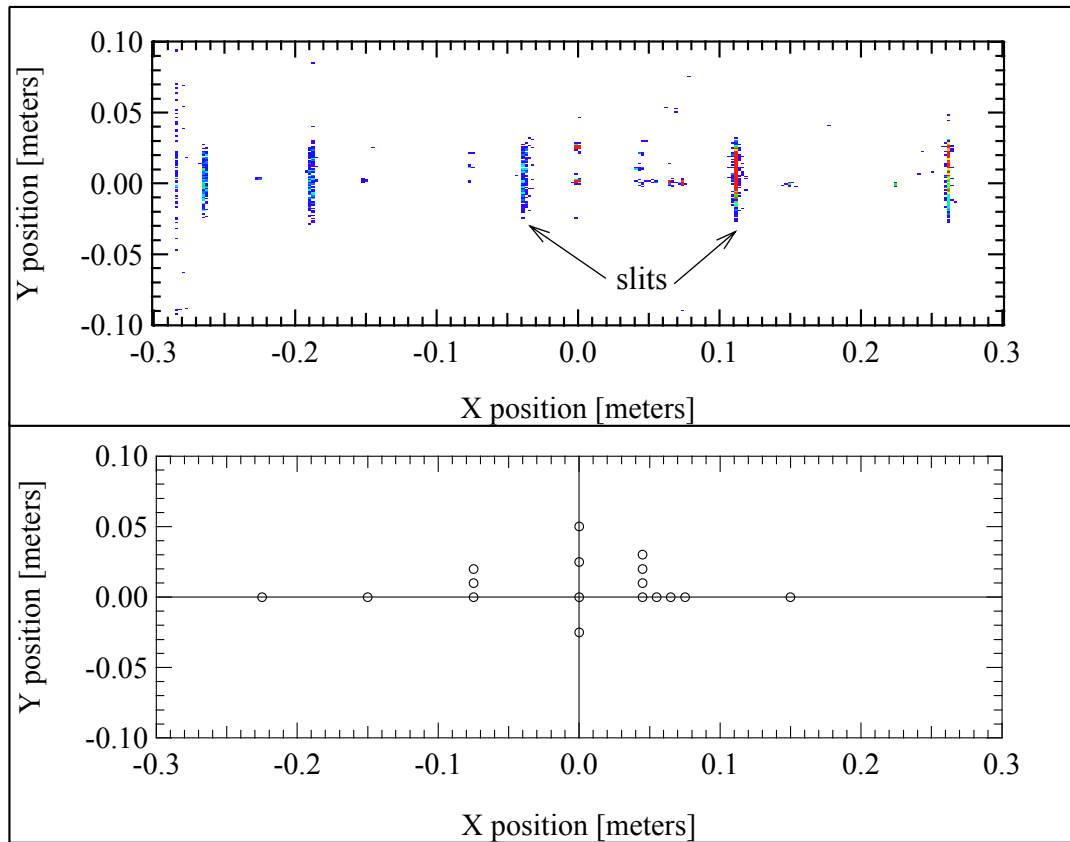


Figure 4.7: Data taken with the position mask placed in front of the S801 CRDC. The top panel is the raw data taken with a small cut in the dispersive angle, θ , and the bottom panel is a picture of the prominently illuminated holes.

Throughout the experiment the measured drift times of the electrons to the anode wire changed in a systematic way, causing the y position calibration to drift. Eventually they reached an asymptotic value at the end of the experiment. This phenomenon was caused by the gas mixture changing in the CRDCs. Drift times decreased, and the collected charge increased over time, suggesting that gas contaminants were being purged. Thus, the drift time distributions (S801 and S802 TAC parameters) shrunk throughout the experiment (Figure 4.8).

The drift behavior can be measured. The masks can be repeatedly inserted for position calibrations throughout the experiment. However, this was not done because the

drift was not discovered until after the experiment had ended.

The width of the TAC distributions only depends on the gain (mm/channel) and the vertical width of the beam if the spectrograph magnets don't change. Thus, the vertical position calibration can be tracked throughout the experiment by measuring the width of the TAC distributions. The center of the distributions will also change and can be adjusted accordingly. The best measure of this, lacking repeated mask measurements, is to use a constant like the spectrograph acceptance. The gains and offsets were modified for each run to keep the spectrograph acceptance constant throughout the experiment. Since the y position in the focal plane strongly depends on ϕ angle, the known reaction kinematics were used to validate this procedure.

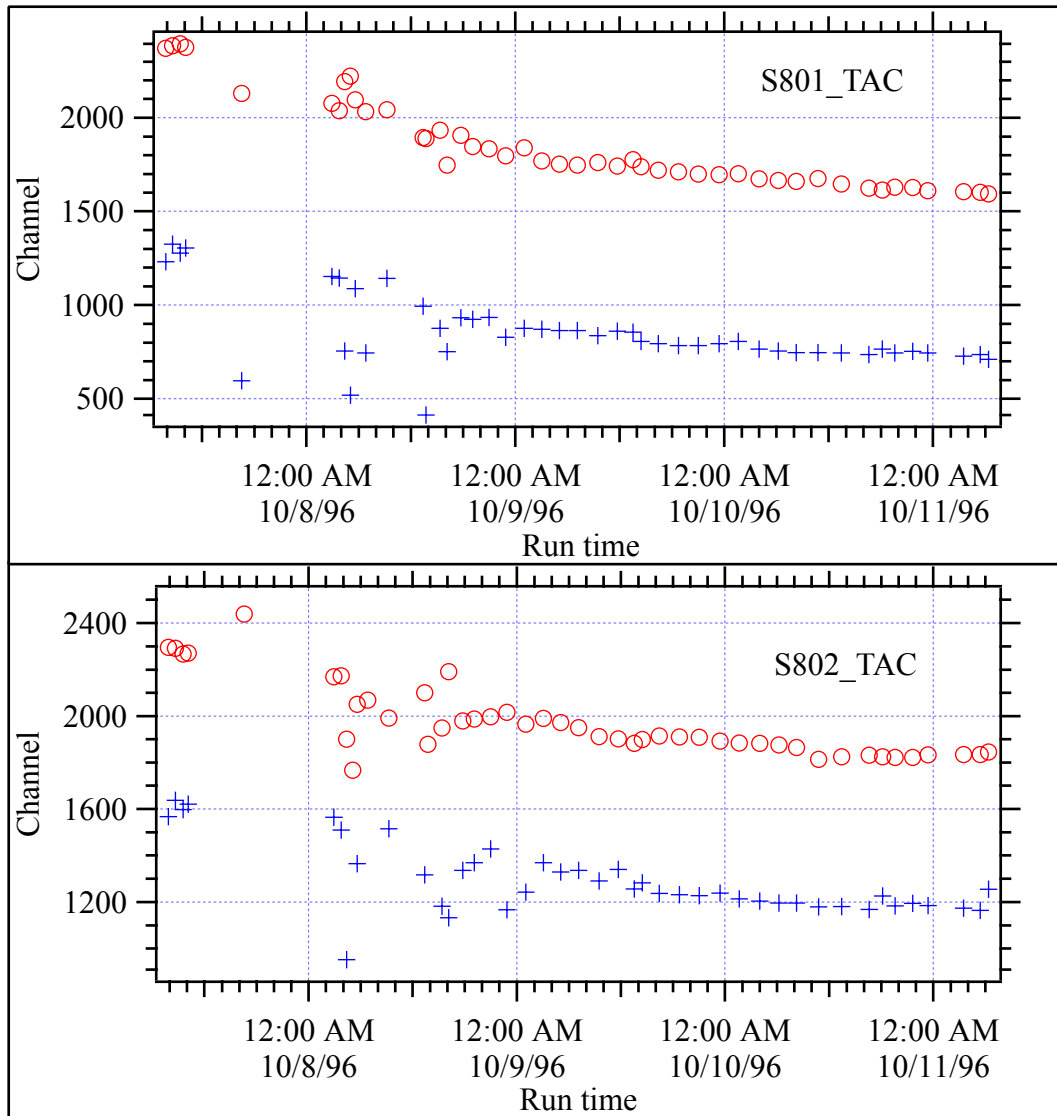


Figure 4.8: Detector y-position (TAC) drifting over time during this experiment. The circles are the centers of the distribution and the (+) are the widths. Error bars are not plotted and fluctuations are due to low statistics.

4.2.5.2 Elastic and inelastic scattering

Scattering the beam off the different targets used in the experiment serves many purposes. Sweeping the elastic peak across the focal plane allows the spectrograph bending radius as a function of focal plane position to be calibrated. (In most cases the scattering populates excited states in the target nucleus through inelastic scattering, which are also useful in the bending radius calibration.) The resolution and operation of the detectors were checked in this fashion. Since ray-reconstruction is used to achieve the ultimate resolution, these strongly populated reactions provide verification of the coefficients used in ray-reconstruction. Target contaminants may be present and knowledge of these is important in deciphering the energy spectra of the reactions. Target contaminants were found by scattering the ^9Be beam off the different targets and measuring the energy as a function of angle. Different target constituents have different reaction kinematics and therefore are very apparent in an energy-angle plot. The different elastic scattering kinematics provided a very accurate method to determine absolute scattering angle.

4.2.5.3 Spectrograph bending radius calibration

Figure 4.9 shows the spectrograph bending radius calibration taken from the elastic scattering of the beam off the carbon target. The data points were taken from runs at four different field settings which swept the peaks across the focal plane.

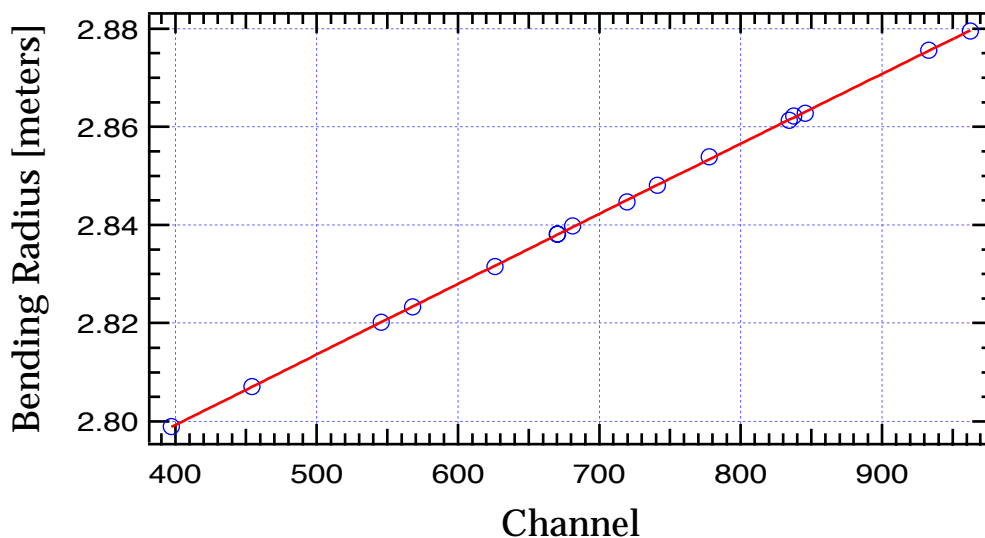


Figure 4.9: Spectrograph bending radius calibration using elastically scattered ${}^9\text{Be}$ for the ${}^{10}\text{Li}$ experiment.

4.2.5.4 Scattering angle calibration

The kinematics of the ${}^9\text{Be}$ beam scattering off ${}^{12}\text{C}$ and ${}^1\text{H}$ are dramatically different. Aligning the kinematics with the spectrum measures any angular offset present in the data (beam angle, spectrograph angle, etc.). Figure 4.10 shows such a plot for the beam scattering off the carbon target. The procedure strongly populated states in carbon (0.0, 4.4, 7.6, 9.6) as well as the ground state in hydrogen, and states at 0.0, ~ 6 and ~ 7 MeV in ${}^{16}\text{O}$. A scattering angle offset of $0.25 \pm 0.03^\circ$ was necessary to align the calculations with the data.

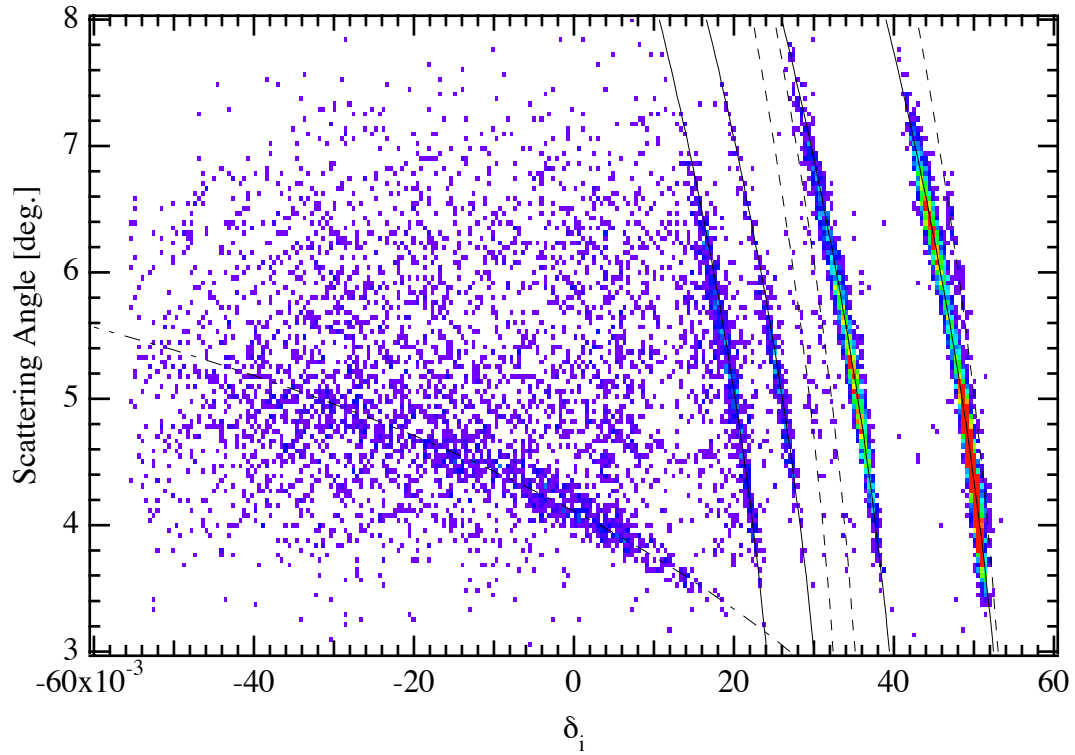


Figure 4.10: Elastic scattering of ^9Be beam at 40 MeV/u from a carbon target consisting of carbon with H_2O contamination. The solid lines are known kinematics for scattering off carbon nuclei populating states, from right to left, g.s., 4.44, 7.65, and 9.64 MeV. The dashed lines are scattering from ^{16}O and populating g.s., 6.1, and 7.1 MeV. The dot-dashed line is elastic scattering off ^1H nuclei. Aligning the known kinematics with the spectrum provides a very accurate scattering angle calibration.

4.2.5.5 Ray reconstruction

As described in Chapter 2, the spectrograph has significant aberrations which must be known and removed. This was the purpose of the mapping effort described in Chapter 3. The fields of Q1, Q2, D1, and D2 were modeled as fringe fields with flat central regions. This flat-field model is valid for the low magnetic fields used in this experiment, but may not be valid for higher field settings at which radial gradients and azimuthal curvature of the spectrograph dipole fields become substantial.

The fringe fields were determined by interpolating the fields from the field maps onto the central trajectory, then fitting the field profile with a 5th order (6 term) Enge function. The effective field boundaries were chosen by matching the integral on either side of the field boundary:

$$\int_{-\infty}^{s_0} B ds = \int_{s_0}^{\infty} (1 - B) ds \quad (4. 1)$$

where s_0 is the field boundary location. Appendix B lists the coefficients used in the reconstruction process.

The useful reconstruction variables are δ (the fractional kinetic energy) and θ and ϕ , the two angles. The reaction scattering angle was constructed as follows:

$$\Theta = \text{atan}(\sqrt{(\tan\theta)^2 + (\tan(\phi + \phi_s))^2}) + \Theta_0 \quad (4. 2)$$

where Θ is the reaction scattering angle, θ and ϕ are the reconstructed angles emerging from the target, ϕ_s is the angle position of the spectrograph, and Θ_0 is the measured angular offset described in section 4.2.7.2.

The energy of the ion observed in the spectrograph is a function of the Q-value of the reaction and the kinematic energy shifts. The ejectiles lose more energy as they are

scattered to larger angles. This energy dependence can be calculated exactly. These known kinematic affects can be used to combine all events with the same reaction Q-value by adding the amount of energy necessary to shift that event to a single angle (usually 0 degrees), as follows:

$$E(\Theta_0) = E(\Theta) + a_2(\Theta - \Theta_0)^2 + a_4(\Theta - \Theta_0)^4 \quad (4.3)$$

where a_2 and a_4 are determined from relativistic kinematics, $E(\Theta)$ is the measured energy at the measured angle Θ , and $E(\Theta_0)$ is the energy at Θ_0 . This parameterization is used because of the ease and speed of the calculation. The kinematic energy shifts were calculated for $\Theta_0 = 0.0$ degrees.

4.3 Results

Nuclear species were identified using the energy loss, total energy, and time-of-flight measurements described earlier. Particle identification in the spectrograph focal plane starts by assuming all ions reach the detectors with the same average rigidity. The particle's total energy and speed is then calculated and used to make simulated particle identification plots. The measured and calculated patterns are compared to identify each group of ions.

Figure 4.11 is a spectrum of energy loss in the CRDCs vs. measured time-of-flight to the first scintillator. The data was filtered to select only the ^{11}C and ^8B groups. Subsequent filtering was performed using total energy measurements from the stopping scintillator. The resulting contamination was $<1\%$ for the ^{13}B spectrum, and 2.5% for the ^{10}Li spectrum. The ^{11}C group is very clearly separated, and the contamination for that group is well below 0.1% . Table 4.2 lists the measured cross sections for all of the reactions.

Table 4.2: Reaction cross sections from the ^{10}Li experiment. The uncertainties on the cross sections are purely statistical. A 10-50% systematic error from the beam current measurement is not included.

Reaction	Target	Area	σ [nb/sr]
^{10}Li (lowest peak)	0.94 mg cm ⁻² Be	305	260±15
^{13}B (g.s.)	1.1 mg cm ⁻² C	44	420±60
^7He (g.s.)	0.94 mg cm ⁻² Be	14534	12300±100
^{10}Be (g.s.)	1.1 mg cm ⁻² C	1379	13120±350

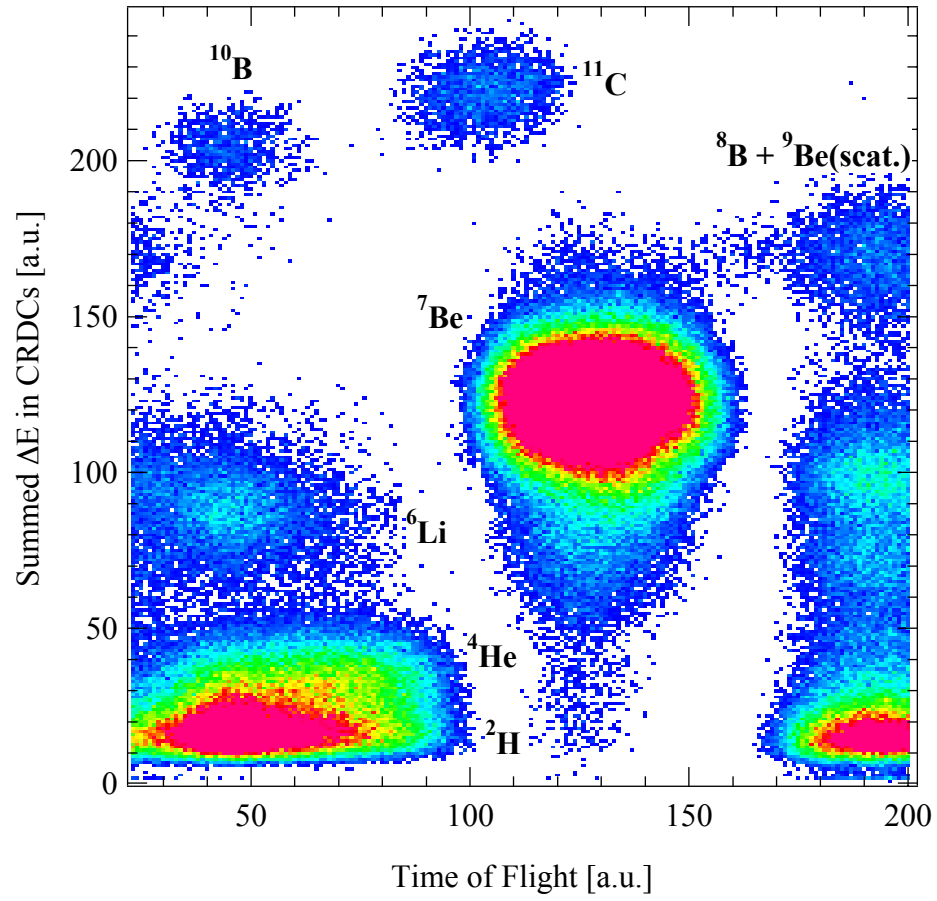


Figure 4.11: Measured energy loss vs. time-of-flight spectra. Contamination in the ^8B gate arises mainly from scattered beam.

4.3.1 ^{10}Be and ^7He energy spectra

The ($^9\text{Be},^{11}\text{C}$) reaction on the carbon and beryllium targets provided additional calibration and verification points by measuring the location of states in the nuclei ^{10}Be and ^7He . The ground state mass of ^{10}Be [Au93] and its first excited state at 3.36803(11)MeV [Aj88] are known to better than 1 keV. These states were included in the energy calibration. Figure 4.12 shows an energy vs. scattering angle plot of the $^{12}\text{C}(^9\text{Be},^{11}\text{C})^{10}\text{Be}$ reaction. It clearly shows that the ground and first excited states of ^{10}Be are populated, as well as states in the ejectile ^{11}C nucleus. Figure 4.13 shows just an energy spectrum of the ^{11}C ejectiles from this reaction, as well as Gaussian fits used to extract the peak locations. There is no problem fitting the isolated ground state peak with a Gaussian shape. The location of the first excited state is more difficult to ascertain due to the complex, non-Gaussian background surrounding it. Nevertheless, the spectrum was fit with a sum of 5 Gaussians, and the position error in first excited peak was increased by the covariance of the peak parameters surrounding it.

The ground state of ^7He is known at $S_n = -440 \pm 30$ keV with a width of $\Gamma = 160 \pm 30$ keV [Au93, Aj88]. Figures 4.14 and 4.15 are the data taken populating the ^7He nucleus. The peak fitting procedure for the ^7He ground state is not straightforward because it is an unbound nucleus and has an asymmetric shape with an energy-dependent width. The line shape is folded with the experimental resolution function and fit to the data. The location and width of the peak is within errors of their expected values. (See section 4.4.3.1 for details about the fitting procedure.) This procedure confirms the beam energy and relative target thicknesses between the carbon and beryllium targets.

The experimental resolution function was determined to be a mixture of Gaussian

and Lorentzian shapes. Figure 4.16 shows the effect of using a pure Gaussian (top) contrasted with using the mixture. The function is a sum with 25% Lorentzian and 75% Gaussian. This mixture improves the fit substantially in the low (<0) energy tail. However, it doesn't appreciably affect the width or location of the peak.

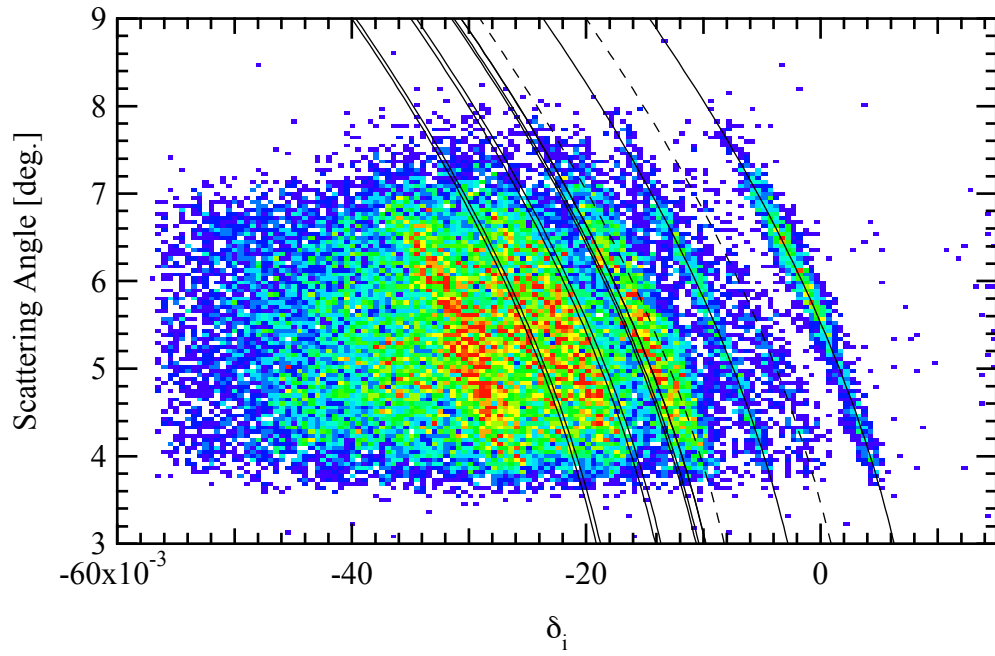


Figure 4.12: Spectrum of ^{11}C ejectiles from $^{12}\text{C}(^9\text{Be}, ^{11}\text{C})^{10}\text{Be}$ reaction populating the ground and excited states in ^{10}Be . The solid lines overlaid on the spectrum are the calculated kinematics for known states in ^{10}Be . The dashed lines are the ^{11}C 2.0 MeV excited state corresponding to the reactions (from right to left) $^{12}\text{C}(^9\text{Be}, ^{11}\text{C}(2.0))^{10}\text{Be}(\text{g.s.})$ and $^{12}\text{C}(^9\text{Be}, ^{11}\text{C}(2.0))^{10}\text{Be}(3.368)$.

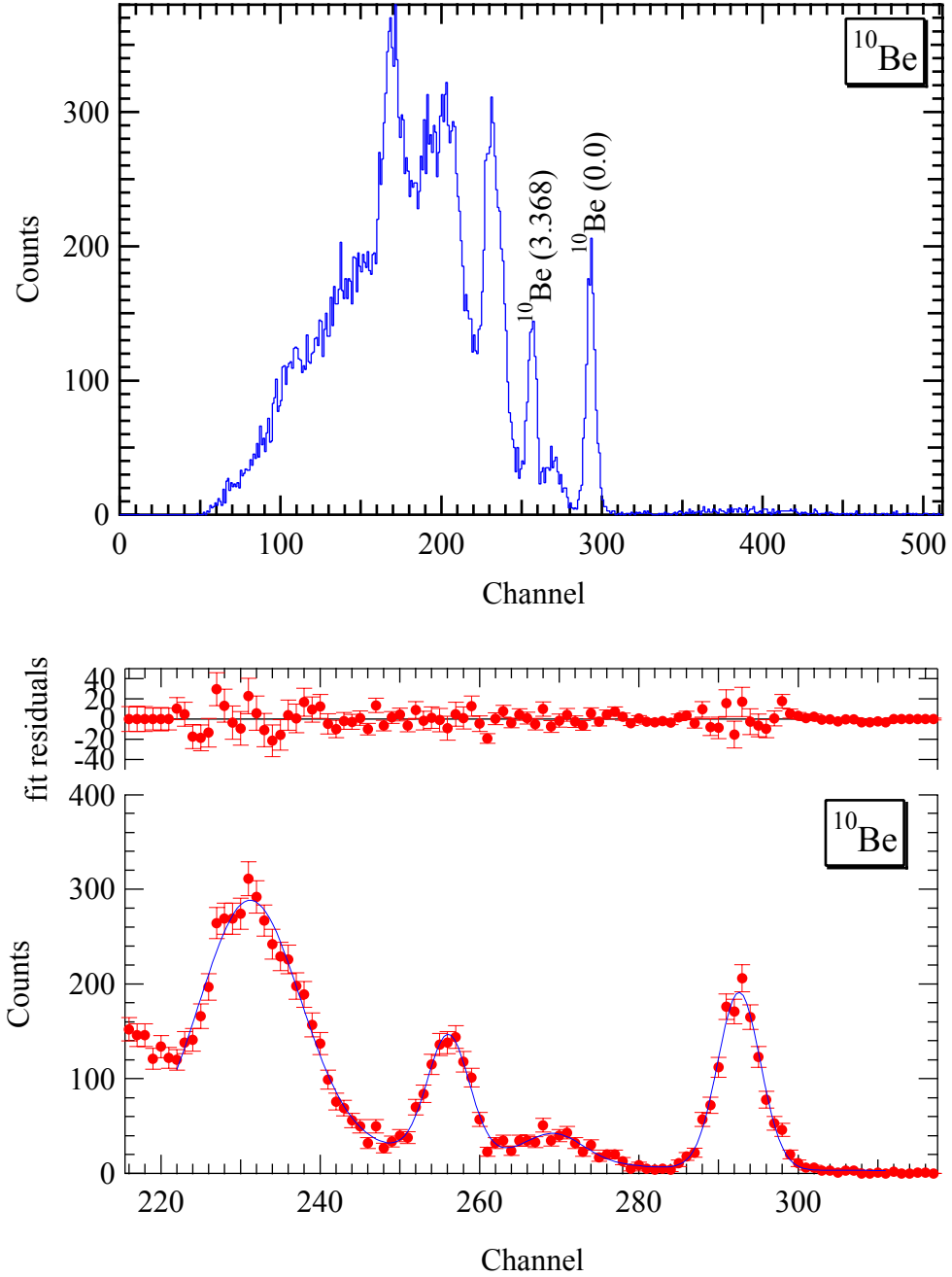


Figure 4.13: Top: Spectrum of ^{11}C ions in the S800 focal plane populating states in ^{10}Be . The top panel shows the entire focal plane extent. Bottom: Five Gaussians were fit to the lower portion of the spectrum to determine the location of the g.s. and 3.368 MeV states in ^{10}Be .

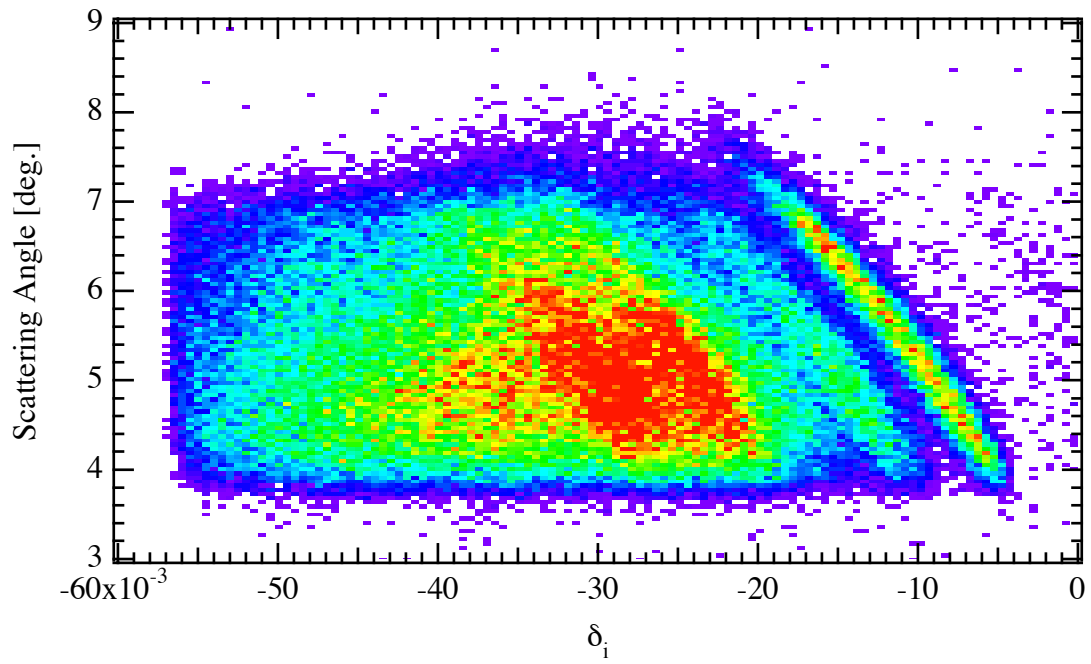


Figure 4.14: Same as figure 4.12, but using the ${}^9\text{Be}({}^9\text{Be}, {}^{11}\text{C})$ reaction to make ${}^7\text{He}$.

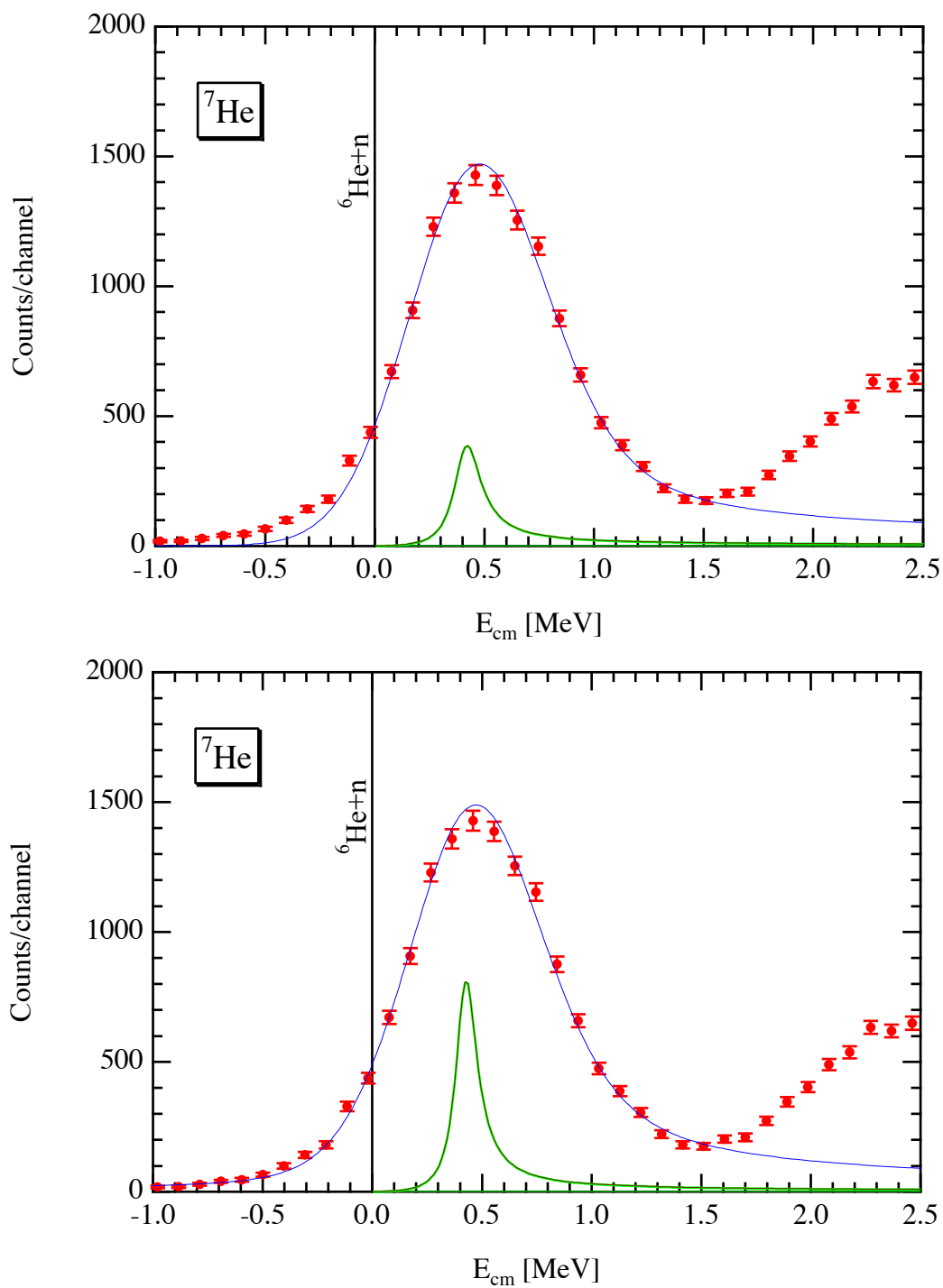


Figure 4.15: Fits to the ${}^7\text{He}$ ground state using two different resolution functions. The top panel shows a purely Gaussian resolution function, whereas the bottom shows an improved fit (<0 MeV) by including some Lorentzian shape in the resolution function. The mixture doesn't affect the peak location (430 ± 30 keV) of the fit, but has a small effect on the extracted width (120 ± 30 versus 150 ± 30 keV).

4.3.2 ^{13}B energy spectrum

The $^{12}\text{C}(^9\text{Be},^8\text{B})^{13}\text{B}$ reaction provided a quality ^8B energy calibration. The reaction populates numerous states in the ^{13}B nucleus ranging from the 0-10 MeV. The higher lying states provide the most useful energy calibration because they are closest to the ^{10}Li Q-value. Figure 4.12 shows a ^{13}B energy spectrum. The top portion of the figure shows all the peaks. The bottom panel shows Gaussian fits to the spectrum of the known states in ^{13}B . The ground state is the only clearly separated peak. Because of the substantial background above 7 MeV in the spectrum, peaks above 7 MeV were excluded from the energy calibration.

The resolution for this peak is $E/\Delta E=1300$, limited by the intrinsic angular spread in the beam. The target thickness broadening has an effect, but is $E/\Delta E\sim 3000$. The much larger effect is the kinematic broadening due to the beam emittance. The primary beam typically has an emittance 5-10 π mm-mrad in both the dispersive and non-dispersive directions, usually a little better in the dispersive direction [St98]. These angles smear out the kinematics of the reaction substantially, especially at larger angles.

Directly measuring these divergences by transmitting the beam to the focal plane is the preferred method of determining the intrinsic angular divergence. This option was unavailable in the present experiment. Instead, the beam divergence was estimated through simulation. The prescription is to first assume that the resolution is entirely dominated by kinematic and target thickness broadening, a valid assumption for energy resolutions of ~ 1 in 10^3 . The angular distribution for an isolated state is measured and entered into the simulation. The θ and ϕ acceptances are measured and the target thickness contributions are known. These are entered into the simulation, leaving only the incoming

angular spread, $(\Delta\theta, \Delta\phi)$, as free parameters. Finally, these angular widths are adjusted until the resolution matches that of the measured peak. The resulting full angular widths were 4.4 milliradians in each direction.

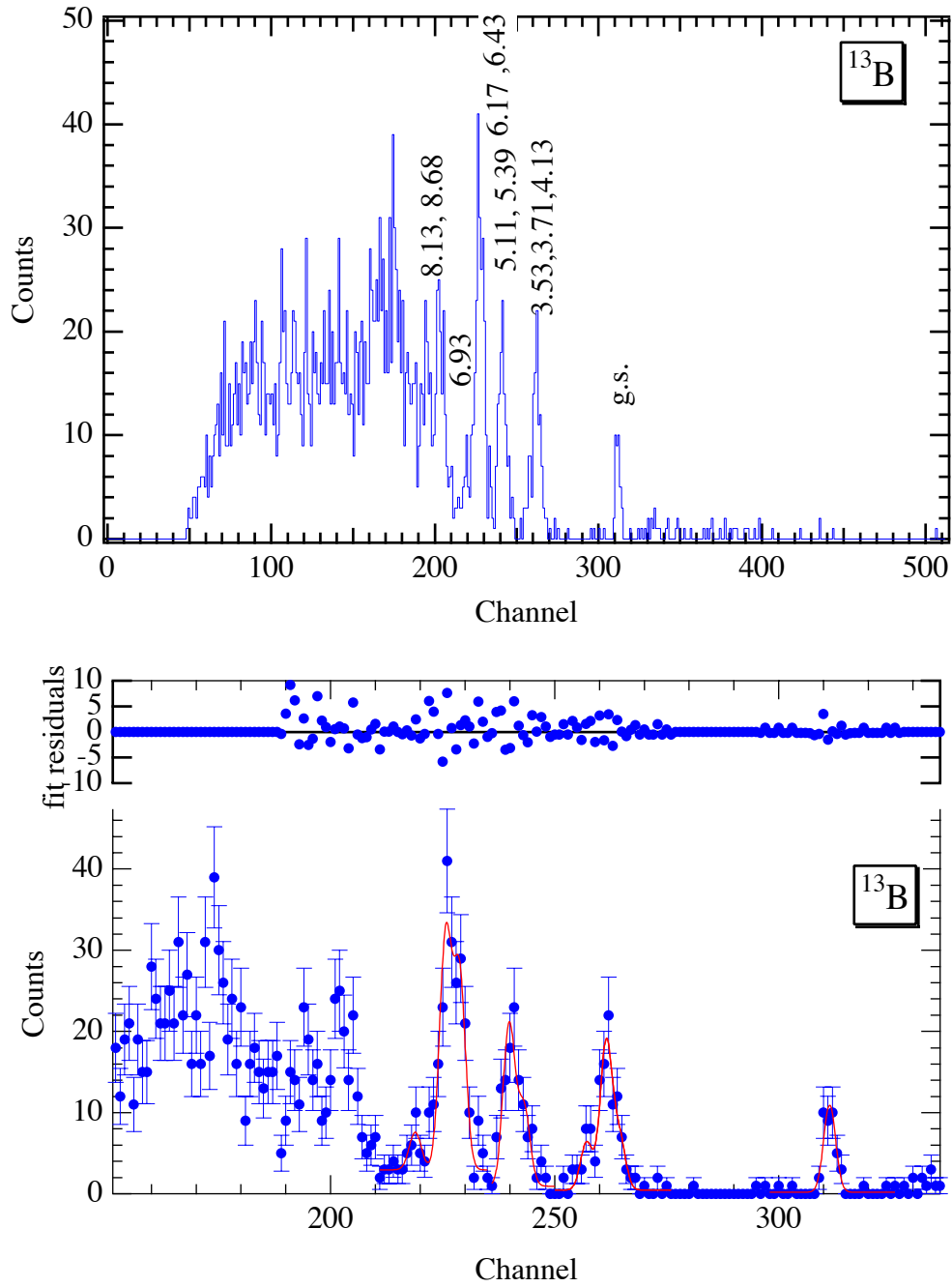


Figure 4.16: Top: Energy spectrum of ^8B ions in the focal plane populating states in the ^{13}B nucleus. Bottom: Multiple Gaussian fits used for energy calibration of the focal plane.

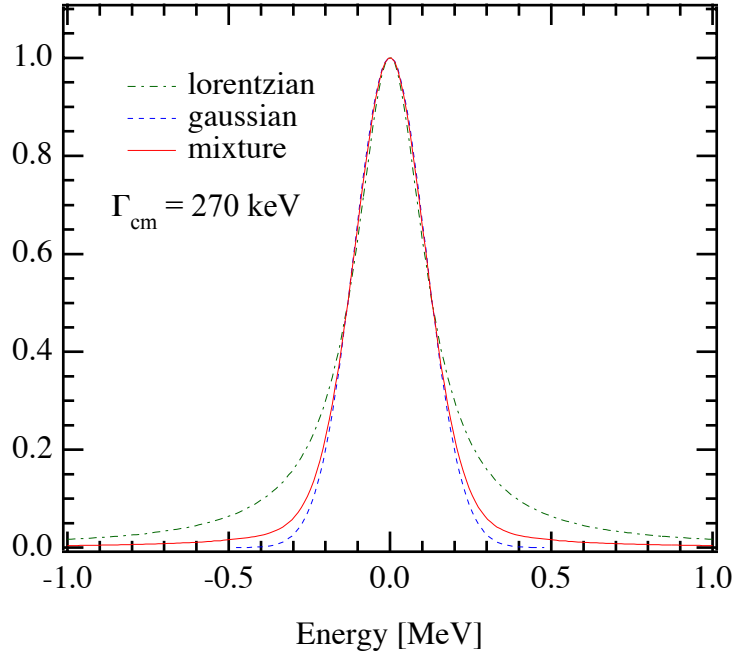


Figure 4.17: Resolution function used for the (${}^9\text{Be}, {}^8\text{B}$) reaction (solid line). All three peaks have the same FWHM.

Adjusting the resolution width for different target thickness and kinematic broadening effects one arrives at the total resolution width of 300 keV for the ${}^8\text{B}$ energy spectrum from the ${}^{10}\text{Li}$ reaction, which is 270 keV in the ${}^{10}\text{Li}$ c.m. system.

4.3.3 ${}^{10}\text{Li}$ energy spectrum

Figure 4.19 shows an energy spectrum for the ${}^8\text{B}$ ejectiles following the ${}^{12}\text{C}({}^9\text{Be}, {}^8\text{B}){}^{13}\text{B}$ and ${}^9\text{Be}({}^9\text{Be}, {}^8\text{B}){}^{10}\text{Li}$ reactions. The ${}^8\text{B}$ ions were selected, and kinematic energy shifts were applied event by event to shift the energy to what it would be at 0° . This moves all events with the same Q-value into one peak. The ${}^{10}\text{Li}$ spectrum exhibits the sharp rise at threshold characteristic of unbound nuclei and similar to that observed for the ${}^7\text{He}$ spectrum shown earlier.

A pre-existing NSCL computer program called RELMASS was used to calibrate

the energy within the ^{10}Li system. The program is described in detail Brian Young's thesis [Yo93]. The program accepts spectrograph magnetic field settings, calibration reactions, target thickness, beam energy, and scattering angles as input. For energy calibration, it takes a known state in a nucleus and deduces a bending radius. RELMASS then fits a polynomial to the bending radius as a function of focal plane position for a series of measured field vs. position measurements with a particle of known momentum.

For mass measurements, the process is inverted; the program uses a focal plane position to deduce bending radius and then the energy of the state in the nucleus. The calibration data and subsequent fit are shown in Figure 4.19.

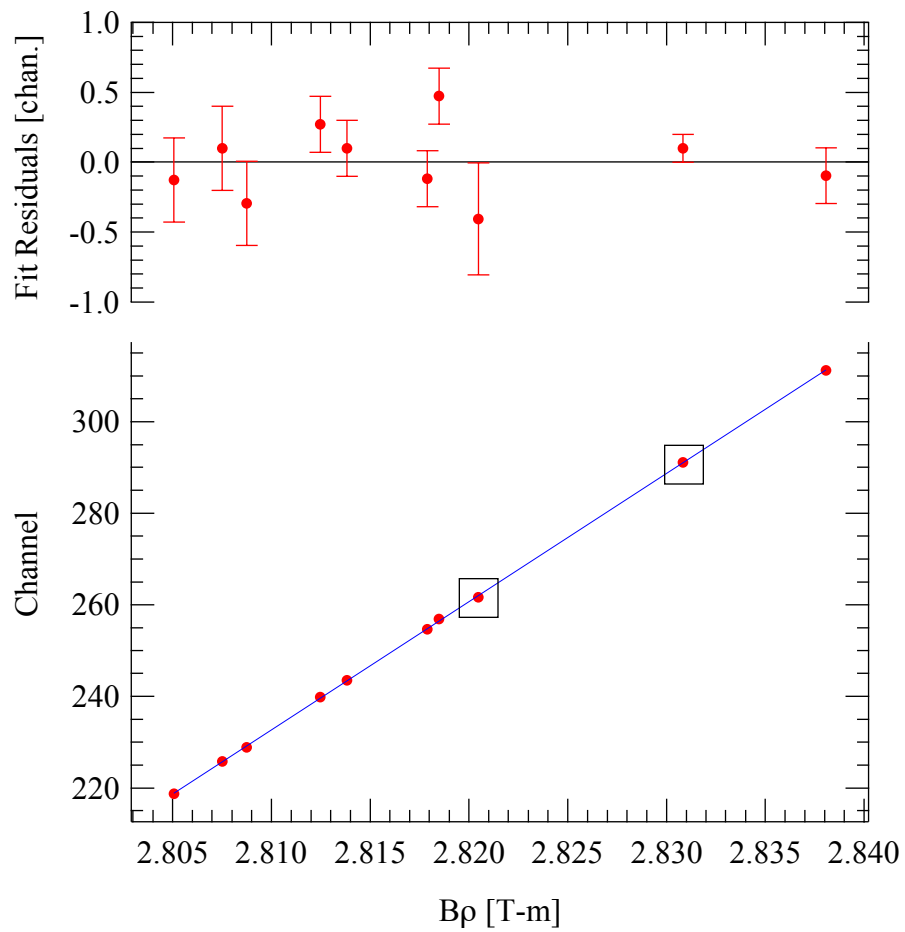


Figure 4.18: Rigidity calibration for this experiment. The line through the data is a linear fit. The points surrounded by squares are calibration points from the $^{12}\text{C}(^9\text{Be},^{11}\text{C})^{10}\text{Be}$ reaction; all others are from the $^{12}\text{C}(^9\text{Be},^8\text{B})^{13}\text{B}$ reaction.

4.3.3.1 Fitting procedure

The expected line shapes for an unbound nucleus are asymmetric resonance shapes with an energy dependent width because the separation energy changes dramatically over the width of the state. The line shape for a complicated transfer reaction is nearly impossible to deduce exactly, so resonances are usually calculated using one-nucleon scattering. For example, Young [Yo94] made calculations of neutrons scattering off ${}^9\text{Li}$ to deduce the approximate line shapes for s-wave and p-wave scattering. Several parameterizations have been established [Yo94, Be98], but there is no clear favorite. In particular, there may be reason to expect that the s-wave line shapes depend strongly on the initial states [Th99]. An R-matrix parameterization is a good approximation [Mc94] for the p-waves and fits the calculated p-wave line-shapes of Young very well. The form is as follows:

$$\sigma(E) = A \frac{\Gamma(E)}{(E - E_r)^2 + \frac{\Gamma^2}{4}} \quad (4.4)$$

where $\Gamma(E) \sim E^{l+1/2}$, so the cross section exhibits the well-known $E^{3/2}$ behavior at threshold. The s-wave shapes were determined by fitting a modified Breit-Wigner distribution to the calculations of Young [Yo94]. The width is much more energy dependent than the p-waves. The parameterization was adjusted to reproduce the energy dependence of the width that Young calculated [Yo94].

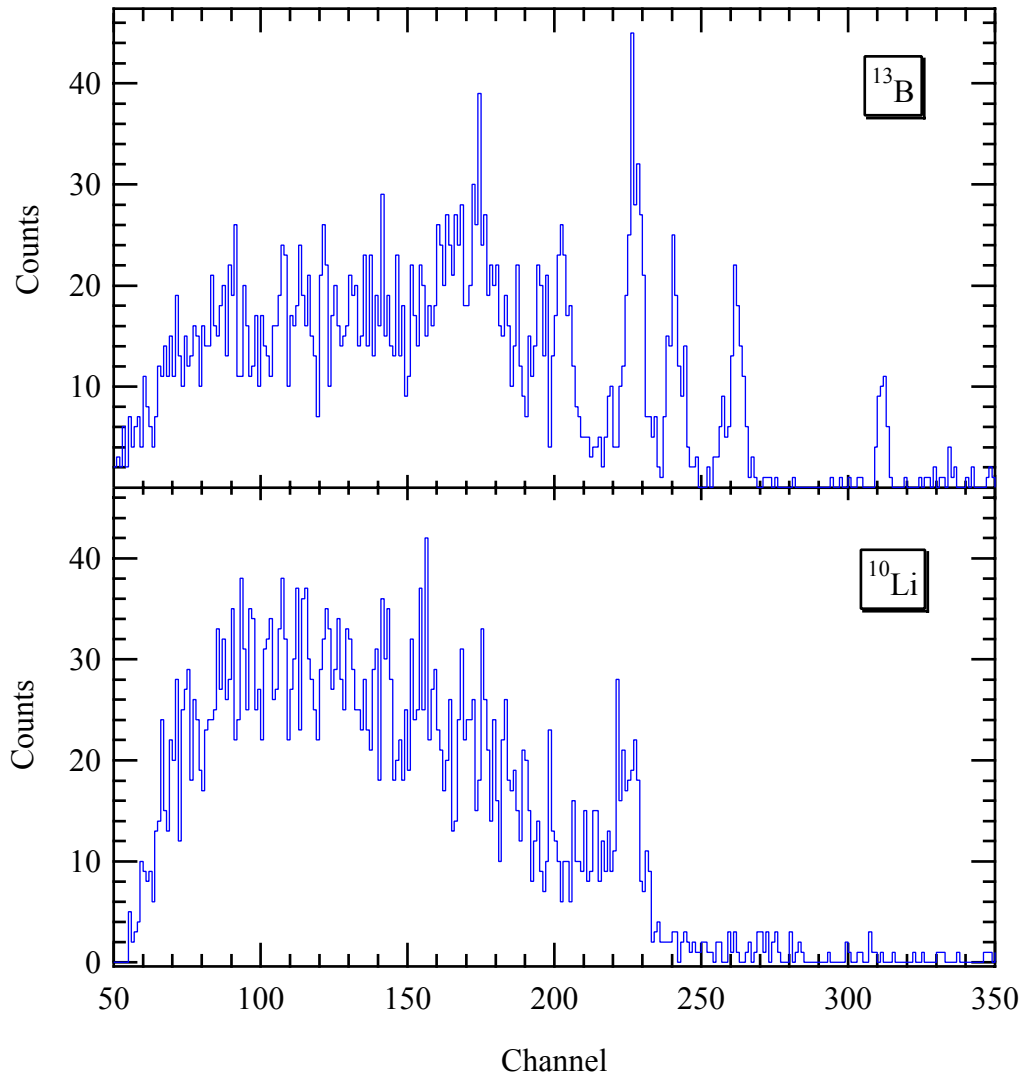


Figure 4.19: Energy spectrum of ^8B ions from both the reactions $^{12}\text{C}(^9\text{Be},^8\text{B})^{13}\text{B}$ (top) and $^9\text{Be}(^9\text{Be},^8\text{B})^{10}\text{Li}$ (bottom), shown for comparison.

The statistics of the spectrum are low and hence a maximum likelihood fitting procedure is appropriate. The fitting procedure is used to maximize the likelihood that the data set describes a Poisson distribution. The likelihood function is defined as follows:

$$L = \prod_{i=1}^N P(y_i, a_i) \quad (4.5)$$

where $P(y_i, a_i)$ is the probability of observing y_i , and a_i is a vector filled with the fit

parameters. Minimizing the negative logarithm of L is the same as maximizing L but more useful for fitting routines which try to minimize a figure of merit. The distribution is assumed to be Poisson in nature, and hence this equates to minimizing the function

$$-\ln(L) = \sum_{i=1}^N y_i \ln(f(x_i, a_i)) - f(x_i, a_i) - \ln(y!) \quad (4.6)$$

where y_i is the measurement at point x_i and $f(x_i, a_i)$ is the fit evaluated at point x_i with parameters a_i .

The fitting model consisted of a background and line-shape contributions. The background shape was a constant plus a three-body contribution which arises from making ${}^9\text{Li}+n+{}^8\text{B}$ in the final state [B156]. The form is a $E^{1/2}$ shape at threshold leveling off to a constant at roughly 3 MeV. The data were fit with this background plus one p-wave, two p-waves, or one s-wave and one p-wave shapes.

The background shape and size have a very small affect on the locations of the peaks, but a dramatic affect on the widths. Therefore, the background size was adjusted by fitting one p-wave peak to the data such that the size of the fit region didn't affect the peak locations or widths. The resulting background shape was then held constant for all of the fits.

Figure 4.20 shows all the fits to the ${}^{10}\text{Li}$ energy spectrum. A single p-wave fits the data with a peak at 500(60) keV, and a width of 420(60) keV. When using a combined fit, the spectrum can be fit with one p-wave at 525(60) keV and either an s-wave right at threshold (<30 keV) or an additional p-wave at 100 keV. Table 4.3 summarizes the fit

parameters.

Table 4.3: Fitted parameters for ^{10}Li energy spectrum.

States included in the fit	E_{peak} [keV]	Γ_{cm} [keV]
one p-wave	500 ± 60	400 ± 60
two p-waves	$100\pm 60, 525\pm 60$	$50\pm 60, 345\pm 60$
one s-wave, one p-wave	$<50, 515\pm 60$	$<100, 350\pm 60$

Uncertainties of the parameters were calculated by summing all contributions in quadrature. There are systematic contributions to the absolute energy scale from target thickness (30 keV), beam energy (10 keV) and scattering angle (10 keV). The uncertainty of the width and shape of the resolution function each contributes 10 keV. These uncertainties contribute 40 keV systematic error to the peak positions. The relative energy scale (keV/channel) is much less sensitive to the target thickness and beam energy contributions. This reduces the systematic uncertainty of the width substantially, from 40 to 10 keV. Statistical uncertainties on the fit parameters contain contributions from the individual parameter variance and the covariance between other parameters. These depend on each parameter and range from 10-60 keV. The statistical uncertainty of one parameter was determined by adjusting it until the fit test parameter changed by unity. These were added in quadrature with the systematic uncertainties to arrive at the uncertainties in Table 4.3.

All fits are of very similar quality, making interpretation difficult. There is clearly a peak at ~ 500 keV, no question. The region near threshold needs more serious consideration. The structure peaking at ~ 100 keV could be either an s-wave right at threshold or a p-wave at ~ 100 keV. Past experiments and three-body calculations taken together [Ko88, Ta85, Kr93, Yo94, Th94, Th99] would favor an s-wave interpretation for this low lying

structure. However, this claim can't be made from the present data alone. In fact, when considering the degrees of freedom, the single p-wave fit is the best with a $L_v=0.95$. Nevertheless, the other fits are equally valid given the low statistics in the energy spectrum.

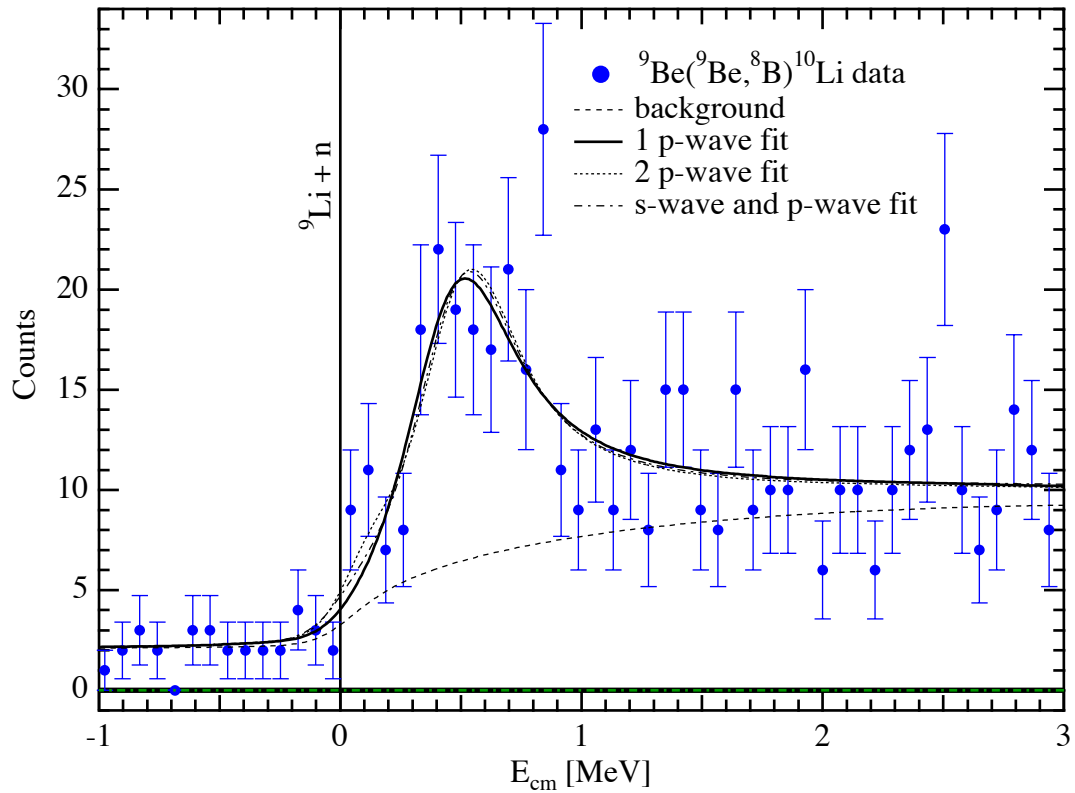


Figure 4.20: The ^{10}Li energy spectrum gathered in this experiment. The three different fits are of similar quality, but the single p-wave fits the data best because it has the fewest degrees of freedom. The background values were held constant for all three fits.

4.4 Discussion

The first measurement of this reaction reported one state at 800(250) keV [Wi75]. It is conceivable that the fitting procedure used in that experiment was a symmetric function and hence would move the peak toward higher energy. Nevertheless, 800 keV value reported there was not corroborated by this measurement.

This particular transfer reaction did not populate 240 keV state reported by Bohlen *et al.* [Bo97] and Bertsch *et al.* [Be98]. The Bohlen group used a charge exchange reaction to populate the states (see Table 4.1), and it is possible that the reactions have different selectivity. It is also possible that the state was misidentified due to the plethora of other peaks surrounding the supposed peak. Another measurement of this reaction with higher resolution and fewer target contaminants would be desirable.

The analysis of Bertsch *et al.* [Be98] favors an s-wave state peaking at 0-100 keV and a p-wave state at 250-350 keV. The resolution in that experiment is insufficient to resolve the two states but the best fit is obtained by including both.

Comparison of data from the present experiment with that of Young's is quite remarkable. Both spectra exhibit the same relative size and shape between 0 and 3 MeV, seen in Figure 4.21. The low-lying rise at threshold is present as well as the large, broad peak at ~500 keV in both spectra.

This measurement also agrees with the 530 ± 60 keV measurement by Bohlen *et al.* [Bo97]. This measurement has the same net nucleon transfer as the present experiment (-p,2n) and perhaps suggests the two reactions should have the same selectivity.

The work of Kryger *et al.* [Kr93] and Thoennessen *et al.* [Th99] indicate a low-lying s-wave state and a p-wave state at 540 keV. While their resolution was insufficient,

it still appears that the 240 keV state wasn't populated in those experiments either.

All these facts lead to a question: Is there really a 240 keV state? Certainly there has to be another p-wave state. It could be very low-lying, or it could be in with broad ~540 keV state seen in other reactions. The only way to clear up this situation is to do more experiments. A coincident inverse kinematics measurement such as ${}^9\text{Li}(d,p){}^{10}\text{Li}$ where both the protons and ${}^9\text{Li}$ fragments are detected might populate all states and should determine spin-parity assignments of the states involved because the (d,p) reaction is well understood. This experiment has been performed with the S800 spectrograph and results should be available shortly [Ko].

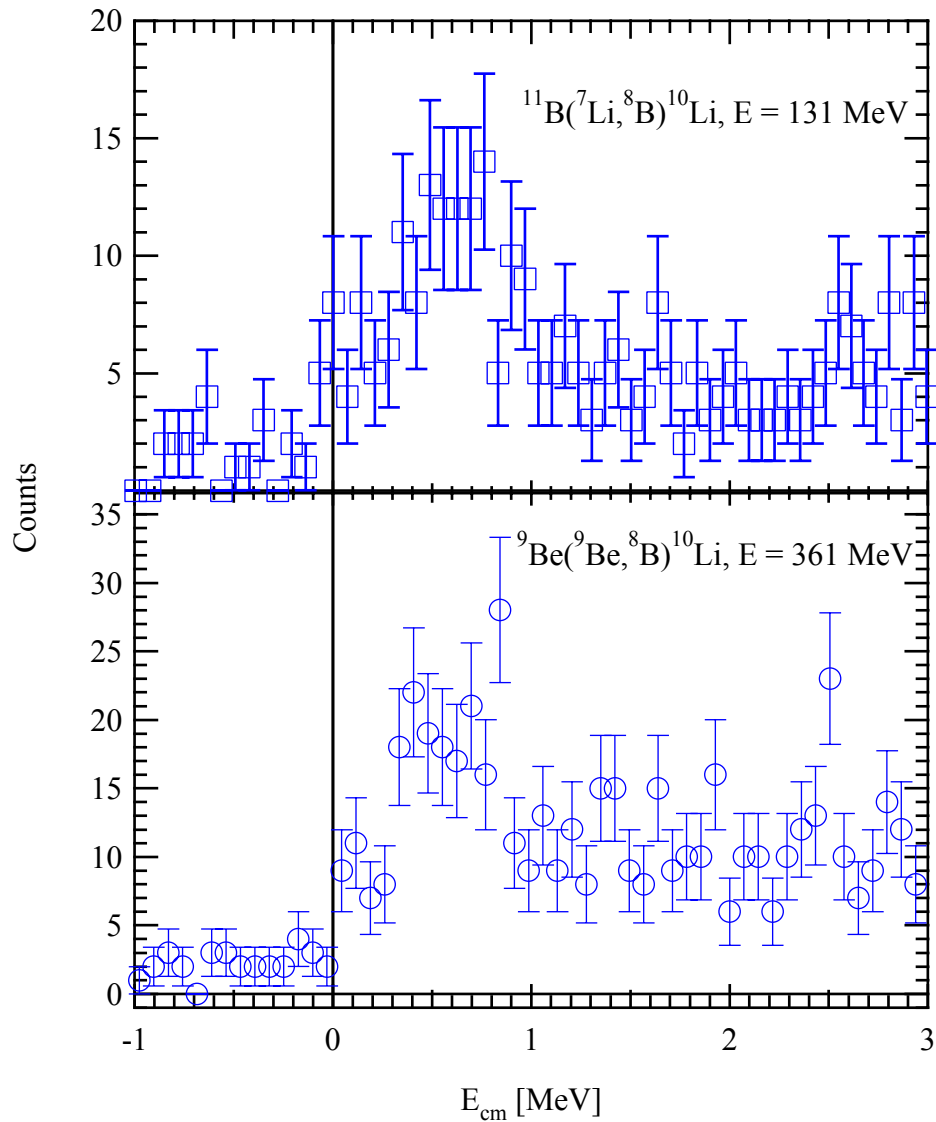


Figure 4.21: Two different reactions measuring the ^{10}Li energy spectrum. The similarities between the two are striking.

4.5 Conclusions

In summary, another binary reaction measurement of the ^{10}Li system was made. One p-wave state was observed at 500 ± 60 keV, with a width of 400 ± 60 keV corroborating several previously reported results. A small excess of counts right at threshold could be interpreted as a p-wave at 100 ± 60 keV or an s-wave state at < 50 keV, but the evidence for

such states is weak at best. Since there are no definitive final measurements available for the ^{10}Li system, each additional measurement contributes valuable knowledge to the overall picture. Future experiments will be performed with the goal of continuing this clarification process.

Chapter 5

Spectroscopy of ^{27}P and ^{23}Al

5.1 Motivation

5.1.1 Explosive hydrogen burning and the rp process

Explosive hydrogen burning is a phenomenon that occurs in extremely hot and dense stellar environments such as occur during X-ray and novae bursts, and Type II supernovae. The extreme temperatures ($10^8 - 10^9$ K) and densities ($10^4 - 10^8$ g cm $^{-3}$) in such environments are necessary for the protons to overcome the Coulomb barrier and fuse with other light nuclei. X-ray and nova bursts occur in binary systems where a small, massive object like a white dwarf accretes hydrogen from a companion star, like a red giant. A thermonuclear flash occurs once enough material has been accreted onto the white dwarf and some of the surface material is ejected and contributes to galactic element production. The massive companion in an x-ray burster system is usually thought to be a neutron star or black hole so no material escapes the star's gravity, and hence it contributes nothing to galactic elemental production. While the hydrogen burning in a supernovae does not contribute to the energy production or the explosion, observation of the proton rich nuclei produced in the event can shed light into and put constraints on the explosion

processes.

The hot CNO cycle and the rp-process are the two main processes which comprise explosive hydrogen burning. The HCNO cycle is fairly well understood, but the rp-process is not. The rp-process is a series of rapid proton capture reactions and β^+ decays that lead to the production of proton rich nuclei. As the environment gets hotter and denser the rp-process moves toward the proton drip line and advances to higher mass nuclei. The capture rates are often based on limited nuclear data or calculations and therefore are very uncertain. Reactions near the valley of stability often have high Q-values (~ 5 MeV) so statistical (Hauser-Feshbach) calculations can be used to determine energy levels because the level density is high. Reactions on nuclei far away from stability typically have low Q-values, so the reaction rate is dominated either by resonant capture or direct capture to the ground state. Not only is it experimentally difficult to study these nuclei, but Hauser-Feshbach calculations fail due to the low level density. Recently, shell model calculations have been used to predict excited state locations in proton rich nuclei, but experimental verification of the levels is still desired [Ch92].

Gamma ray observations of explosive events can provide insight into the workings of the event and how the ejected material is mixed into the interstellar medium. Understanding gamma-ray observations of these events requires knowledge of the production rate and half-life of these isotopes. Typically the light emitted from the explosive event at any given time after the explosion is dominated by the decay of one or a few nuclear species, such as ^{22}Na , ^{44}Ti or ^{26}Al . Understanding their production and half-life can provide information about the complex workings such as energy generation and nucleosynthesis for the explosive event.

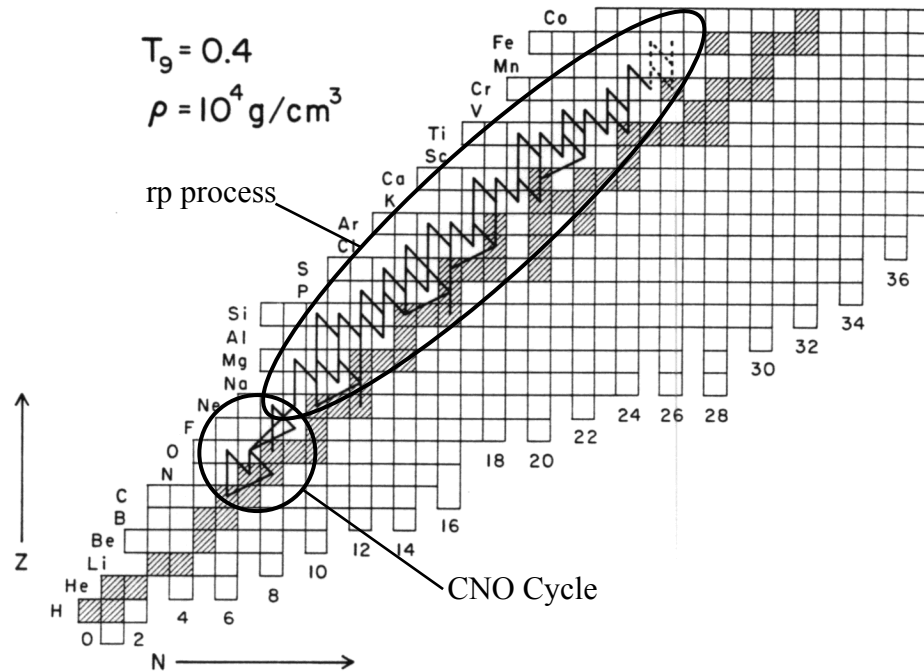


Figure 5.1: The rp-process network for specific temperature and density conditions, reprinted from [Ch92].

This chapter will describe spectroscopic measurements of two nuclei which impact the production of ^{22}Na , ^{26}Al , and other heavier mass elements under certain conditions during an explosive event.

5.1.2 Stellar Reaction Rates

Many (p,γ) reactions in the rp-process proceed through resonant capture and it necessary to know which parameters are important for calculating the capture rates. What follows is a derivation of the resonant capture rate, taken from [Ro88].

The gas in a star is normally nondegenerate, the motion of the nuclei can be described non-relativistically, and the gas is in thermal equilibrium. Hence, the velocity distribution of any nuclear species in a stellar environment is well described by a Max-

well-Boltzmann form:

$$\phi(v) = 4\pi v^2 \left(\frac{m}{2\pi kT} \right)^{3/2} \exp\left(-\frac{mv^2}{2kT}\right) \quad (5.1)$$

where m is the mass of the species and T is the temperature of the gas. The total reaction rate for a reaction whose cross section is $\sigma(v)$ is given by the integral:

$$r = N_x N_y \langle \sigma v \rangle = N_x N_y \int_0^\infty \phi(v) v \sigma(v) dv \quad (5.2)$$

where the product $N_x N_y$ is the number density of pairs of the two species x and y , and v is the relative velocity of the two species. If the two species are identical, then r is divided by two to eliminate double-counting. Calculation of the total reaction rate involves the integral over all velocities, but because there are two species with different masses, the reaction rate involves a double integral over both distributions:

$$\langle \sigma v \rangle = \int_0^\infty \int_0^\infty \phi(v_x) \phi(v_y) v \sigma(v) dv_x dv_y \quad (5.3)$$

Transforming the two velocities v_x and v_y into center-of-mass coordinates v and V , the double integral changes to two independent integrals. Performing the integration over the variable V (the velocity of the center-of-mass) the reaction rate per particle pair is

$$\langle \sigma v \rangle = \int_0^\infty \phi(v) v \sigma(v) dv. \quad (5.4)$$

Inserting the velocity distribution with the reduced mass μ , and using the center-of-mass energy $E = \frac{1}{2}\mu v^2$ we arrive at:

$$\langle \sigma v \rangle = \left(\frac{8}{\pi\mu} \right)^{1/2} \frac{1}{(kT)^{3/2}} \int_0^\infty \sigma(E) E \exp\left(-\frac{E}{kT}\right) dE \quad (5.5)$$

If the reaction proceeds through a narrow resonance then the reaction cross section

takes on a Breit-Wigner form:

$$\sigma_{BW}(E) = \pi\lambda^2 \frac{2J+1}{(2J_1+1)(2J_2+1)} (1 + \delta_{12}) \frac{\Gamma_a \Gamma_b}{(E - E_r)^2 + \left(\frac{\Gamma}{4}\right)^2} \quad (5.6)$$

The resonance is assumed narrow if $\Gamma \ll E_r$. Over this small energy range the Maxwell-Boltzmann energy distribution is flat, takes on the value at the resonance energy and comes out of the integral. Performing just the cross section integral:

$$\int_0^\infty \sigma_{BW}(E) dE = 2\pi^2 \lambda^2 \omega \frac{\Gamma_a \Gamma_b}{\Gamma} \quad (5.7)$$

where ω is the statistical factor in Equation 5.5. The resonance strength is defined as $\omega\gamma = \omega \frac{\Gamma_a \Gamma_b}{\Gamma}$.

For radiative proton capture, the proton widths for the reaction are determined by the Coulomb and centrifugal barriers. These depend on the radial wave functions and the form of the potential taken for the nuclear part of the interaction, and are given by:

$$\Gamma_l(E) = \frac{3\hbar}{R_n} \left(\frac{2E}{\mu}\right)^{1/2} P_l(E, R_n) \theta_l^2 \quad (5.8)$$

where R_n is the radius in the nucleus where the capture occurs $P_l(E, R_n)$ is the probability of penetrating the barrier for a given angular momentum l , and θ_l^2 is generally called the reduced width of the state. This is essentially the probability that the capture leaves the resulting nucleus in that state. The penetrability is defined as the absolute square of the ratio of the radial wave functions at infinity and inside the barrier, and depends on the energy and angular momentum of the resonance.

Finally, the resonant capture reaction rate can be expressed as:

$$\langle \sigma v \rangle = \left(\frac{2\pi}{\mu kT} \right)^{3/2} \hbar^2 \omega \gamma \exp\left(-\frac{E_r}{kT}\right) \quad (5.9)$$

Because of the exponential dependence, uncertainties of 100 keV in the resonance energy can mean orders of magnitude uncertainty in the reaction rate. The uncertainty also enters through the resonance strength but is usually less dramatic. The proton widths are typically linear functions of the resonance energy over the uncertainty range. The gamma widths go as $E^{2\lambda+1}$, where λ is the multipolarity of the transition, and depend on the initial and final quantum numbers, so the spin-parity assignments for the levels involved are also needed to determine the resonance strengths. Experimental determination of spin-parity assignments is preferred but not always available. Reaching very proton rich species with such reactions requires special targets which maybe difficult to manufacture. In the absence of experimental information shell model calculations provide accurate spin-parity assignments of the levels involved.

Factoring in constants, a usable form of the reaction rates derived above is as follows [He95]:

$$N_A \langle \sigma v \rangle = 1.54 \times 10^{11} (AT_9)^{-3/2} \omega \gamma [\text{MeV}] \exp\left(\frac{-11.605 E_r [\text{MeV}]}{T_9}\right) \text{cm}^3 \text{s}^{-1} \text{mole}^{-1} \quad (5.10)$$

where the reduced mass A is given by $A_p A_T / (A_p + A_T)$ and A_p is the proton mass and A_T is the target mass. The resonance strength is given by

$$\omega \gamma = \frac{(2J+1) \Gamma_p \Gamma_\gamma}{2(2J_T+1) \Gamma} \quad (5.11)$$

where J is the spin of the compound nucleus and J_T is the spin of the target. The proton width is normally determined by $\Gamma_p = C^2 S \cdot \Gamma_{sp}$, where $C^2 S$ is the single particle spectroscopic factor and Γ_{sp} is the single particle width. The Γ_{sp} is determined by

calculating phase shifts of the protons scattering off a Woods-Saxon potential whose depth is determined by matching the resonance energies.

The gamma decay widths Γ_γ are determined from the reduced electromagnetic transition probabilities and have an energy dependence specific to the type of transition. The reduced transition probabilities are usually determined using shell model calculations. The transitions of importance here are either E2 or M1 transitions and the gamma widths are given by:

$$\Gamma_{E2}[\text{eV}] = 8.13 \times 10^{-7} E_\gamma^5 [\text{MeV}] B(E2) [\text{e}^2 \text{fm}^4] \quad (5.12)$$

and

$$\Gamma_{M1}[\text{eV}] = 1.16 \times 10^{-2} E_\gamma^3 [\text{MeV}] B(M1) [\mu_N^2] \quad (5.13)$$

Direct reaction cross section measurements are the preferred approach for determining these capture reaction rates. However, the cross sections become prohibitively small at stellar energies because of the repulsion due to the Coulomb barrier so other experimental methods must be employed to gain information about the levels. Indirect spectroscopic measurements have been successfully used to determine energy levels in proton rich nuclei using multinucleon transfer reactions. The (${}^7\text{Li}, {}^8\text{He}$), (${}^3\text{He}, {}^8\text{Li}$), and (${}^4\text{He}, {}^8\text{He}$) reactions are examples of reactions that have been successfully used in the past for spectroscopic measurements of proton rich nuclei [Wi88,Wi98,Be75,Be77,Sc97].

5.1.3 Why study ${}^{27}\text{P}$?

The level structure of ${}^{27}\text{P}$ governs the proton capture reaction rate on ${}^{26}\text{Si}$ and dramatically affects the procession of the rp-process through the waiting point nucleus ${}^{26}\text{Si}$ ($t_{1/2}=2.2$ seconds). (A waiting point nucleus is one with a half-life comparable to the duration of the explosive event.) If the proton capture rate is small enough, the rp-process

must wait for ^{26}Si to beta decay before proceeding to higher masses. Also, if ^{26}Si remains at the end of an explosive event, it beta decays through an excited state of ^{26}Al directly to the ground state of ^{26}Mg , bypassing the ground state of ^{26}Al . It is the β^+ decay of the ^{26}Al ground state to an excited state of ^{26}Mg that produces the characteristic 1.8 MeV gamma ray. The important point to note here is that the characteristic 1.8 MeV gamma ray from ^{26}Al beta decay is not produced. Therefore, it becomes important to predict the amount of ^{26}Si produced during the event in order to understand the gamma ray observatory observations of ^{26}Al gamma rays from explosive events. Several reactions contribute to the population of this nucleus, shown schematically in Figure 5.2. Proton capture on ^{25}Al and beta decay of ^{26}P increase the population, while proton capture on ^{26}Si and its beta decay decrease the population. This is just a subset of the much more complex network of reactions in the rp process, shown in Figure 5.1.

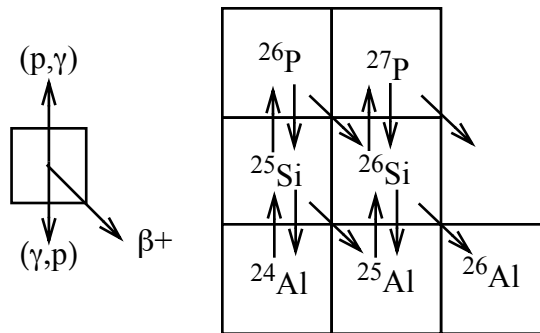


Figure 5.2: Subset of the chart of the nuclides schematically showing the rp-process reactions affecting the abundance of ^{26}Si . This is just a small subset of the total reaction network (see Figure 5.1).

The proton threshold in ^{27}P is at 0.897(35) MeV. Experiments have reported only one excited state at 1.66(4) MeV [Be77] using the $^{32}\text{S}(^3\text{He}, ^8\text{Li})^{27}\text{P}$ reaction at 70 MeV and 7° (see Figure 5.3). Recently a shell model calculation suggested there is a state at 1.18 ± 0.10 MeV, but there is no experimental report of this state. Examination of Benen-

son *et al.* spectrum indicates the possibility of a state at ~ 1.2 MeV, but it wasn't reported. A level at ~ 1.2 MeV would change the proton capture rate by orders of magnitude at certain temperatures. Network calculations at these temperatures then show a substantial depletion of the ^{26}Si nucleus, and an enhancement of ^{27}P and ^{28}S . Thus, experimental verification of this level is highly desired and another measurement would prove useful.

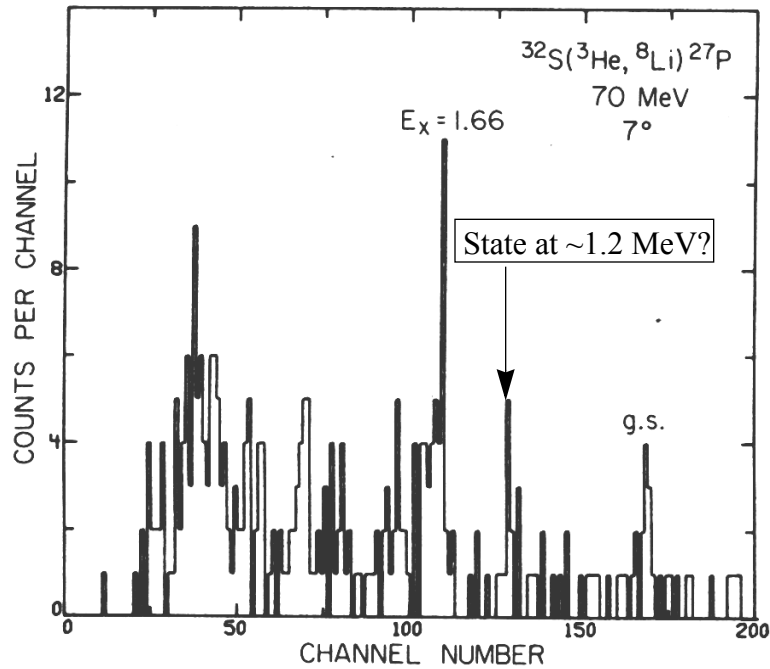


Figure 5.3: Benenson's spectroscopic measurement of ^{27}P [Be77]. There appears to be a state at ~ 1.2 MeV, but wasn't reported.

5.1.4 Why study ^{23}Al ?

The level structure of ^{23}Al determines the proton capture reaction rate on ^{22}Mg . In the ^{23}Al case, the Q-value for the (p,γ) reaction is very low at 0.13 MeV and thus competes with photodisintegration. Processing more ^{22}Mg into ^{23}Al and beyond decreases the amount of ^{22}Na produced in the explosion. There has been one observation of an excited state at 0.46 ± 0.06 MeV by Wiescher *et al.* [Wi88] using the $^{24}\text{Mg}(^7\text{Li}, ^8\text{He})^{23}\text{Al}$ reaction at

190 MeV but was not resolved from the ground state (see Figure 5.2).

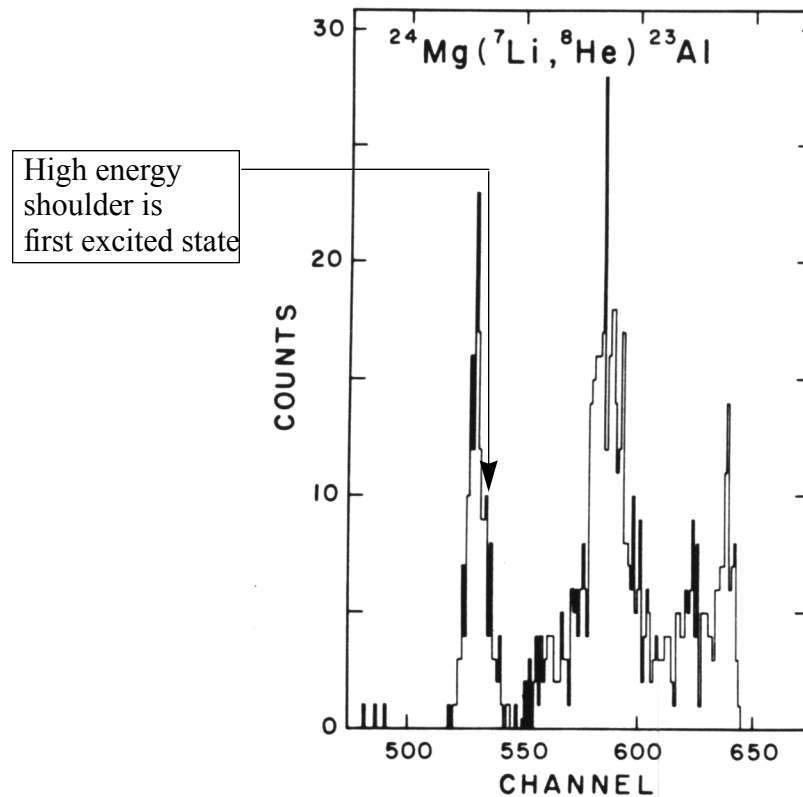


Figure 5.4: Previous spectroscopic measurement of ^{23}Al . The first excited state is not resolved from the ground state [Wi88].

Using the same reaction and the S800 spectrograph, it should be possible to resolve the two states and measure its location to 5 keV accuracy. Since this level is so close to the proton threshold, an uncertainty of 60 keV can mean orders of magnitude uncertainty in the reaction rate. Thus, resolving the first excited state from the ground state is highly desirable. An uncertainty of 5 keV would translate into an acceptable 10% uncertainty in the reaction rate.

5.2 Experiment

The experiment employed the S800 spectrograph in the dispersion-matched,

energy-loss mode. A primary beam of 50.1(3) MeV/u ^7Li entered the S800 at the object position, the beam was transmitted to the target position in the main scattering chamber of the S800, and targets of ^{28}Si and ^{24}Mg were used to populate states in ^{27}P and ^{23}Al with the binary transfer reaction ($^7\text{Li}, ^8\text{He}$). The beam interacted with the targets, and the $^8\text{He}^{2+}$ ions were swept to the focal plane detectors by the spectrograph magnets. The angular coverage of the spectrograph was 0-12° in the laboratory.

The targets used were 0.94 mg cm⁻² ^9Be , 0.34 mg cm⁻² ^{10}B mounted on a 30 μg/cm² carbon backing, 0.63 mg cm⁻² ^{24}Mg , and 1.4 mg cm⁻² natSi. The transverse size of the targets is modestly important for background reduction, especially given how thin the targets are. Since the image in the main scattering chamber is dispersive (12 cm/%), and there is roughly a 0.08% momentum spread in the primary beam, the beam spot size will be about 1 cm on target. Beam tails can react with the target frame and produce an undesirable background in the focal plane. Targets of at least 12 mm in diameter were chosen to minimize this kind of background.

The natural silicon target was a 2" diameter circular silicon wafer obtained from a silicon chip manufacturer, Virginia Semiconductor, placed in a 45 mm diameter circular frame. The target was extremely uniform (at the 0.1% level) and was oxygen free but contained the natural abundances of other silicon isotopes. The target was 1.4(1) mg/cm² thick as specified by the manufacturer and was verified with alpha-particle energy loss. Prior to the experiment, it was not known whether the 4.3% ^{29}Si and 3.7% ^{30}Si contaminants in the target would pose contamination problems.

The ^{24}Mg target was 99.9% enriched and was 0.63(2) mg/cm² thick mounted in a 20 mm square frame. The thickness was measured with alpha-particle energy loss.

The target thicknesses were verified by measuring the energy loss of the beam through them. This method is only good to 10% absolute target thickness because of the uncertainty in stopping power of the target materials for a ${}^7\text{Li}$ beam of 50 MeV/u. Alpha-particle energy-loss measurements (typically done with alphas from ${}^{241}\text{Am}$ and mixed thorium sources) are much more accurate for the silicon and magnesium targets because of the quantity of existing stopping power data (see [Zi91]). Nevertheless, beam measurements were within error of the alpha-particle measurements.

The ${}^7\text{Li}$ primary beam was first transported to the focal plane of the spectrograph to check the dispersion matching. Ideally, the width of the peak at the focal plane should be $\leq 0.01\%$ of the total beam energy. Figure 5.5 shows a spectrum of the position in the dispersive direction at the first tracking detector. The peak has a non-Gaussian shape with a full width of $\Delta E/E=0.03\%$, but this is acceptable because the resolution was limited by kinematic broadening due to the primary beam divergence ($\Delta\theta\sim 5\text{mrad}$, $\Delta\phi\sim 5\text{ mrad}$ FWHM) to 0.05-0.1%.

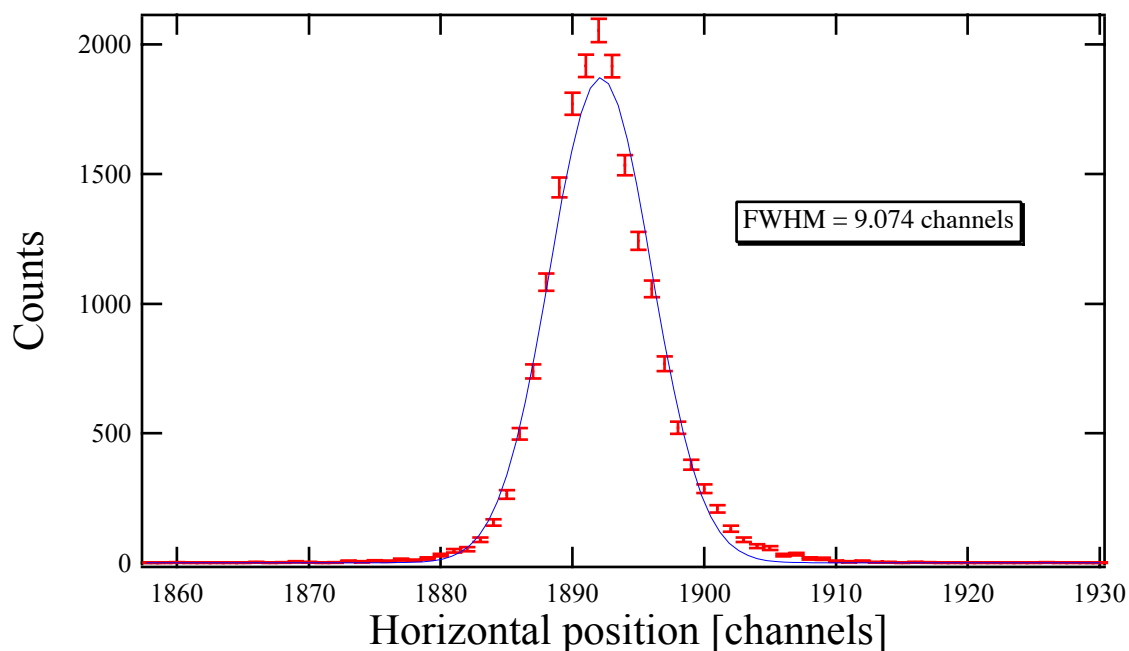


Figure 5.5: Primary beam spot at the focal plane, used to check the dispersion matching of the spectrograph for the experiment. The line through the data points is a single Gaussian fit; the error bars are statistical. The beam was transmitted to the focal plane from the object position with the spectrograph in dispersion matched mode. The FWHM of the peak corresponds to an energy resolution of $E/\Delta E \sim 4000$.

The detector positions were calibrated by inserting masks just upstream of the tracking detectors and illuminating the holes with primary beam, as described in Chapter 4. The x-position (dispersive direction) is “hard-wired” in the detectors, so only the center of the detector has to be determined. The y-position is determined by drift time of the electrons from the ionization to the anode wire, and depends on several factors including gas mixture and drift voltage. Gradual changes in the y-position through time was observed in this experiment as in the ^{10}Li experiment (see Chapter 4). The magnitude of the effect ($\sim 10\%$) was much smaller than in the ^{10}Li experiment, and a much better monitoring method was available. The $^7\text{Li}^{2+}$ charge state of the beam provided a very nice monitor of the drifting y position as well as magnet fluctuations.

Particle identification in this experiment was straightforward. Not only were the particle groups clearly separated with no overlap, but a ${}^7\text{Li}^{2+}$ charge state of the beam comes strongly and provided a constant reference. Figure 5.6 shows a particle identification spectrum for this experiment. Singly charged alpha particles from the reaction arrive at the focal plane at the same time. The ${}^8\text{He}^{2+}$ and ${}^4\text{He}^{1+}$ lose similar amounts of energy in the ion chamber and CRDCs, but the ${}^8\text{He}^{2+}$ ions have twice the total energy. Hence, the total E-TOF spectrum was used to identify the ${}^8\text{He}^{2+}$ ions.

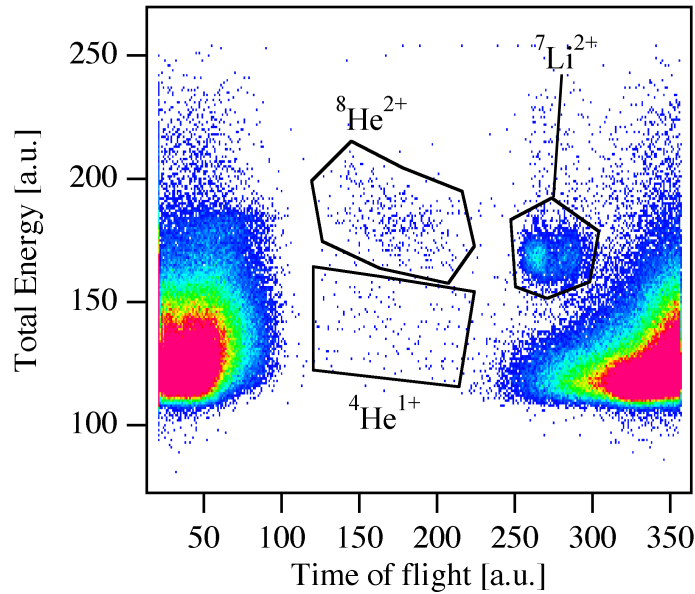


Figure 5.6: Particle identification spectrum for this experiment.

5.3 Results

Energy calibrations were performed by inserting the ${}^9\text{Be}$ and ${}^{10}\text{B}$ targets and observing the $({}^7\text{Li}, {}^8\text{He})$ reaction without changing the spectrograph settings. Calibrations using the ${}^9\text{Be}({}^7\text{Li}, {}^8\text{He}){}^8\text{B}$ reaction were performed regularly throughout the experiment; the ${}^{10}\text{B}({}^7\text{Li}, {}^8\text{He}){}^9\text{C}$ measurements were done near the end of the experiment.

The ground state Q-values of the ${}^{10}\text{B}({}^7\text{Li}, {}^8\text{He}){}^9\text{C}$ and ${}^9\text{Be}({}^7\text{Li}, {}^8\text{He}){}^8\text{B}$ reactions

are $-33.5534(74)$ and $-28.2636(71)$ MeV, respectively [Au95]. The errors on these values are dominated by the 7 keV ^8He mass error. Three peaks were populated in the ^8B nucleus: the ground state and excited states at $0.774(6)$ and $2.32(3)$ MeV. The first excited state in ^8B (0.774 MeV) was used in the calibration, but the ^8B (2.32 MeV) state was not used. Only the ground state of ^9C was populated. A magnet excursion roughly halfway through the experiment was accounted for by observing the peak shift in the $^9\text{Be}(^7\text{Li},^8\text{He})^8\text{B}$ reaction, and applying the same shift to all spectra following the excursion.

The energy and scattering angle of each event were reconstructed using the techniques described in Chapter 4 and Appendix B lists the reconstruction coefficients used. Energy spectra were created by applying kinematic shifts to all events to shift the energy to what it would be at 0° . In other words, all events having the same Q-value appear in the same peak after the shifts are applied. Figure 5.7 shows kinematic spectra for the two calibration reactions before shifting the energies.

The expected line shape from a kinematic simulation including finite beam emittance is a Lorentzian. All data points in the fits were weighted according to Poisson statistics. The two lowest states in ^8B were fit with a double Lorentzian with identical widths plus constant and linear backgrounds. Holding the widths of the two states equal is appropriate because the intrinsic state width does not contribute to the width of the peak; the width of the peak is dominated by kinematic broadening effects described in Chapter 4. The ground state of ^9C was fit with a pure Lorentzian plus a constant background. The two states of ^{23}Al were fit with a double Lorentzian with identical widths plus a constant background. Allowing the width of the second state to vary gives an identical result with

no significant change in χ^2 . The ground state peak of ^{27}P was fit by a single Gaussian plus a constant background. The next two higher-lying peaks were fit with a double Gaussian with equal widths plus a constant background. The widths of all of these ^{27}P peaks were equal within errors. The large, broad structure around channel 140 was fit with a skewed Gaussian (an additional x^3 term in its argument) and a constant background. Fitting all peaks with Gaussian or Lorentzian line shapes had a negligible effect on the results. The fits to the ^{23}Al and ^{27}P energy spectra are shown in Figures 5.10 and 5.11 respectively.

The ^{29}Si and ^{30}Si contaminants in the silicon target don't appear to cause significant spectrum contamination, illustrated in the lower left panel in Figure 5.7 and the bottom panel in Figure 5.8.

Figure 5.9 is a plot of the energy calibration for this experiment.

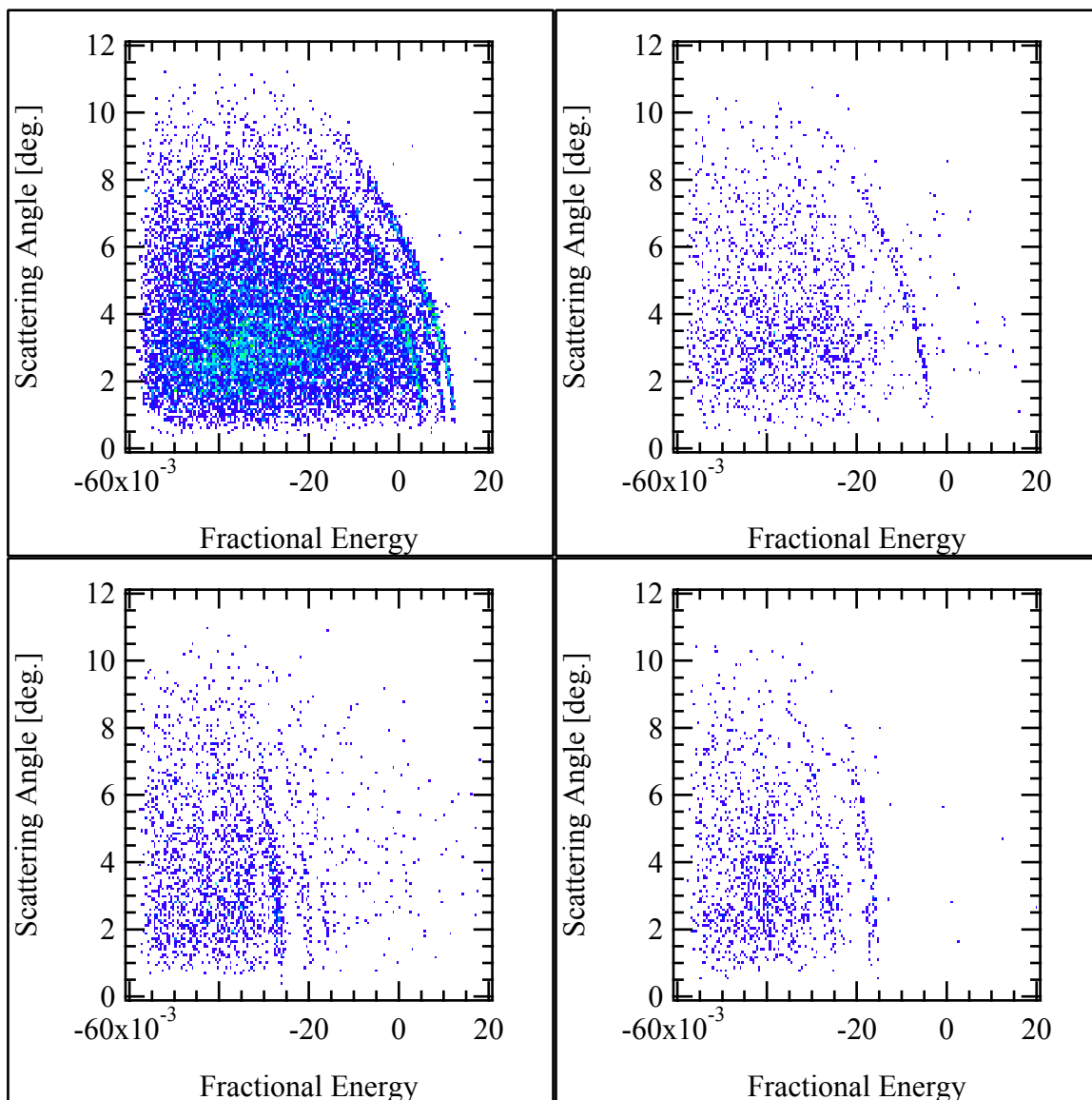


Figure 5.7: All kinematic spectra for this experiment. The fractional energy is relative to the central energy and defined as $(E-E_0)/E_0$. The resolution is better at lower angles because of the reduced kinematic broadening effects at lower scattering angles (see Chapter 4).

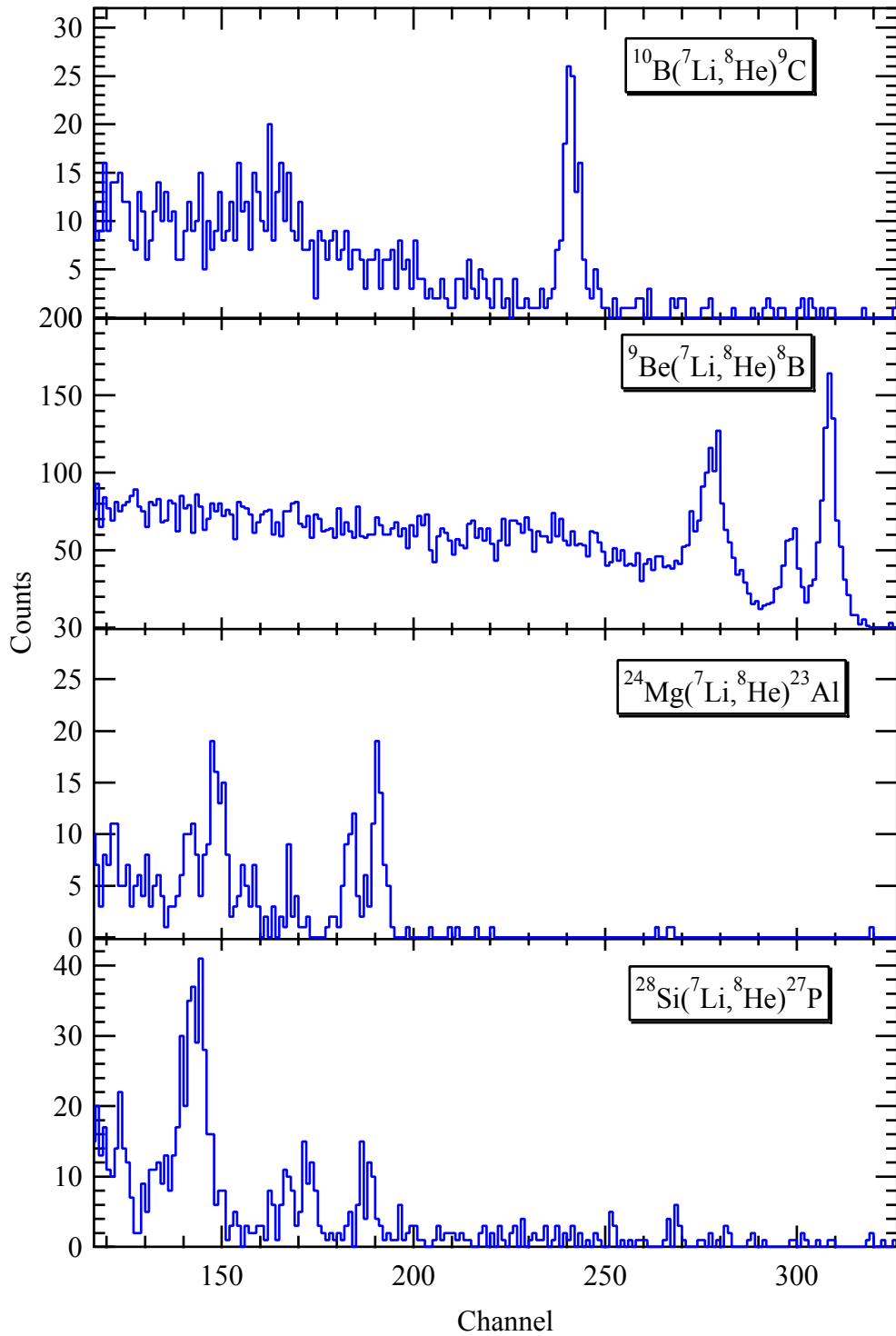


Figure 5.8: ^8He energy spectra for the listed reactions at $E(^7\text{Li})=50.1$ MeV/u and $\Theta_{\text{lab}}=0\text{-}12^\circ$.

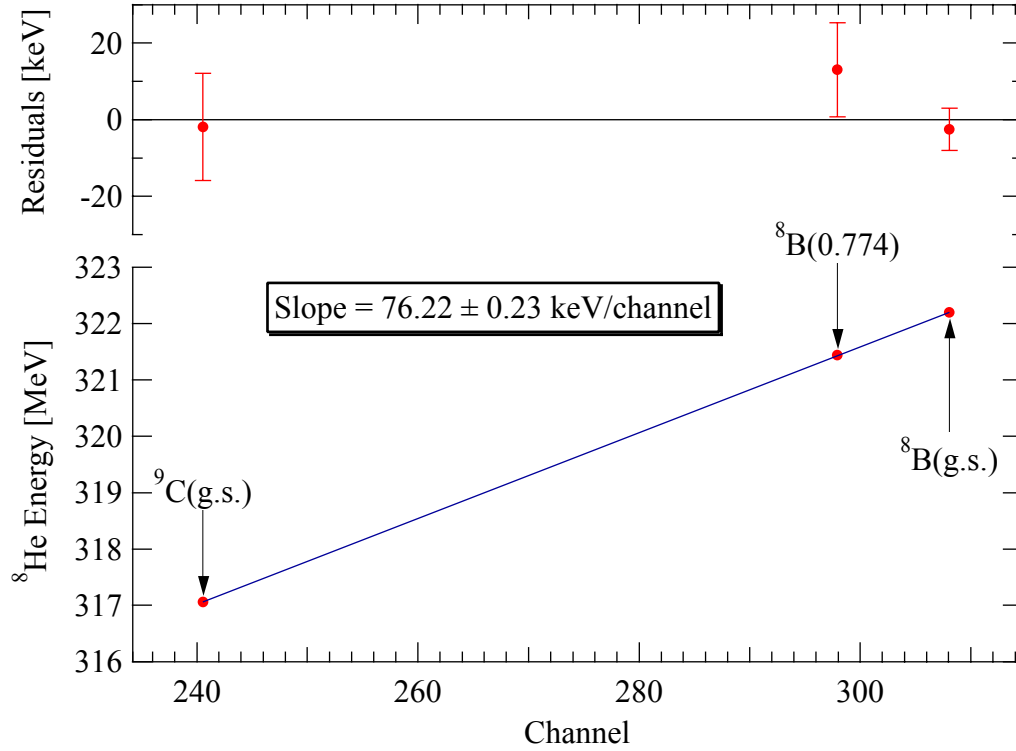


Figure 5.9: ⁸He energy calibration for this experiment. The line through the data is a linear fit. Errors on the points are statistical uncertainties (translated into energy) and mass errors of the calibration nuclei summed in quadrature. The mass errors are taken from the 1995 Mass Evaluation Update [Au95].

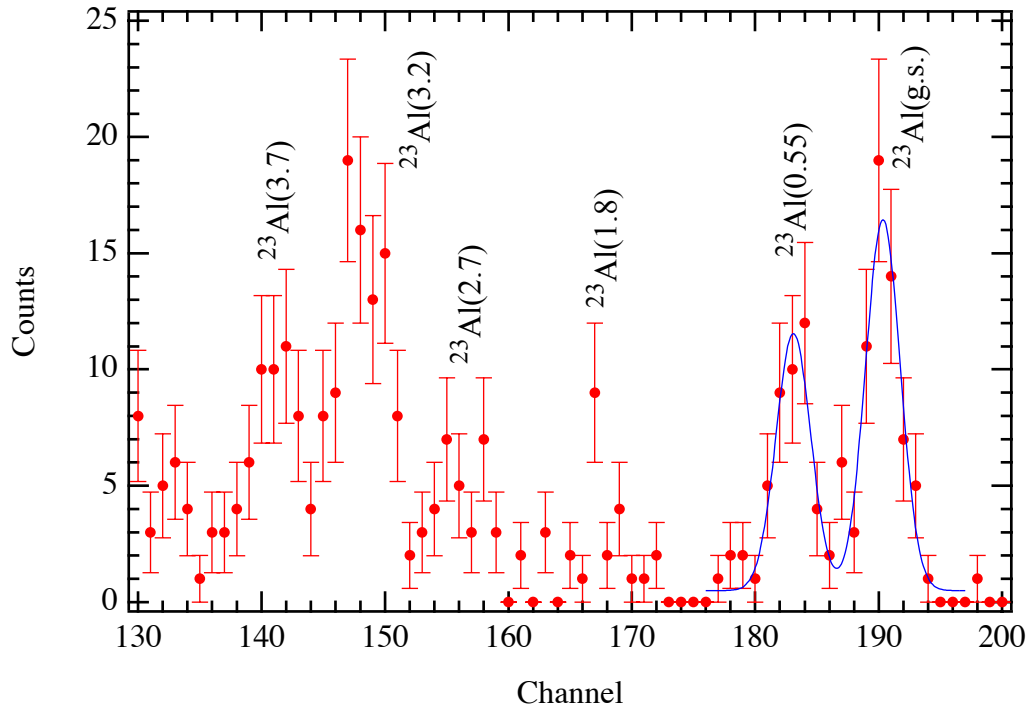


Figure 5.10: The energy spectrum of the $^{24}\text{Mg}(^7\text{Li}, ^8\text{He})^{23}\text{Al}$ reaction.

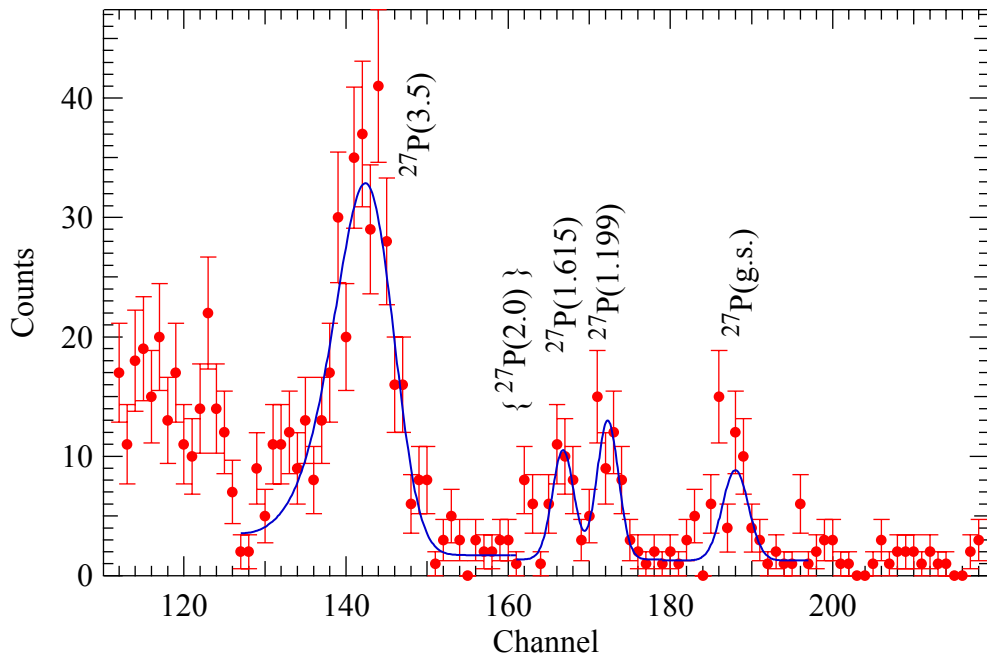


Figure 5.11: The energy spectrum of the $^{28}\text{Si}(^7\text{Li}, ^8\text{He})^{27}\text{P}$ reaction.

Table 5.1: Experimental observations of states in ^{23}Al .

Mass Excess [MeV]	Excited State Loc. [MeV]	Prev. Exp. M.E. [MeV]
6.773(28)	0.00	6.767(25)[Be75]
7.322(30)	0.550(20)	7.23(6) [Wi88]
8.545(44)	1.773(35)	--
9.348(42)	2.575(34)	--
9.95(33)	3.204(21)	--
10.47(36)	3.699(24)	--

Table 5.2: Experimental observations of states in ^{27}P .

Mass Excess [MeV]	Excited State Loc. [MeV]	Prev. Exp. M.E. [MeV] [Be77]
-0.670(41)	0.00	-0.753(35)
0.529(42)	1.199(19)	--
0.945(44)	1.615(21)	0.91(4)
2.783(46)	3.453(22)	--

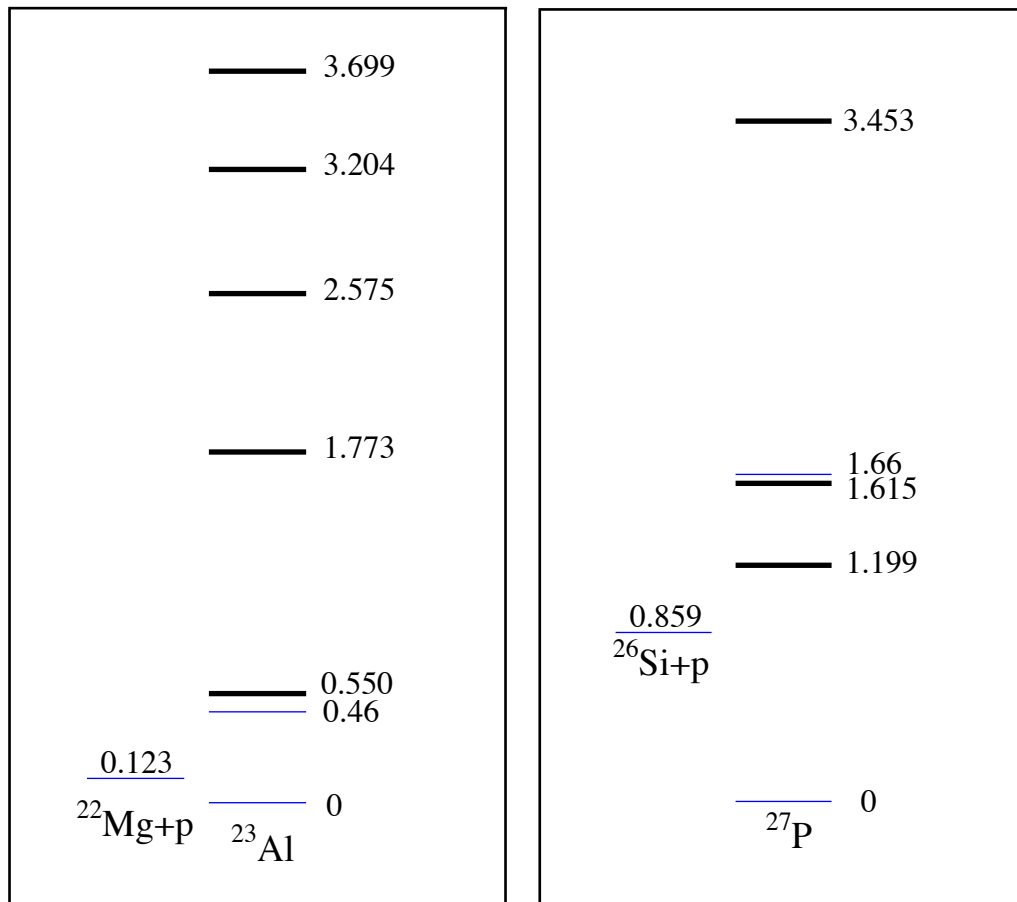


Figure 5.12: New level schemes for ^{23}Al and ^{27}P following this experiment. The thick lines are measurements reported here; the thin lines are previous measurements. The excited state locations are given relative to the ground state of the nucleus from their respective measurements. The proton separation energies are a weighted average of the present ground state mass measurements and those of Benenson *et al.* in the seventies [Be75, Be77].

The errors on the energies are a quadrature sum of the calibration mass errors. As described in Chapter 4, RELMASS was used to determine the masses of the states in the nuclei ^{23}Al and ^{27}P . The beam energy, target thicknesses, scattering angle (0°), and channel locations were input as calibrations. The mass excess of all peaks in ^{23}Al and ^{27}P are given as output and are summarized in Tables 5.1 and 5.2.

Absolute mass errors were a combination of statistics, calibration mass errors, beam energy, target thickness, and scattering angle, which dominated (21 keV for ^{23}Al and 36 keV for ^{27}P). The errors in excited state location quoted in Tables 5.1 and 5.2 are purely statistical. The astrophysical significance of these measurements requires that resonant energies (energies above the proton threshold) be quoted. The Tables give a mass excess for each state, excited state location within the nucleus, and location with respect to the proton separation energy of the nucleus.

5.4 Discussion

5.4.1 The Isobaric Multiplet Mass Equation (IMME)

The IMME is an empirical equation which relates the masses of isobaric analog states to each other based on their z-axis projection of isospin [Be79]. The equation is a good predictor of masses among isobaric multiplets and is as accurate as the input data allow. Its form is a quadratic polynomial relating the mass excess of multiplet states as $ME = a + bT_z + cT_z^2$. The IMME coefficients for many isobaric multiplets have been determined [Be79].

The ^{23}Al and ^{27}P ground states belong to isobaric quartets of $T=3/2$. Figure 5.13 shows the $A=23$, $J^\pi=5/2^+$, $T=3/2$ isobaric quartet mass excesses plotted as a function of T_z . The ground state ^{23}Al is the $T_z=-3/2$ member of the quartet. The $A=23$ $T=3/2$ IMME coef-

ficients calculated using the current measurement along with the other three measurements [Az89] agree with those published in the 1979 Benenson and Kashy review article. Combining the previous value of the ^{23}Al mass excess with this one gives a mass excess of $6.770(19)$ keV.

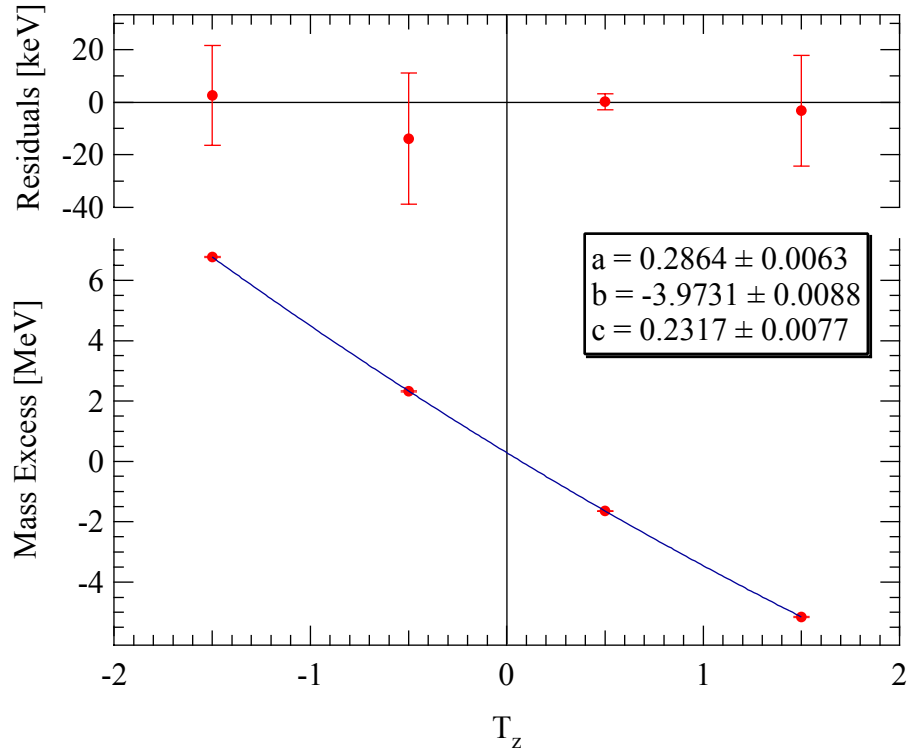


Figure 5.13: Mass excesses for the $A=23$, $J^\pi=5/2^+$, $T=3/2$ isobaric quartet. The line through the data is a quadratic fit; the box lists the coefficients from the fit with errors in MeV.

Figure 5.14 shows the $A=27$, $J^\pi=1/2^+$, $T=3/2$ isobaric quartet mass excesses plotted as a function of T_z . The ground state of ^{27}P is the $T_z=-3/2$ member. There is a small disagreement with the present mass excess of $-0.670(41)$ MeV and the previous measurement of $-0.753(35)$ MeV, but both measurements agree, within errors, with the IMME prediction of $-716(16)$ MeV in the review article. A weighted average of the two measurements yields a mass excess for the ground state of ^{27}P of $-715(27)$ keV. This

value is used for determining the IMME coefficients in Figure 5.15 and Table 5.3.

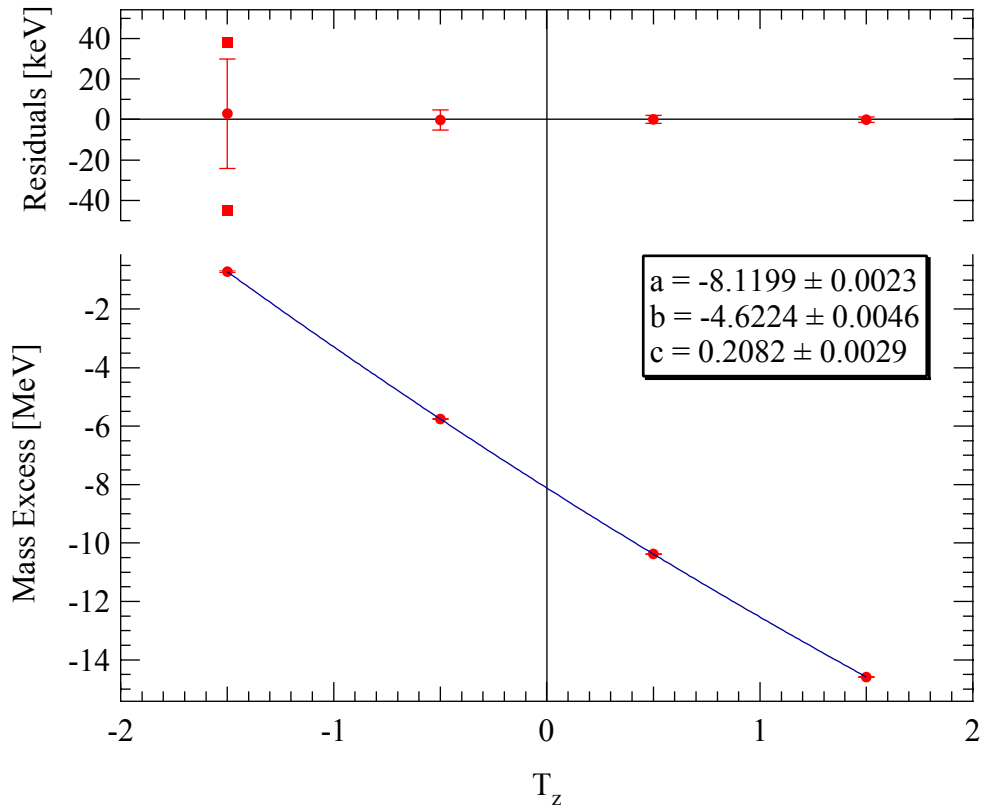


Figure 5.14: Mass excesses of the $A=27$ $J^\pi=1/2^+$ $T=3/2$ isobaric quartet. The line through the data is a quadratic fit; the box shows the fit coefficients and their errors in MeV. The two solid squares are this measurement (lower) and Benenson's measurement.

Table 5.3: IMME coefficients for the A=23 and A=27, T=3/2 isobaric multiplets.

Coef.	A=23, $J^\pi=5/2^+$, T=3/2		A=27, $J^\pi=1/2^+$, T=3/2	
	Present	Past [Be79]	Present	Past [Be79]
a	0.286(6)	0.287(4)	-8.120(2)	-8.120(2)
b	-3.973(9)	-3.973(8)	-4.622(5)	-4.629(5)
c	0.232(8)	0.230(4)	-0.208(3)	0.207(3)

In the review article, the possibility of a cubic term or “d” coefficient is discussed. The cause of such a term would be the significant expansion of the wave function in the lowest isospin member of the multiplet due to Coulomb repulsion. If the wave function was $s_{1/2}$ in nature, the lack of a centrifugal barrier may cause additional expansion. The ^{27}P nucleus is a good test of this because it is proton rich and its ground state is $s_{1/2}$. When the multiplet is fit with a cubic, with $d=1(5)$ keV, consistent with zero. The A=23 case was also fit with a cubic, yielding $d=8(13)$ keV, again consistent with zero.

5.4.2 Astrophysical implications

The measurement of the excited states have a direct effect on the proton capture rates described earlier in this chapter. Specifically the excited state at 0.550(19) MeV in ^{23}Al and the newly reported 1.199(19) MeV in ^{27}P . In these specific cases (^{23}Al and ^{27}P), the proton and gamma widths have been previously determined for the levels that dominate the resonant capture rates [Wi88, He95]. Equations 5.12 and 5.13 describe how the gamma widths scale with energy. The proton width is insignificant for the ^{23}Al case because $\Gamma_\gamma \ll \Gamma_p$. In the case of ^{27}P , the proton and gamma widths are of the same order, so both must be scaled slightly. Alex Brown has made several calculations illustrating how the $^{26}\text{Si}(p,\gamma)$ proton width scales with resonance energy. The dependence is linear

over the small range of use. The widths and resonance strengths are listed in Tables 5.4 and 5.5.

Figures 5.15 and 5.16 show the difference in reaction rates based on the old and new experimental information. At temperatures between 0.1 and 3 GK the $^{26}\text{Si}(p,\gamma)^{27}\text{P}$ reaction rate is greatly enhanced. This leads to a significant depletion of ^{26}Si and ^{26}Al and a substantial enhancement of ^{27}P and, at higher temperatures, ^{28}S . See [He95] for details. The $^{22}\text{Mg}(p,\gamma)^{23}\text{Al}$ reaction rates are very similar to those published in [Wi88] but slightly lower with improved error bars. This will cause a slight enhancement of the ^{22}Na in the temperature range 0.1-1.0 GK compared to previous predictions.

Table 5.4: Resonance parameters the levels that dominate resonant proton capture in the $^{22}\text{Mg}(p,\gamma)^{23}\text{Al}$ reaction.

E^*	E_p	Γ_γ [eV]	Γ_p [eV]	J^π	$\omega\gamma$ [eV]
0.550(20)	0.430	7.63E-07	32	$5/2^+$	7.63E-07

Table 5.5: Resonance parameters the levels that dominate resonant proton capture in the $^{26}\text{Si}(p,\gamma)^{27}\text{P}$ reaction.

E^*	E_p	Γ_γ [eV]	Γ_p [eV]	J^π	$\omega\gamma$ [eV]
1.199(19)	0.385	1.43E-03	2.33E-03	$3/2^+$	1.77E-03

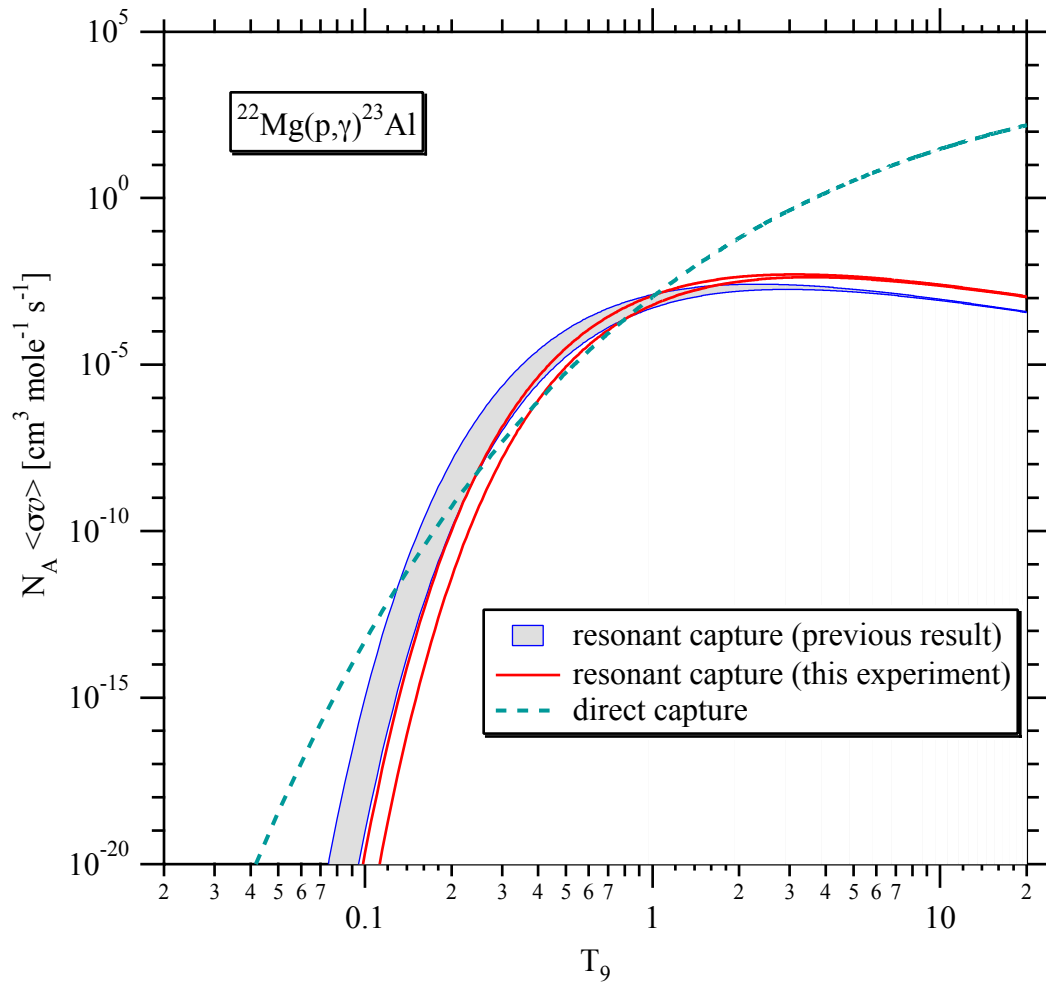


Figure 5.15: Astrophysical reaction rates using data from past and present experiments.

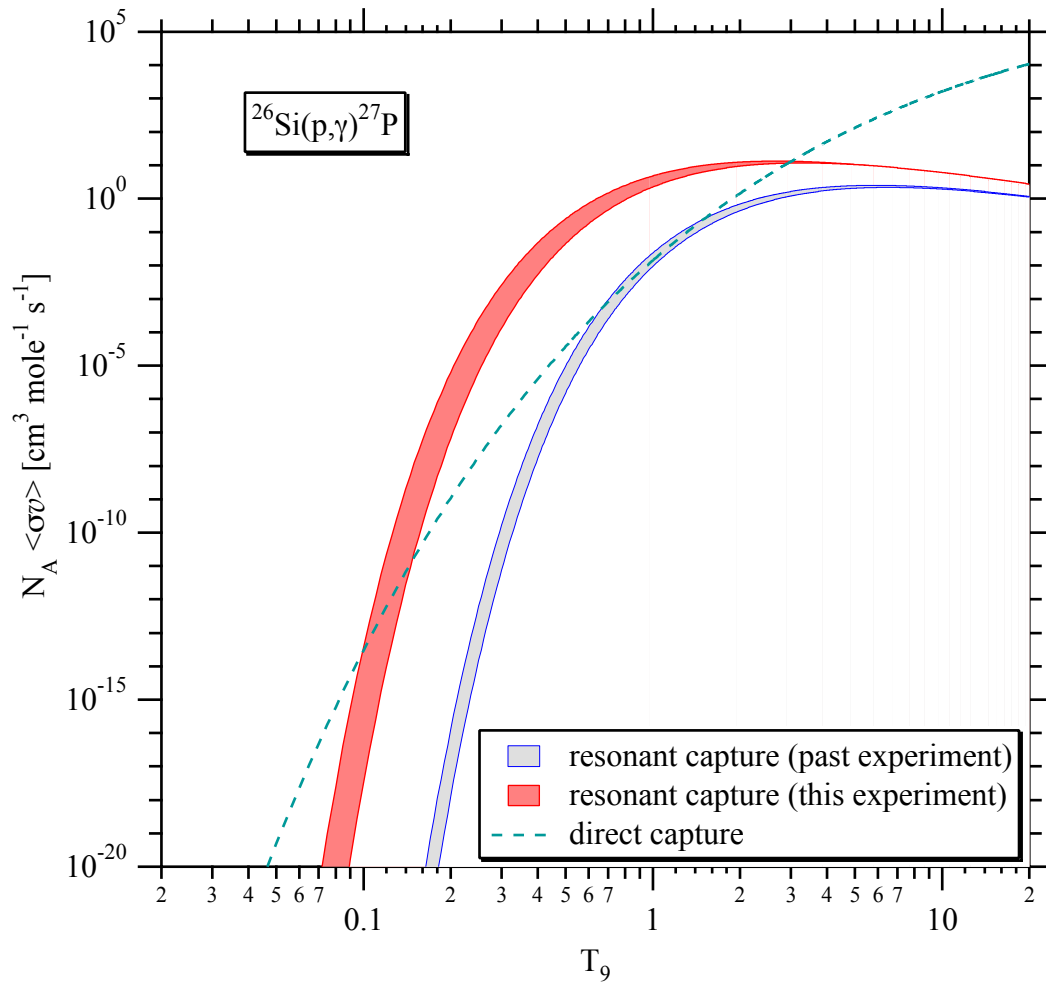


Figure 5.16: Astrophysical reaction rates due to past and present experiments. Note that the calculations of Herndl *et al.* [He95] agree with the present experiment.

5.5 Conclusions

High precision mass measurements ($\delta m/m \leq 1.6 \times 10^{-6}$) were made of several nuclear states including the ground states of two proton rich nuclei. The spectroscopic measurements in the two nuclei represent the first experimental report of some of the excited states in the nuclei. Astrophysical proton capture reaction rates for the rp process were calculated and found to deviate slightly from previous calculations but are now on a much firmer basis due to the smaller uncertainties. These will impact the mass flow dur-

ing explosive hydrogen burning events in specific temperature and density conditions, and it will be left up to the astrophysicist to run network calculations using the new, improved nuclear data.

Chapter 6

Summary

The S800 spectrograph was built at the NSCL and commissioned in September 1996. The magnetic fields of the spectrograph dipoles were measured to a precision of 1 Gauss after smoothing, and the data were used for transfer map calculations necessary to provide the high energy resolution of the S800. Features of the fields such as azimuthal curvatures, radial field gradients, and effective lengths were measured. Measurements of the central field region indicate that the maximum field gradient is ≤ 1 Gauss/cm, which meets the design criteria.

The S800 spectrograph was used for spectroscopic measurements of the exotic nuclei ^{10}Li , ^{23}Al , and ^{27}P . The $^9\text{Be}(^9\text{Be}, ^8\text{B})^{10}\text{Li}$ reaction was used to populate states in the particle unbound nucleus ^{10}Li . Definitive evidence for a p-wave state at $-S_n=500(60)$ keV, corresponding to a $^9\text{Be}(^9\text{Be}, ^8\text{B})^{10}\text{Li}$ reaction Q-value of $-33.59(6)$ MeV, was presented and agrees with previous spectroscopic measurements of ^{10}Li . A small excess of counts right at threshold is tantalizing but, given the experimental resolution, provides little information about low-lying s-wave or p-wave states. The experiment represents one more measurement with which to draw conclusions about the ^{10}Li nucleus. Future mea-

measurements are necessary to clarify the ^{10}Li situation. Possible future studies include re-measurement of the $^{10}\text{Be}(^{12}\text{C}, ^{12}\text{N})^{10}\text{Li}$ reaction, either with an improved ^{10}Be target or with a ^{10}Be beam, as a confirmation of the existence of the state at ~ 250 keV is desired.

The rp-process nuclei ^{23}Al and ^{27}P were studied spectroscopically through the reactions $^{24}\text{Mg}(^7\text{Li}, ^8\text{He})^{23}\text{Al}$ and $^{28}\text{Si}(^7\text{Li}, ^8\text{He})^{27}\text{P}$. The ground state mass excesses and low lying excited states were determined by measuring the Q-value of the $^{24}\text{Mg}(^7\text{Li}, ^8\text{He})^{23}\text{Al}$ and $^{28}\text{Si}(^7\text{Li}, ^8\text{He})^{27}\text{P}$ reactions which were $Q=-37.396(28)$ and $Q=-37.347(41)$, respectively. This measurement of the first excited state of ^{23}Al at 550(20) keV substantially reduces the error of the $^{22}\text{Mg}(p,\gamma)^{23}\text{Al}$ reaction in the rp process network and will reduce the uncertainty on the amount of the gamma ray emitter ^{22}Na produced in explosive hydrogen burning situations where the rp process is triggered.

The first experimental report of the first excited state in ^{27}P at 1.199(19) keV significantly increases the $^{26}\text{Si}(p,\gamma)^{27}\text{P}$ reaction rate in certain temperature and density conditions during explosive hydrogen burning. The effect can be as large as 3 orders of magnitude at $T=0.4$ GK and will have a significant effect on mass and reaction flow. This new rate also affects the amount of the gamma ray emitter ^{26}Al produced in explosive stellar events. The uncertainties on the excited states of ^{23}Al and ^{27}P are still large when considering their effect on reaction rates and even higher resolution measurements are still desired though not critical.

A recent review article points out that the dominant uncertainty in galactic ^{26}Al production is the rate of the $^{25}\text{Al}(p,\gamma)^{26}\text{Si}$ reaction in these explosive hydrogen burning scenarios in novae, which will bypass the production of the ^{26}Al ground state via $^{25}\text{Al}(\beta^+\nu)^{25}\text{Mg}(p,\gamma)^{26}\text{Al}$ [Ka98]. The $^{25}\text{Al}(p,\gamma)^{26}\text{Si}$ reaction proceeds through several

states just above threshold states in ^{26}Si . The special characteristics of the S800 are ideally suited for spectroscopic study of ^{26}Si with transfer reactions. For example, the $^{27}\text{Al}(^7\text{Li}, ^8\text{He})^{26}\text{Si}$ or the $^{28}\text{Si}(p,t)^{26}\text{Si}$ reactions could be used to populate states near the proton threshold. The high resolution and larger cross section possible with the (p,t) reaction makes this a particularly attractive option.

High resolution studies of exotic, unstable nuclei and those with astrophysical significance are now possible and will continue to be performed with the S800. Until direct measurements of (p, γ) reactions are possible, the S800 will continue to provide invaluable, indirect astrophysical information. Higher precision mass measurements using very low cross section transfer reactions are now possible and will continue. Experiments using the high intensity radioactive beams to be delivered by the coupled cyclotron project coupled with the capabilities of the S800 will undoubtedly be fruitful.

Appendix A

Mapper Post-Processing Software

A.1 Introduction

The program D1_D2 was written to read and process raw map files from the mapping campaign described in Chapter 3. The software was written in VAX Fortran for the Digital Equipment Corporation's Alpha servers at the NSCL. This appendix will briefly describe how to use the software, and input and output file formats.

A.2 How to use the software

To run the program, type:

```
RUN DISK$$S800:[CAGGIANO.MAPPER.D1D2]D1_D2.EXE
```

Depending on the options selected, it may take up to 2 hours of CPU time to process a map, so the program must be run in batch mode. The program also uses some large arrays, so the user will need access to 80 MB of working space.

All that is needed to run the program is the name of an input file which contains all the important information necessary to process the map. Map file names, calibration file names, current settings, how to process the map, etc. is all passed to the program through this input file. The input file is a simple text file containing keywords followed by appro-

appropriate parameters. The parameters vary depending on the keyword detected. The user specifies the name of the input file and the program reads commands from the file. The commands don't have to occur in any particular order. If a command is not encountered, default values are used.

The following are allowed commands and parameters:

ADC <switch> <resolution>

This command controls the resolution used for the raw voltage from the ADC's. If switch=1, then the resolution is set to the number of bits specified by <resolution>. If switch=0, then the full resolution is used (20 bits).

SMOOTH <switch> <P1> <P2> <P3> <P4> <P5>

The switch instructs the program to smooth the data. The data will be smoothed <switch> if set to an integer greater than zero. If <switch> > 0, the number selects the smoothing method used. P1, P2, and P3 have different meanings depending on the method of smoothing selected. Table A.1 lists all the choices and their meanings in context.

In all cases except the gaussian weighted average, P3 is an integer which tells the user how to treat the ends of the data array if the weighted sum option is used:

- 1 = REPEAT (repeat the last point)
- 2 = BOUNCE (use the last points in reverse order)
- 3 = WRAP (as if the data was one period of a sinusoidal wave)
- 4 = ZERO (additional points are = 0.0)
- 5 = NOTHING (no smoothing on the ends)
- 6 = FIT (extrapolate the data by linear fit)

In the gaussian smoothing case, the width of the gaussian is a function of the local derivatives, given by:

$$\sigma(x) = (\sigma_{max} - \sigma_{min})e^{-|x|/x_0} \quad (\text{A.1})$$

where σ_{min} , σ_{max} , and x_0 are P1, P2, and P3 specified by the user, and x is the value of the local derivatives. Typical values are $\sigma_{min}=1$, $\sigma_{max}=10$, $x_0=2$. The maximum gradients encountered in the field maps are ~ 7 T/m which is a useful number when deciding how to set x_0 . P4 is the number of times to apply the smoothing algorithm. P5 is a switch for smoothing in the polar angle coordinate; 0=off, 1=on.

Table A.1: Smoothing parameters and their meanings

Switch	Smoothing method	P1	P2	P3
≤ 0	None	--	--	--
1	Savitzky-Golay weighted average	Number of points	polynomial order	end effect
2	Binomial weighted average	Number of points	--	end effect
3	average	Number of points	--	end effect
4	not used	--	--	--
5	Gaussian weighted average	minimum sigma	maximum sigma	decay constant
6	Polynomial fit over entire radial range	polynomial order	--	--

BADPASS <switch> <nbad> <nbs_max> <nsig>

If switch = 1 then bad passes are smoothed by local radial fits. <nbad> controls the azimuthal (ϕ) sample number where the radial passes are checked for bad passes. The program fits the radial data at the <nbad>th polar sample. The program chooses the <nbs_max> worst samples that have a deviation greater than <nsig>*(the standard deviation from the fit) and replaces them with the fitted value.

INPUT <map file name> <integer current>

The map file name is the name of the file which contains the binary raw data from a S800 dipole map. This file is generated by reading the raw integer data from a text file

and writing it back out in “unformatted” mode from a FORTRAN program. This is done to conserve disk space. The integer current is the rough current that the map was taken at. Allowed values are 50,100,150,...,400 for D1 and the same for D2 with 420 added. The valid numbers are given in Tables 3.1 and 3.2 and are always rounded to the nearest 25 Amps. So, 111 Amps is labeled “100”, and 366 Amps is labeled “375”. The label is used to lookup the appropriate calibration values from the calibration files and to construct the output file names.

INTERP <switch> <spacing in mm> <# of points to use> <interp. method>

If switch = 1 then interpolation from polar to cartesian coordinates is performed. The spacing of the xy grid has to be specified in mm. The number of points to use is the number of points to use in one dimension. For example, if NPTS = 4, then 16 surrounding points will be used to determine the value of the field at the specified point. The interpolation method is an integer which selects the type of interpolation to be done. The following is a list of allowed types:

11 one-dimensional cubic spline interpolation (Akima), from IMSL

12 one-dimensional b-spline interpolation (Akima), from IMSL

13 one-dimensional Newton's divided difference method, from CERN library

14 one-dimensional Lagrangian interpolation (3rd order), from Numerical Recipes

15 one-dimensional Singular Value Decomposition fit, from Num. Rec.

21 two-dimensional area weighted average of surrounding 4 points

22 two-dimensional average of surrounding 4 points

23 two-dimensional distance weighted average of surrounding 4 points

FILES <nmr probe data file name> <hall probe data file name>

The two file names where the calibration data is kept.

FFT <switch> <P1> <P2>

If switch = 1 then a FFT is performed on each single pass of the data, with cuts at $N=P1$ and $N=P2$ in the fourier amplitudes. Default is no FFT.

ALIGN <switch>

If switch = 1 then the odd and even passes at the same radial coordinate are aligned with each other by interpolating the even pass some distance and minimizing the sum-squared difference between each pass.

CALIBRATE <switch>

If switch = 1 then the map is calibrated according to the two calibration files specified in the FILES command, using the integer current specified in the INPUT command to determine which data from the calibration files to use.

ROTATE <switch> <X0> <Y0> <angle>

If switch = 1, the the map is rotated about the point (X0,Y0)(in meters) by the angle (in degrees).

TRANSLATE <switch> <dx> <dy>

If switch = 1 then the map is translated by the amount (dx,dy) (in meters).

PASSES <switch>

If switch = 0, then the average of even and odd passes is used.

If switch = 1, then only odd passes are used (default).

If switch = 2, then only even passes are used.

POSCAL <switch>

This option exists for maps of the small, permanent magnets used to calibrate the

absolute position of the mapper with respect to the magnet steel. If the switch=1, then the program reads in the residual field map and subtracts the appropriate portion of the map from the permanent magnet map. This removes the contribution to the field from the residual magnetization and gives a more accurate position determination. Calibration of the map is not performed either. If switch=0, the map is assumed to be an ordinary field map.

A.3 Sample input file

The following is a sample input file:

```
adc      1      18
smooth   1      25.    2.    6.    10.    1.
BADPASS  1  1100    5    2.0
INPUT    [.D1RAW]D1400TCO_UNF.MAP 400
INTERP   1  5.0  50  15
FILES    D1_NMR.DAT [.D1HALL]D1_HALL_PROBE.DAT
FFT      0      3      5
ALIGN    1
CALIBRATE 1
ROTATE   0  3.0412  0.0  -.115
TRANSL   1      -0.0059    0.0
PASSES   2
POSCAL   0
```

Notice that the program is not case sensitive; the keywords can have any combination of capital letters in them. The program only reads the first 3 letters of the keyword ; the rest of the letters are just for the reader's edification. Spacing and format don't matter as long as at least one space or tab exists between all parameters.

Proceeding from the first line down, the ADC resolution was set to 18 bits. The data was smoothed according to the Savitzky-Golay algorithm using 2nd order polynomial weighting. The ends were extrapolated with a linear fit, the smoothing algorithm will be applied 10 times, and polar angle smoothing will be done once. Bad passes were fixed

using the 1100th angular sample to check for deviations. Deviations greater than 2σ will be replaced by the fitted value. The five worst passes were fixed. The data were taken from D1 and the raw map data is contained in a file called [.D1RAW]D1400TCO_UNF.MAP and the current setting for the map was ~ 400 Amps for each of the dipoles. The data was interpolated onto a cartesian grid from the polar grid using a 50x50 grid with spacing of 5 mm. The 15 indicates 1D interpolations using a polynomial fit. The calibration data was stored in the files D1_NMR.DAT [.D1HALL]D1_HALL_PROBE.DAT (NMR and hall probe respectively) and the data will be calibrated. No FFT filtering was performed. The odd and even passes were aligned with each other. The map was not rotated, but translated -5.9 mm in the x direction. The output files contained only even pass data and the map was an ordinary field map, not a position calibration map.

A.4 Output files

There are two sets of output files. One set is called <map file prefix>_rphi_c*.out. The rphi tells the user that the data contained in that file is in polar coordinates. The C* determines which coil the map corresponds to - C1 is the coil #1, etc. The file is in fortran unformatted (binary) format. Each record of the file contains all of the data for PHI=constant, R=(rmin,rmax). Thus, the number of records in the file is equal to the number of phi samples in the map. There is a header on the file which is two integers: NR and NP, the number of samples in the r and phi directions, respectively. NP will be the number of lines in the file following the header line, while the NR will specify how many numbers are in each line (record).

The other set of output files are called <map file prefix>_xy_c*.out. The files con-

tain the map data on a cartesian grid, whose pitch is specified by the user in the command INTERP. The header on this file contains an exact replica of the input file preceeded by the date and time stamp and the input file name. The input file is followed by the 5 character string <EOH>, followed by the following parameters:

XMIN,XMAX,YMIN,YMAX,SPACING

NX,NY

These parameters specify the extent of the cartesian grid that holds the data. The data is on a square whose lower left corner is (XMIN,YMIN) and whose upper right corner is (XMAX,YMAX). There are NX x NY points on the grid, separated by (SPACING). All coordinates are in meters. Here is a sample of the header of an output file, which was used to process a D1 field map taken at B=1.56 Tesla:

```

FILE WAS CREATED ON 13-NOV-1998 02:40:29.84
PARAMETER FILE USED: D1_400.INP
adc      0   20
smooth   0  25.  2.  6.  1.  1.
BADPASS  1 1100  5  2.0
INPUT    [.D1RAW]D1400TCO_UNF.MAP 400
INTERP   1 5.0 50 15
FILES    D1_NMR.DAT [.D1HALL]D1_HALL_PROBE.DAT
FFT      0   3   5
ALIGN    1
CALIBRATE 1
ROTATE   0 3.0412 0.0 -.115
TRANSL   1 -0.0059  0.0
PASSES   2
POSCAL   0
<EOH>

```

The body of the data is zero suppressed to conserve disk space. The first four numbers of the record are integers that contain the extent of the non-zero portion of the maps. (Usually, only the first two integers are non zero.) The rest of the record is written for a

given Y value.

The sample output file header above describes a typical set of map processing parameters used to provide Daniel Bazin with field data with which he created inverse transfer maps for S800 experiments. For D1 maps, the even passes (the ones in which gravity helped the motion) were used. For D2 maps, the odd passes (again, the ones in which gravity helped the motion) were used.

Appendix B

Inverse transfer maps

This appendix lists all of the inverse map coefficients used to reconstruct energy and scattering angle in both experiments. Table B.1 contains all coefficients up through 3rd order for the ^{10}Li experiment (Chapter 4). Table B.2 contains all coefficients through 3rd order for the ^{23}Al and ^{27}P experiment (Chapter 5).

In COSY language, the dispersive angle is called a and the vertical angle is called b , i.e. $a=\theta$ and $b=\phi$. The reconstructed coefficients are a , y , b , and d in the scattering chamber as a function of x , a , y , b in the focal plane. Positions and angles are expressed in meters and radians. The d variable is the reconstructed fractional energy, $d=(E-E_0)/E_0$. All coefficients of the form $(a|*)$ are grouped together, as are the $(y|*)$ coefficients, etc. The coefficients for each reconstructed variable are grouped according to order and sorted from lowest order (at the top) to highest order (at the bottom). For example, the third order a coefficient $(a|xb^2)$ has the value $-1.311 \text{ rad m}^{-1} \text{ rad}^{-2}$ in Table B.1.

Table B.1: Inverse map coefficients for the ^{10}Li experiment.

Coef. #	Value	Order	x	a	y	b
a coefficients						
1	1.859E-02	1	1	0	0	0
2	-1.015E+00	1	0	1	0	0
3	-1.323E-02	2	2	0	0	0
4	1.991E-01	2	1	1	0	0
5	6.234E-02	2	0	2	0	0
6	1.635E-02	2	0	0	2	0
7	-1.283E-01	2	0	0	1	1
8	1.059E-01	2	0	0	0	2
9	3.537E-03	3	3	0	0	0
10	-5.004E-02	3	2	1	0	0
11	1.412E-01	3	1	2	0	0
12	-3.467E+00	3	0	3	0	0
13	4.078E-02	3	1	0	2	0
14	-4.230E+00	3	0	1	2	0
15	3.864E-01	3	1	0	1	1
16	3.508E+00	3	0	1	1	1
17	-1.331E+00	3	1	0	0	2
18	-1.840E+00	3	0	1	0	2
y coefficients						
1	-5.527E-01	1	0	0	1	0
2	9.537E-01	1	0	0	0	1
3	-3.267E-02	2	1	0	1	0
4	3.705E-01	2	0	1	1	0
5	-1.501E-01	2	1	0	0	1
6	-4.029E+00	2	0	1	0	1
7	-3.218E-02	3	2	0	1	0
8	-1.297E-01	3	1	1	1	0
9	7.813E+00	3	0	2	1	0
10	-2.645E-01	3	0	0	3	0
11	2.089E-01	3	2	0	0	1
12	3.403E-01	3	1	1	0	1
13	-4.810E+00	3	0	2	0	1
14	3.178E+01	3	0	0	2	1
15	-2.199E+02	3	0	0	1	2

Table B.1: Inverse map coefficients for the ^{10}Li experiment.

Coef. #	Value	Order	x	a	y	b
16	5.034E+02	3	0	0	0	3
b coefficients						
1	-7.183E-01	1	0	0	1	0
2	-4.317E-01	1	0	0	0	1
3	9.235E-02	2	1	0	1	0
4	2.173E+00	2	0	1	1	0
5	-3.506E-01	2	1	0	0	1
6	-9.858E+00	2	0	1	0	1
7	-9.809E-02	3	2	0	1	0
8	1.533E-01	3	1	1	1	0
9	-5.302E+00	3	0	2	1	0
10	-5.845E+00	3	0	0	3	0
11	5.418E-01	3	2	0	0	1
12	1.939E+00	3	1	1	0	1
13	5.329E+00	3	0	2	0	1
14	7.659E+01	3	0	0	2	1
15	-4.741E+02	3	0	0	1	2
16	1.057E+03	3	0	0	0	3
d coefficients						
1	2.057E-01	1	1	0	0	0
2	1.201E-02	1	0	1	0	0
3	1.632E-02	2	2	0	0	0
4	1.575E-01	2	1	1	0	0
5	5.794E-01	2	0	2	0	0
6	9.261E-02	2	0	0	2	0
7	-4.582E-01	2	0	0	1	1
8	1.143E+00	2	0	0	0	2
9	1.271E-03	3	3	0	0	0
10	-1.783E-02	3	2	1	0	0
11	1.216E-01	3	1	2	0	0
12	-1.922E+00	3	0	3	0	0
13	3.922E-02	3	1	0	2	0
14	-1.859E+00	3	0	1	2	0
15	-4.231E-02	3	1	0	1	1
16	1.468E+00	3	0	1	1	1
17	-5.444E-02	3	1	0	0	2
18	3.971E-02	3	0	1	0	2

Table B.2: Inverse map coefficients for the rp-process nuclei experiment.

Coef. #	Value	Order	x	a	y	b
a coefficients						
1	1.571E-02	1	1	0	0	0
2	-9.232E-01	1	0	1	0	0
3	-1.191E-02	2	2	0	0	0
4	1.854E-01	2	1	1	0	0
5	5.844E-02	2	0	2	0	0
6	1.457E-02	2	0	0	2	0
7	-1.169E-01	2	0	0	1	1
8	1.084E-01	2	0	0	0	2
9	3.257E-03	3	3	0	0	0
10	-4.881E-02	3	2	1	0	0
11	1.833E-01	3	1	2	0	0
12	-4.525E+00	3	0	3	0	0
13	7.037E-02	3	1	0	2	0
14	-6.106E+00	3	0	1	2	0
15	3.017E-01	3	1	0	1	1
16	6.683E+00	3	0	1	1	1
17	-1.219E+00	3	1	0	0	2
18	-3.008E+00	3	0	1	0	2
y coefficients						
1	-2.315E-01	1	0	0	1	0
2	7.835E-01	1	0	0	0	1
3	-9.625E-02	2	1	0	1	0
4	-1.844E-01	2	0	1	1	0
5	-1.720E-02	2	1	0	0	1
6	-8.269E-01	2	0	1	0	1
7	6.873E-03	3	2	0	1	0
8	-1.656E-01	3	1	1	1	0
9	9.953E+00	3	0	2	1	0
10	2.533E+00	3	0	0	3	0
11	1.633E-02	3	2	0	0	1
12	-6.366E-01	3	1	1	0	1
13	-6.798E+00	3	0	2	0	1
14	4.384E+00	3	0	0	2	1
15	-5.764E+01	3	0	0	1	2
16	1.418E+02	3	0	0	0	3
b coefficients						

Table B.2: Inverse map coefficients for the rp-process nuclei experiment.

Coef. #	Value	Order	x	a	y	b
1	-1.266E+00	1	0	0	1	0
2	-3.319E-02	1	0	0	0	1
3	1.319E-01	2	1	0	1	0
4	2.901E+00	2	0	1	1	0
5	-5.266E-01	2	1	0	0	1
6	-1.432E+01	2	0	1	0	1
7	-1.459E-01	3	2	0	1	0
8	2.179E-01	3	1	1	1	0
9	-7.316E+00	3	0	2	1	0
10	-8.941E+00	3	0	0	3	0
11	8.108E-01	3	2	0	0	1
12	2.863E+00	3	1	1	0	1
13	7.910E+00	3	0	2	0	1
14	1.126E+02	3	0	0	2	1
15	-6.941E+02	3	0	0	1	2
16	1.561E+03	3	0	0	0	3
d coefficients						
1	2.054E-01	1	1	0	0	0
2	-3.053E-03	1	0	1	0	0
3	1.622E-02	2	2	0	0	0
4	1.661E-01	2	1	1	0	0
5	5.711E-01	2	0	2	0	0
6	9.321E-02	2	0	0	2	0
7	-4.661E-01	2	0	0	1	1
8	1.156E+00	2	0	0	0	2
9	1.412E-03	3	3	0	0	0
10	-2.253E-02	3	2	1	0	0
11	1.644E-01	3	1	2	0	0
12	-2.642E+00	3	0	3	0	0
13	5.480E-02	3	1	0	2	0
14	-2.949E+00	3	0	1	2	0
15	-5.982E-02	3	1	0	1	1
16	2.996E+00	3	0	1	1	1
17	-6.261E-02	3	1	0	0	2
18	-5.324E-01	3	0	1	0	2

Bibliography

- [Aj88] F. Ajzenberg-Selove, Nucl. Phys. A490, 1 (1988).
- [Al96] J.S. Al-Khalili and J.A. Tostevin, Phys. Rev. Lett. 76, 3903 (1996).
- [Am90] A. I. Amelin *et al.*, Sov. J. Nucl. Phys. 53, 782 (1990).
- [Ar87] E. Arnold *et al.*, Phys. Lett. B197 311 (1987).
- [Au93] G. Audi and A.H. Wapstra, Nucl. Phys. A565, 1 (1993).
- [Au95] G. Audi and A.H. Wapstra, Nucl. Phys. A595, 409 (1995).
- [Ba77] F.C. Barker and G.T. Hickey, J. Phys. G3, L23 (1977).
- [Be75] W. Benenson *et al.*, Phys. Lett. 58B, 46 (1975).
- [Be76] F.D. Becchetti *et al.*, Nucl. Inst. Meth. 138, 93 (1976).
- [Be77] W. Benenson *et al.*, Phys. Rev. C15, 1187 (1977).
- [Be79] W. Benenson and E. Kashy, Rev. Mod. Phys. 51, 527 (1979).
- [Be93] M. Berz *et al.*, Phys. Rev. C 47, 537 (1997).
- [Be95] M. Berz *et al.*, ‘COSY INFINITY User’s Guide and Reference Manual’, version 7, MSUCL-977 (1995).
- [Be98] G.F. Bertsch *et al.*, Phys. Rev. C57, 1366 (1998).
- [Bl56] M.M. Block, Phys. Rev. 101, 796 (1956).
- [Bl92] B. Blank *et al.*, Z. Phys. A343, 375 (1992).
- [Bo93] H. Bohlen *et al.*, Z. Phys. A344, 381 (1993).
- [Bo97] H. Bohlen *et al.*, Nucl. Phys. A616, 254c (1997).
- [Ch92] A.E. Champagne and M. Wiescher, Ann. Rev. Nucl. Part. Phys. 42, 39 (1992).
- [Da85] N.J. Davis *et al.*, Phys. Rev. C32, 713 (1985).
- [De92] R. Degenhart *et al.*, NSCL annual report article, 216 (1992).
- [En79] H.A. Enge, Nucl. Inst. Meth. A162, 161 (1979).
- [Ha95] P. G. Hansen *et al.*, Annu. Rev. Nucl. Part. Sci. 45, 591 (1995).
- [He95] H. Herndl *et al.*, Phys. Rev. C52, 1078 (1995).
- [Ka98] F. Kappeler *et al.*, Annu. Rev. Nucl. Part. Sci. 48, 175 (1998).

- [Ko88] T. Kobayashi *et al.*, Phys. Rev. Lett. 60, 2599 (1988).
- [Ko99] A. Komives *et al.*, NSCL experiment #95037, to be published in 1999.
- [Ko] J.J. Kolata *et al.*, NSCL experiment #97003, results unpublished.
- [Kr93] R.A. Kryger *et al.*, Phys. Rev. C47, R2439 (1993).
- [Ma83] P. Marchand and L. Marmet, Rev. Sci. Inst. 54 (8), 1034 (1983).
- [Mc94] K.W. McVoy and P. Van Isacker, Nucl. Phys. A 576, 157 (1994).
- [No89] J.A. Nolen Jr. *et al.*, Proposal for the construction of the S800 spectrograph, MSUCL-694, 1989.
- [No92] J.A. Nolen Jr., Enc. App. Phys. 3, 273 (1992).
- [Or98] N. A. Orr, conference proceedings from 16th European Conference on Few-Body Problems in Physics, Autrans, France, June 1998.
- [Pr92] W.H. Press *et al.*, Numerical Recipes in Fortran, 2nd ed., Wiley (1992).
- [Ri92] K. Riisager, Rev. Mod. Phys. 66, 1105 (1992).
- [Ro88] C.E. Rolfs and W.S. Rodney, Cauldrons in the Cosmos, University of Chicago Press (1988).
- [Sc97] H. Schatz *et al.*, Phys. Rev. Lett. 79, 3845 (1997)
- [Sh92] B. Sherrill *et al.*, Nucl. Inst. Meth. B70, 289 (1992).
- [St69] R.H. Stokes and P.G. Young, Phys. Rev. 178, 1789 (1969).
- [St98] J. Stetson, private communication.
- [Ta82] I. Tanihata *et al.*, Phys. Rev. Lett. B 289, 261 (1992).
- [Ta85] I. Tanihata *et al.*, Phys. Rev. Lett. 2676 (1985).
- [Th84] G.B. Thomas Jr. and R.L. Finney, Calculus and Analytical Geometry, 6th ed., Wiley, (1984).
- [Th94] I.J. Thompson and M.V. Zhukov, Phys. Rev. C49, 1904 (1994).
- [Th99] M. Thoennessen *et al.*, Phys. Rev. C59, 111 (1999).
- [Wi75] K. H. Wilcox *et al.*, Phys. Lett. B59, 142 (1975).
- [Wi88] M. Wiescher *et al.*, Nucl. Phys. A 484, 90 (1988).
- [Yo94] B.M. Young *et al.*, Phys. Rev. C49, 279 (1994).

- [Yu98] J. Yurkon *et al.*, NSCL Annual Report for the year 1997, FOCAL PLANE DETECTOR FOR THE S800 HIGH RESOLUTION SPECTROMETER, (http://www.nscl.msu.edu/news/annual_report/Yurkon.pdf).
- [Ze93] A. Zeller, private communication
- [Zh97] B. Zhang, Ph. D. dissertation, Characteristics of the Superconducting Magnets for the S800 Spectrometer (1997).
- [Zi95] M. Zinser *et al.*, Phys. Rev. Lett. 75, 1719 (1995).
- [Zi97] M. Zinser *et al.*, Nucl. Phys. A619, 151 (1997).